

# Exploring Point Defects as Qubit Candidates in Cubic Boron Nitride

Joseph Panama Vera



Thesis submitted for the degree of  
Master in Material Science  
60 credits

Department of Physics  
Faculty of Mathematics and Natural Sciences

UNIVERSITY OF OSLO

Spring 2025



# **Exploring Point Defects as Qubit Candidates in Cubic Boron Nitride**

Joseph Panama Vera

© 2025 Joseph Panana Vera

Exploring Point Defects as Qubit Candidates in Cubic Boron Nitride

<http://www.duo.uio.no/>

Printed: Reprosentralen, University of Oslo

# Abstract

Point defects have emerged as a powerful tool for advancing knowledge and technology. Their influence extends to cutting-edge fields such as quantum technologies, enabling significant findings and driving remarkable scientific progress.

This thesis explores point defects in wide band gap semiconductors as qubits platforms for quantum technologies applications. A study of the NV center in diamond is included as a guide for the exploration of candidate defects in cubic boron nitride (c-BN). Four defects are investigated in c-BN:  $N_B$ ,  $V_B - V_N$ ,  $V_B - C_B$  and  $V_B - Si_B$ . Ab initio simulations were performed to investigate the properties of defects. Additionally, the decay of coherence of the spin defect over time was analyzed using the cluster-correlation expansion (CCE) method.

Our results for the study of the NV center in diamond are consistent with available literature. It exhibits a triplet ground-state spin and a zero-phonon line (ZPL) of 2.227 eV ( $\lambda = 557$  nm), confirming its classification as a color center. In addition, this defect exhibits a coherence time of 0.916 ms. On the other hand, in c-BN,  $N_B$  with a charge state +1 exhibits a doublet ground-state spin. Nevertheless, it is also reported as a color center due to its ZPL of 1.64 eV ( $\lambda = 757$  nm). Finally, the three complex defects with neutral charges states exhibits the desired triplet ground-state spin.  $V_B - V_N$  reports a ZPL of 0.826 eV ( $\lambda = 1503$  nm),  $V_B - C_B$  reports a ZPL of 0.933 eV ( $\lambda = 1331$  nm), and  $V_B - Si_B$  report a ZPL of 1.256 eV ( $\lambda = 988$  nm). All these complex defects emit at telecom wavelenghts, making them promising candidates for quantum communication applications.

# Acknowledgements

First of all, I would like to thank the University of Oslo for trusting me and giving me the opportunity to pursue this research project. Furthermore, I am deeply grateful to the Norwegian people for their warm hospitality over these few years.

I would also like to express my gratitude: to my main supervisor, Marianne Etzelmüller Bathen, for her constant guidance and support. Thank you for sharing your knowledge and brilliant ideas for the development of this project, besides showing me how wonderful the world of quantum technologies is. To Morten Hjorth-Jensen, for his wonderful classes, your enthusiasm undoubtedly served as both motivation and inspiration for much of my work. Thank you for such great ideas and conversations in spanish. To David Rivas Gongora, for his guidance and the great discussions about physics. Also, a special thank you for your support since my arrival in Norway. To Christopher Linderälv, for his excellent constructive criticism.

I would also like to thank David and Pablo Rivera Riofano for the trust they have placed in me from the beginning through the NORPART project.

To my parents, siblings, aunt and uncle, thank you for your constant support and confidence throughout this process.

A mis padres, hermanos, tía y tío, gracias por su constante apoyo y confianza a lo largo de este proceso.

# Contents

<b>Abstract</b>	<b>i</b>
<b>Acknowledgements</b>	<b>ii</b>
<b>1 Introduction</b>	<b>1</b>
<b>2 Condensed Matter Physics Background</b>	<b>3</b>
2.1 Crystal structure . . . . .	3
2.1.1 Bravais lattice . . . . .	4
2.1.2 Unit cell . . . . .	6
2.1.3 Reciprocal space . . . . .	7
2.2 Electrons in a periodic potential . . . . .	8
2.2.1 Single-electron Schrödinger equation . . . . .	9
2.2.2 Bloch's theorem . . . . .	10
2.3 Phonons . . . . .	11
2.3.1 Brief formalism . . . . .	11
2.3.2 Optical and acoustic phonons . . . . .	12
2.4 Physics of semiconductors . . . . .	14
2.4.1 Types of materials . . . . .	14
2.4.2 Band structure . . . . .	15
2.4.3 Types of semiconductors: Doping . . . . .	16
2.5 Defects in crystalline materials . . . . .	19
2.5.1 Point defects . . . . .	19
2.5.2 Thermodynamic approach . . . . .	20
2.5.3 Point defects for quantum technologies . . . . .	22
2.6 Cubic boron nitride . . . . .	23
2.6.1 Crystal structure . . . . .	24
2.6.2 Point defects in c-BN . . . . .	25
<b>3 Fundamentals of Density Functional Theory</b>	<b>27</b>
3.1 Quantum mechanics in many-body systems . . . . .	27
3.1.1 The Schrödinger equation . . . . .	27
3.1.2 Born-Oppenheimer approximation . . . . .	28
3.1.3 Hartree method . . . . .	29
3.1.4 Hartree-Fock method . . . . .	30
3.2 Foundations of the Density Functional Theory . . . . .	30
3.2.1 The Hohenberg-Kohn theorems . . . . .	30

3.2.2	The Kohn-Sham equations . . . . .	33
<b>4</b>	<b>Methodology</b>	<b>36</b>
4.1	Self-consistent field method . . . . .	36
4.2	Exchange-correlation functionals . . . . .	37
4.2.1	Local density approximation . . . . .	37
4.2.2	Generalized-gradient approximation . . . . .	37
4.2.3	Hybrid functional . . . . .	38
4.3	Convergence tests . . . . .	38
4.4	Chemical potentials . . . . .	40
4.5	Finite-size corrections . . . . .	41
4.6	Formation energy . . . . .	42
4.6.1	Master equation . . . . .	42
4.6.2	Diagram . . . . .	42
4.7	Optical transitions . . . . .	43
4.8	Spin coherence . . . . .	45
4.9	Selection of point defects in a host material . . . . .	47
<b>5</b>	<b>Computational Aspects</b>	<b>49</b>
5.1	Convergence tests: Primitive cell . . . . .	49
5.2	Convergence test: Stable Phases . . . . .	51
5.3	Convergence test: Supercell . . . . .	54
<b>6</b>	<b>Results</b>	<b>56</b>
6.1	Studies of NV center in diamond . . . . .	56
6.1.1	Bulk properties of diamond . . . . .	56
6.1.2	Formation energy diagram for the NV center . . . . .	58
6.1.3	Kohn-Sham level diagrams . . . . .	60
6.1.4	Zero Phonon Line . . . . .	62
6.2	Studies of c-BN . . . . .	64
6.2.1	Bulk properties of c-BN . . . . .	64
6.2.2	Bulk properties of the elemental components . . . . .	68
6.3	Point Defects in c-BN . . . . .	70
6.3.1	Initial defect selection . . . . .	70
6.3.2	Formation energy diagram . . . . .	71
6.3.3	Kohn-Sham level diagrams . . . . .	74
6.3.4	Zero Phonon Line . . . . .	81
6.4	Spin Coherence . . . . .	84
<b>7</b>	<b>Concluding remarks</b>	<b>87</b>
<b>Bibliography</b>		<b>88</b>
<b>Appendix</b>		<b>93</b>
<b>A Convergence Tests</b>		<b>93</b>
<b>B Local Density of States</b>		<b>98</b>

<b>C Analyzing the Fraction of Exact Hartree-Fock Exchange</b>	<b>99</b>
<b>D NV center in Diamond</b>	<b>101</b>
<b>E Point defects in c-BN</b>	<b>103</b>
<b>List of Figures</b>	<b>107</b>
<b>List of Tables</b>	<b>112</b>

# Chapter 1

## Introduction

A new technological era has begun, this time led by the principles of quantum mechanics. Something that, in past decades, was merely a fantasy—an idea straight out of science fiction. Although quantum mechanics is already a part of our current devices in certain ways, today it is becoming more established by including the use of principles such as quantum entanglement, superposition, and quantum tunneling. This cutting-edge new field is known as quantum technologies. Several potential applications have been envisioned for its use, including quantum computing, quantum communication, quantum sensing, quantum metrology, and so on [1]. One of the main areas of interest in this vast new field is the use of quantum bits (qubits) for quantum computers. The qubits are the basic unit of quantum information. Today, there are several platforms available to obtain these desired qubits. Superconducting materials are widely used to host qubits through the Josephson junctions [1]. However, this latter faces challenges related to the scalability, short coherence times and operation at extremely low temperatures. There are also others potentials platforms for obtaining qubits such as trapped ions, quantum dots, topological qubits and defect-based qubits [2], [3]. The defect-based qubits have attracted particular attention of researchers due to their potential for operation at room temperature and their ability to couple with current technology. Solid-state platforms such as semiconductors (including the wide band gap semiconductors) act as housing for the qubits [4]–[6]. Here, the qubits are obtained by introducing flaws in the crystal structure of the solid. These flaws are known as Point defects.

There are currently several potential host materials for quantum technologies through point defects [1], [4]. Among them is the well-known nitrogen-vacancy (NV) center in diamond. While it is a promising candidate, it faces manufacturing challenges due to the material's hardness. Even so, many researchers have conducted extensive and rigorous investigations into this point defect.

In the theoretical field, ab initio simulations have emerged as a powerful tool for predicting many of the properties of point defects. This allows for the understanding of useful properties such as band structures, formation energy diagrams, spin states, and so on [7]–[9]. The scope of this useful tool includes studies of point defects in host materials such as diamond, silicon carbide, gallium nitride, aluminum nitride, and many others [10].

This master's thesis aims to study two wide band gap host semiconductors: diamond and cubic boron nitride (c-BN). For diamond, the NV center will be studied, while for c-BN, four different point defects will be investigated. Here, studies on the NV center are taken as a benchmark for a proper exploration of point defects in c-BN. Thus, c-BN is the main target material in this thesis. Both materials have a zincblende structure. Diamond is composed solely of carbon atoms, while c-BN consists of boron and nitrogen atoms.

In diamond, the NV center consists of a nitrogen atom substituting a carbon atom, along with a nearby vacancy. On the other hand, in c-BN, the first point defect is an antisite ( $N_B$ ). Then, there are a di-vacancy ( $V_B - V_N$ ), a vacancy-carbon substitution ( $V_B - C_B$ ), and finally, a vacancy-silicon substitution ( $V_B - Si_B$ ).

Point defects, both in diamond and c-BN, will be studied using ab initio simulations. For these simulations, the Vienna Ab initio Simulation Package (VASP) will be used [11]–[14], along with the effective pseudopotentials and the Projector augmented wave (PAW) method [15], [16]. Furthermore, the Perdew, Burke and Ernzerhof (PBE) and Heyd, Scuseria and Ernzerhof (HSE06) functionals will be employed [17], [18].

Initial calculations will be performed to study the bulk properties of the materials. Subsequently, point defect studies will address topics such as defect formation energies and diagrams, Kohn-Sham level diagrams and zero-phonon lines.

The final stage of this thesis will focus on the study of spin coherence. For this purpose, the cluster-correlation expansion (CCE) method will be used to analyze the decay of coherence over time. The PyCCE package provides an implementation of this method [19].

# Chapter 2

## Condensed Matter Physics Background

In this chapter, essential concepts necessary to understand the phenomena studied in this thesis will be introduced. The study of matter requires knowledge of its constituent elements, their arrangement and how they interact with each other. Therefore, concepts such as crystal structure, Bravais lattice, unit cell, reciprocal space, electrons in a periodic potential, and phonons will be discussed. Additionally, it is crucial to understand the properties exhibited by materials, such as semiconductors and insulators, in both their natural and doped states. Here, doping plays a special role in enabling the use of insulators as wide band gap semiconductor materials, which is important in this thesis. Hence, topics such as band structure, doping, and defects will also be covered. Finally, a description of the target material of this thesis, cubic boron nitride, will be included, along with an overview of the promising defects that will be investigated in detail.

### 2.1 Crystal structure

In solid state physics, materials can be classified according to their arrangement pattern as crystalline, polycrystalline, and amorphous. Crystalline materials have an atomic structure that follows a repeating pattern. This repetitive pattern is called a unit cell, which can fill the volume of the material through the periodicity. Based on this, we can conclude that crystalline materials exhibit short-range order in their structural arrangement. In contrast, polycrystalline and amorphous materials lack periodicity. Polycrystalline materials consist of numerous crystallites, each exhibiting short-range order; however, there is no consistent relationship among the various crystallites that make up the material. In the case of amorphous materials, the atomic structure is characterized by a complete lack of order, making it impossible to establish a repeating pattern. Even so, all cases can be described mathematically. In this thesis, we will focus on crystalline materials, as our target material (c-BN) is crystalline.

### 2.1.1 Bravais lattice

A Bravais lattice is a geometric representation of a periodic structure, which can be defined as follows:

#### Bravais lattice

It is defined as an infinite periodic array of discrete points, where all the points are equivalent, generated through translational symmetry operations. Mathematically, in three dimensions (3D), this can be represented as:

$$\mathbf{R} = n_1 \mathbf{a}_1 + n_2 \mathbf{a}_2 + n_3 \mathbf{a}_3. \quad (2.1)$$

Here,  $\mathbf{R}$  is the translation vector,  $n_i$  are integers values and  $\mathbf{a}_i$  are the primitive vectors.

Eq. 2.1 indicates that if we could position ourselves at a lattice point, we would observe the same surroundings as if we were located at any other lattice point (translational invariance).

In 3D, the Bravais lattices can be classified through the point groups. These point groups classify the symmetries of a crystal and are divided into several categories based on their symmetry elements, such as rotation axes, mirror planes, and inversion centers [20]. Following this selective process, only 14 Bravais lattices are distributed in 7 crystalline systems [21]. Table 2.1 shows the information on Bravais lattice classifications in detail. The parameters  $a$ ,  $b$  and  $c$  are the euclidean norm of the primitive vectors  $\mathbf{a}_1$ ,  $\mathbf{a}_2$  and  $\mathbf{a}_3$ ; whereas  $\alpha$ ,  $\beta$  and  $\gamma$  are the angles formed by the primitive vectors.

However, to complete the construction of the crystal, we need one more concept: the basis. The basis or motif is the ingredient that replaces the representative points of the Bravais lattice, which can be composed of one atom or a set of atoms. Note that the Bravais lattice is an abstraction, whereas the crystal has a physical meaning.

#### Crystal structure

$$\text{Basis} + \text{Bravais lattice} = \text{Crystal}$$

Fig. 2.1 shows a simple example of the above relation. Here, we have only considered one atom as the basis, while the Bravais lattice is represented as a 2D hexagonal lattice.

Table 2.1: Classification of Bravais lattices in 3D.

System	Types	Lattice parameters
Cubic	Simple Cubic (SC)	$a = b = c$ $\alpha = \beta = \gamma = 90^\circ$
	Body-Centered Cubic (BCC)	$a = b = c$ $\alpha = \beta = \gamma = 90^\circ$
	Face-Centered Cubic (FCC)	$a = b = c$ $\alpha = \beta = \gamma = 90^\circ$
Tetragonal	Simple Tetragonal (ST)	$a = b \neq c$ $\alpha = \beta = \gamma = 90^\circ$
	Body-Centered Tetragonal (BCT)	$a = b \neq c$ $\alpha = \beta = \gamma = 90^\circ$
Orthorhombic	Simple Orthorhombic (SO)	$a \neq b \neq c$ $\alpha = \beta = \gamma = 90^\circ$
	Base-Centered Orthorhombic (BCO)	$a \neq b \neq c$ $\alpha = \beta = \gamma = 90^\circ$
	Body-Centered Orthorhombic (BCO)	$a \neq b \neq c$ $\alpha = \beta = \gamma = 90^\circ$
	Face-Centered Orthorhombic (FCO)	$a \neq b \neq c$ $\alpha = \beta = \gamma = 90^\circ$
Hexagonal	Simple Hexagonal	$a = b \neq c$ $\alpha = \beta = 90^\circ, \gamma = 120^\circ$
Monoclinic	Simple Monoclinic (SM)	$a \neq b \neq c$ $\alpha = \gamma = 90^\circ, \beta \neq 90^\circ$
	Base-Centered Monoclinic (BCM)	$a \neq b \neq c$ $\alpha = \gamma = 90^\circ, \beta \neq 90^\circ$
Triclinic	Simple Triclinic (ST)	$a \neq b \neq c$ $\alpha \neq \gamma \neq \beta \neq 90^\circ$
Rhombohedral	Simple Rhombohedral (SR)	$a = b = c$ $\alpha = \gamma = \beta \neq 90^\circ$

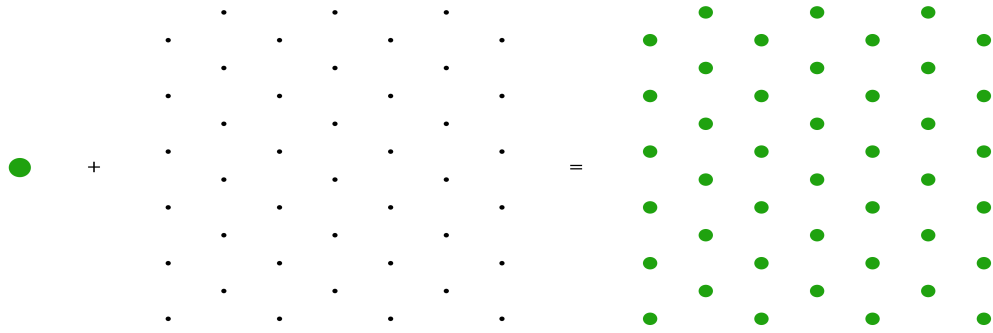


Figure 2.1: Relation between the basis (green ball), the Bravais lattice (set of black points) and crystal (set of green balls).

### 2.1.2 Unit cell

The unit cell is a fundamental term used to describe the smallest repeating unit in a crystal. It can be subdivided into the primitive unit cell and the conventional unit cell, also called the primitive cell and the conventional cell [22].

A primitive cell is a space region containing just one lattice point. When it is translated through all the primitive vectors (translational symmetry), it reconstructs the crystal without overlapping itself or leaving voids. A disadvantage of this type of cell is that it may not reflect the full symmetry of the lattice. This is why, in many cases, it is better to use the conventional cell, since it contains the full symmetry. The cells that contain two or more lattice points are called conventional cells. Just like primitive cells, they also allow us to reconstruct the crystal without overlapping itself or leaving voids. **Fig. 2.2** shows examples of primitive and conventional cells in different dimensions. **Fig. 2.2b** illustrates an example where the conventional cell exhibits the crystal's symmetry more clearly than the primitive cell.

On the other hand, a special type of primitive cell is the Wigner-Seitz cell, since it has the full symmetry of the lattice [23]. The Wigner-Seitz or Voronoi cell describes a uniquely defined region of space around a lattice point. **Fig. 2.2a** shows its construction in two dimensions (2D), which can be done by choosing any lattice point as the origin point and drawing lines to connect it with all the nearest neighbor lattices. The next step is to draw perpendicular lines (planes in 3D) that pass through the midpoints of the previous lines. The volume enclosed by these lines (or planes in 3D) defines the Wigner-Seitz cell.

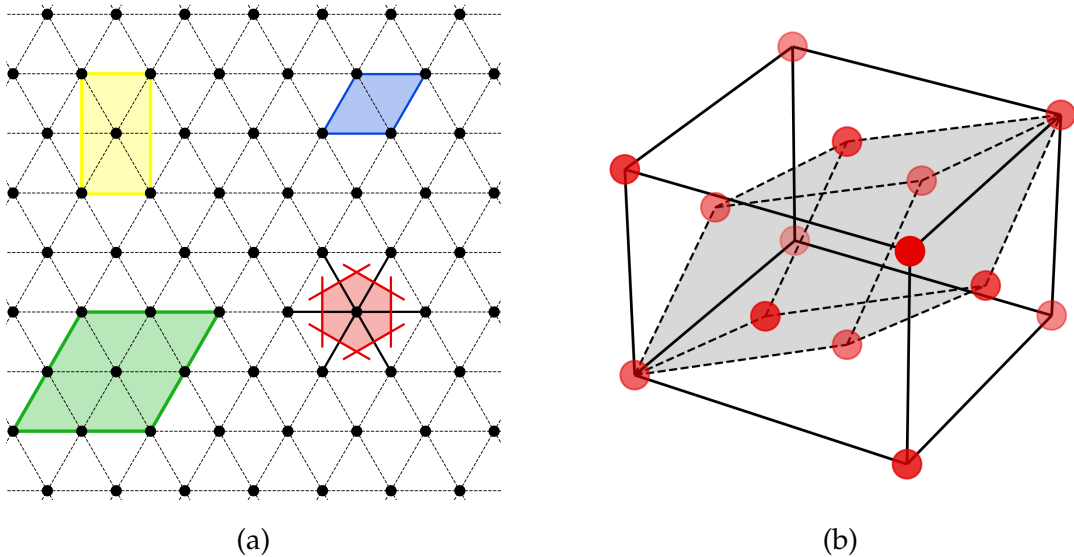


Figure 2.2: (a) 2D representation of primitive and conventional cells in a hexagonal lattice. The cells with blue and red edges are primitive cells, with only the latter being a Wigner-Seitz cell. The cells with green and yellow edges are conventional cells. (b) Primitive and conventional cells of an FCC lattice. The primitive cell is represented with dashed lines and shaded in gray. The conventional cell has a cubic shape and is outlined with solid lines.

### 2.1.3 Reciprocal space

In addition to the real space, the reciprocal space plays an important role since it allows us to obtain information such as diffraction patterns and electronic band structures. In reciprocal space, it is also possible to obtain a lattice containing the periodicity of the crystal [20]. This is known as the reciprocal lattice, and can be defined as follows:

#### Reciprocal lattice

It is the Fourier transform of the real lattice, where each point represents a wave vector  $\mathbf{k}$  that corresponds to the periodicity of the real lattice.

Mathematically, it can be defined, taking into account Eq. 2.1, as a set of vectors  $\mathbf{G}$  that satisfy:

$$e^{i\mathbf{G} \cdot \mathbf{R}} = 1, \quad (2.2)$$

or equivalently

$$\mathbf{G} \cdot \mathbf{R} = 2\pi l, \quad (2.3)$$

where  $l$  is an integer. The vector  $\mathbf{G}$  is known as the reciprocal lattice vector and can be represented as the sum of three new primitive vectors:

$$\mathbf{G} = m_1 \mathbf{b}_1 + m_2 \mathbf{b}_2 + m_3 \mathbf{b}_3, \quad (2.4)$$

where  $m_i$  are integers values, and the vectors  $\mathbf{b}_i$  can be constructed using the primitive vectors of the real lattice as:

$$\mathbf{b}_1 = 2\pi \frac{\mathbf{a}_2 \times \mathbf{a}_3}{\mathbf{a}_1 \cdot (\mathbf{a}_2 \times \mathbf{a}_3)}, \quad (2.5)$$

$$\mathbf{b}_2 = 2\pi \frac{\mathbf{a}_3 \times \mathbf{a}_1}{\mathbf{a}_1 \cdot (\mathbf{a}_2 \times \mathbf{a}_3)}, \quad (2.6)$$

$$\mathbf{b}_3 = 2\pi \frac{\mathbf{a}_1 \times \mathbf{a}_2}{\mathbf{a}_1 \cdot (\mathbf{a}_2 \times \mathbf{a}_3)}. \quad (2.7)$$

The real ( $\mathbf{a}_i$ ) and reciprocal ( $\mathbf{b}_i$ ) primitive vectors satisfy:

$$\mathbf{a}_i \cdot \mathbf{b}_j = 2\pi \delta_{ij}, \quad (2.8)$$

where  $\delta_{ij}$  is a Kronecker delta. If  $i = j$ , then  $\delta_{ij} = 1$  and if  $i \neq j$ , then  $\delta_{ij} = 0$ . It is important to note that the reciprocal lattice, which is constructed using the primitive vectors of the real lattice, is also a Bravais lattice. It is not unreasonable to ask what would occur if we were to create a new lattice from the primitive vectors of the reciprocal lattice, essentially, if we were to construct the reciprocal of the reciprocal lattice. This process would lead us back to the original real lattice, a relationship that can be demonstrated mathematically by formulating new primitive vectors  $\mathbf{c}_1, \mathbf{c}_2$  and  $\mathbf{c}_3$ .

Similar to the real lattice, a cell analogous to the Wigner-Seitz cell can also be constructed within the reciprocal lattice. This cell is known as the first Brillouin zone (1BZ) [24]. The construction procedure follows the same steps as described

above for Wigner-Seitz cell. The representation of the 1BZ in 2D and 3D is shown in Fig. 2.3. Fig. 2.3a shows the 1BZ, as well as higher-order zones in 2D, whereas Fig. 2.3b depicts the 1BZ for an FCC lattice in 3D.

The 1BZ plays a crucial role in our understanding and exploitation of the electronic and vibrational properties of a crystal. It allows us to explore electron behavior and phonon dispersion, as it contains all the unique and necessary wave vectors to describe how waves interact with a periodic potential created by the crystal lattice [25]. Higher-order Brillouin zones are not relevant for studying those properties, since all the essential information is contained within the 1BZ. For instance, if we take a wave vector outside the 1BZ, it can be mapped back into the 1BZ using a reciprocal lattice vector  $\mathbf{G}$ . This process shows that information is redundant due to the periodicity of the reciprocal lattice:

$$\mathbf{k}' = \mathbf{k} + \mathbf{G}. \quad (2.9)$$

Furthermore, we realize that the symmetry of the Brillouin zone is determined by the symmetry of the crystal lattice, as its primitive vectors are constructed based on the primitive vectors of the real lattice, as shown in Eqs. 2.5, 2.6 and 2.7.

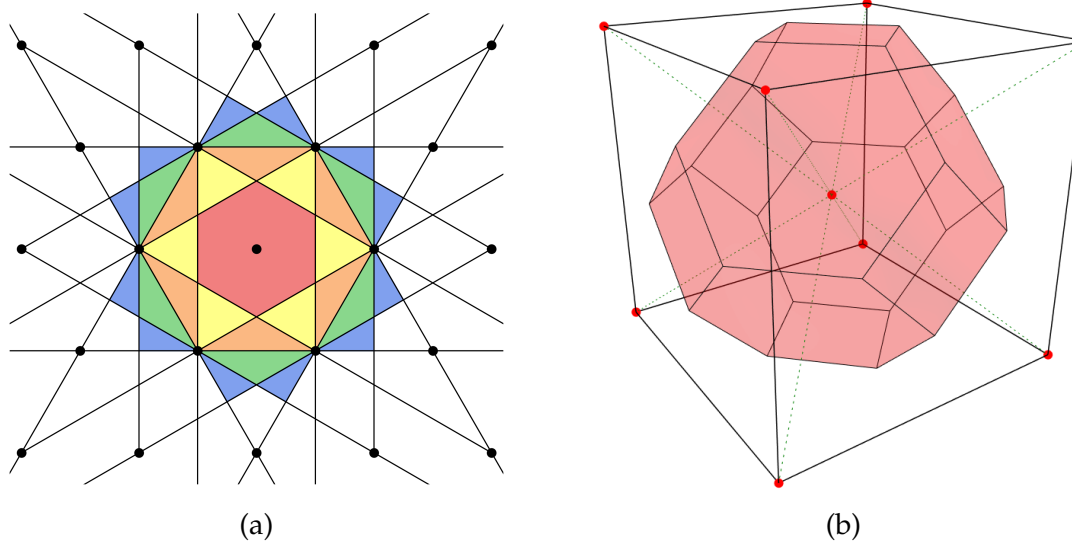


Figure 2.3: (a) Brillouin zones in a hexagonal lattice in 2D: the first zone is shaded in red, the second in yellow, the third in orange, the fourth in green, and finally, the fifth in blue. (b) 1BZ of an FCC lattice in 3D is a truncated octahedron, shaded in red.

## 2.2 Electrons in a periodic potential

As explained above, each point in the Bravais lattice is substituted for a basis to build the crystal. The atoms that constitute this basis can be subdivided into ions and their corresponding valence electrons. In this context, the ions are considered fixed in their positions, obeying the repeating structure of the lattice, while the valence electrons are free to move throughout the crystal lattice. It is important

to note that the ions consist of a nucleus and core electrons. These core electrons are contained in the innermost shells, which are closest to the nucleus. On the other hand, the valence electrons are located in the outermost shell of an atom, which is an typically incomplete shell. Consequently, the arrangement of ions within the lattice generates a periodic potential that interacts with the electrons .

### 2.2.1 Single-electron Schrödinger equation

Facing the challenge of understanding the electron behavior in a periodic potential means diving into a many-electron problem. Fortunately, we can tackle the problem by working only with one electron, that is, by proposing a single-electron Schrodinger equation [26]. This equation is given as:

$$\left[ -\frac{\hbar^2}{2m_e} \nabla^2 + V(\mathbf{r}) \right] \Psi(\mathbf{r}) = E\Psi(\mathbf{r}), \quad (2.10)$$

where  $\hbar$  is the reduced Planck constant,  $m_e$  the electron mass,  $\Psi(\mathbf{r})$  the wave function,  $E$  the energy eigenvalue, and  $V(\mathbf{r})$  is a potential that has the periodicity of the lattice, i.e.,

$$V(\mathbf{r} + \mathbf{R}) = V(\mathbf{r}), \quad (2.11)$$

where  $\mathbf{R}$  is any lattice vector, as defined in Eq. 2.1. Given that the potential is periodic, it can be expressed as a Fourier series:

$$V(\mathbf{r}) = \sum_{\mathbf{G}} V_{\mathbf{G}} e^{i\mathbf{G} \cdot \mathbf{r}}, \quad (2.12)$$

where  $V_{\mathbf{G}}$  are the Fourier coefficients. Furthermore, Eq. 2.12 satisfies Eq. 2.2. Fig. 2.4 shows an example where an arrangement of ions in a one-dimensional Bravais lattice creates a periodic potential.

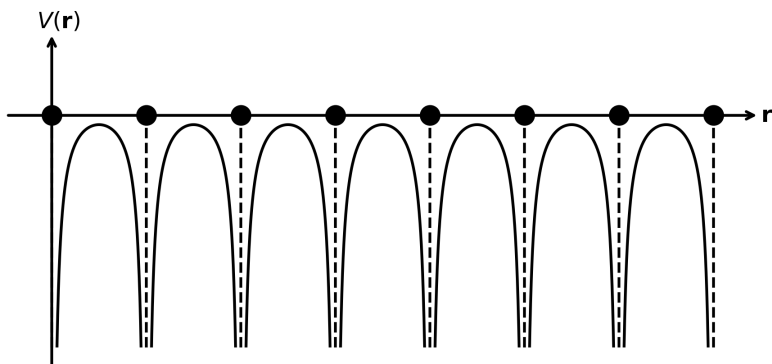


Figure 2.4: Periodic potential in a one-dimensional lattice. The black balls depict the ions.

On the other hand, the general plane wave expansion for the wave function  $\Psi(\mathbf{r})$  can be expressed as:

$$\Psi(\mathbf{r}) = \sum_{\mathbf{k}} C_{\mathbf{k}} e^{i\mathbf{k} \cdot \mathbf{r}}, \quad (2.13)$$

where  $\mathbf{k}$  is the wave vector. If we now substitute the Eqs. 2.12 and 2.13 into the Schrödinger equation (Eq. 2.10):

$$\sum_{\mathbf{k}} \frac{\hbar^2 k^2}{2m_e} C_{\mathbf{k}} e^{i\mathbf{k}\cdot\mathbf{r}} + \sum_{\mathbf{G}, \mathbf{k}} V_{\mathbf{G}} C_{\mathbf{k}} e^{i(\mathbf{G}+\mathbf{k})\cdot\mathbf{r}} = E \sum_{\mathbf{k}} C_{\mathbf{k}} e^{i\mathbf{k}\cdot\mathbf{r}}. \quad (2.14)$$

Note that in the second term on the left-hand side, the sum is taken over all possible values of  $\mathbf{G}$  and  $\mathbf{k}$ , so that term can be rewritten as:

$$\sum_{\mathbf{G}, \mathbf{k}} V_{\mathbf{G}} C_{\mathbf{k}-\mathbf{G}} e^{i\mathbf{k}\cdot\mathbf{r}}. \quad (2.15)$$

Then Eq. 2.14 becomes to:

$$\sum_{\mathbf{k}} e^{i\mathbf{k}\cdot\mathbf{r}} \left\{ \left( \frac{\hbar^2 k^2}{2m_e} - E \right) C_{\mathbf{k}} + \sum_{\mathbf{G}} V_{\mathbf{G}} C_{\mathbf{k}-\mathbf{G}} \right\} = 0, \quad (2.16)$$

the above relation is valid for every vector  $\mathbf{r}$ , so the sum in brackets must vanish for every  $\mathbf{k}$

$$\left( \frac{\hbar^2 k^2}{2m_e} - E \right) C_{\mathbf{k}} + \sum_{\mathbf{G}} V_{\mathbf{G}} C_{\mathbf{k}-\mathbf{G}} = 0. \quad (2.17)$$

The last equation represents a set of equations, which show us the relation between coefficients  $C_{\mathbf{k}}$  and  $C_{\mathbf{k}-\mathbf{G}}$ . Note that there is a difference in the vector  $\mathbf{G}$  between the  $\mathbf{k}$ -values, which means that  $C_{\mathbf{k}}$  is coupled to  $C_{\mathbf{k}-\mathbf{G}}$ ,  $C_{\mathbf{k}-\mathbf{G}'}$ ,  $C_{\mathbf{k}-\mathbf{G}''}$ , and so on. Additionally, it is worth mentioning that Eq. 2.17 is nothing more than a representation of the Schrödinger equation in reciprocal space [27].

## 2.2.2 Bloch's theorem

The new representation shown in Eq. 2.17 allows us to face our problem through a system of  $N$  equations (set of equations), where  $N$  is the number of unit cells. The solution of each equation can be represented as a superposition of plane waves, where its  $\mathbf{k}$ -values differ only by the vector  $\mathbf{G}$ . Given this, we can write the wave function as:

$$\Psi_{\mathbf{k}}(\mathbf{r}) = \sum_{\mathbf{G}} C_{\mathbf{k}-\mathbf{G}} e^{i(\mathbf{k}-\mathbf{G})\cdot\mathbf{r}}, \quad (2.18)$$

and this, in turn, can be rearranged as:

$$\Psi_{\mathbf{k}}(\mathbf{r}) = \left[ \sum_{\mathbf{G}} C_{\mathbf{k}-\mathbf{G}} e^{-i\mathbf{G}\cdot\mathbf{r}} \right] e^{i\mathbf{k}\cdot\mathbf{r}}. \quad (2.19)$$

Therefore, the above equation allows us to define a fundamental theorem [21]. This is expressed as:

## Bloch's Theorem

Electrons subjected to a periodic potential have eigenstates given by:

$$\Psi_{n\mathbf{k}}(\mathbf{r}) = u_{n\mathbf{k}}(\mathbf{r})e^{i\mathbf{k}\cdot\mathbf{r}}, \quad (2.20)$$

the product shows a function  $u_{n\mathbf{k}}(\mathbf{r})$  containing the lattice's periodicity multiplied by a plane wave  $\mathbf{k}$  within the 1BZ. Additionally,  $n$  is known as the band index and is an integer.

It should be noted that any wave function  $\Psi_{\mathbf{k}}(\mathbf{r})$  satisfying Eq. 2.20 is known as a **Bloch function**. Evidently,

$$u_{n\mathbf{k}}(\mathbf{r} + \mathbf{R}) = u_{n\mathbf{k}}(\mathbf{r}), \quad (2.21)$$

and

$$\Psi_{n\mathbf{k}}(\mathbf{r} + \mathbf{R}) = \Psi_{n\mathbf{k}}(\mathbf{r})e^{i\mathbf{k}\cdot\mathbf{R}}, \quad (2.22)$$

for all  $\mathbf{R}$  in the Bravais lattice. Since there are multiple solutions at each  $\mathbf{k}$  corresponding to different energy levels, Bloch functions and the functions  $u_{n\mathbf{k}}(\mathbf{r})$  can be indexed by  $n$  as shown in Eqs. 2.20, 2.21 and 2.22. This simple concept plays an important role in understanding the bands through the dispersion relation  $E_n(\mathbf{k})$ .

## 2.3 Phonons

In a real physical system, ions are not fixed in a certain position but vibrate around their equilibrium positions even at low temperatures, thus generating a collective excitation. The quantification of the collective lattice vibrations are known as phonons.

### 2.3.1 Brief formalism

The displacements generated through the vibrations of the ions can be described under a purely classical treatment governed by Newton's second law:

$$M_\alpha \frac{d^2 u_\alpha}{dt^2} = - \sum_\beta \Phi_{\alpha\beta}(\mathbf{r} - \mathbf{r}') u_\beta(\mathbf{r}'), \quad (2.23)$$

where  $M_\alpha$  is the mass of the ion  $\alpha$ ,  $u_\alpha$  is the displacement of ion  $\alpha$ ,  $u_\beta$  is the displacement of ion  $\beta$  and  $\Phi_{\alpha\beta}(\mathbf{r} - \mathbf{r}')$  is the force constant matrix between ions  $\alpha$  and  $\beta$ , which describes how the movement of ion  $\alpha$  affects ion  $\beta$ . These displacements can, in turn, be used to describe them as a collection of simple harmonic oscillators via the harmonic approximation. This approximation allows us to assume, due to the small displacements, that the force between ions is quadratic. Here, the potential energy is:

$$V = \frac{1}{2} \sum_{\alpha, \beta} \sum_{\mathbf{r}, \mathbf{r}'} u_\alpha(\mathbf{r}) \Phi_{\alpha\beta}(\mathbf{r} - \mathbf{r}') u_\beta(\mathbf{r}'). \quad (2.24)$$

A key point for the description of this behavior is to take advantage of the periodicity of the lattice to study the oscillations in reciprocal space. This allows us to express the oscillations in terms of normal modes [28]. Similar to the Bloch functions for electrons, the displacements can be expressed as plane waves using the Fourier transform:

$$u_\alpha(\mathbf{r}, t) = \frac{1}{\sqrt{N'}} \sum_{\mathbf{q}} e^{i\mathbf{q}\cdot\mathbf{r}} u_\alpha(\mathbf{q}, t), \quad (2.25)$$

where  $N'$  is the number of unit cells in the crystal,  $\mathbf{q}$  is a wave vector,  $e^{i\mathbf{q}\cdot\mathbf{r}}$  is the plane wave, and  $u_\alpha(\mathbf{q}, t)$  is the amplitude of the normal mode [26]. This leads us to find a matrix known as the dynamic matrix, which is essential for understanding the vibrational properties of the lattice:

$$D_{\alpha\beta}(\mathbf{q}) = \frac{1}{\sqrt{M_\alpha M_\beta}} \sum_{\mathbf{r}} e^{i\mathbf{q}\cdot\mathbf{r}} \Phi_{\alpha\beta}(\mathbf{r}). \quad (2.26)$$

The dimensions of the dynamic matrix  $D_{\alpha\beta}(\mathbf{q})$  depend on the number of atoms ( $N$ ) found in the unit cell. In the 3D case, the matrix will consequently have dimensions of  $3N \times 3N$ .

Using the dynamic matrix to solve the eigenvalue problem, we can obtain the frequency of the phonons (eigenvalues) and the oscillatory behavior of the ions in each normal mode (eigenvector), which defines the phonon dispersion relation. The eigenvalue equation is given by:

$$\sum_{\beta} D_{\alpha\beta}(\mathbf{q}) e_{\beta}(\mathbf{q}) = \omega^2(\mathbf{q}) e_{\alpha}(\mathbf{q}), \quad (2.27)$$

where  $e_{\beta}$  and  $e_{\alpha}$  are the eigenvectors and  $\omega$  is the frequency.

### 2.3.2 Optical and acoustic phonons

Optical phonons are characterized by out of phase motion of ions, whereas acoustic phonons are characterized by in-phase motion of ions [26]. From the phonon dispersion relation they can be observed as branches (Fig. 2.5a). The optical phonons are represented as high-energy branches, whereas the acoustic phonons branches are low-energy branches. At the  $\Gamma$ -point their frequency is zero.

If we take into account the perpendicular or parallel displacements of the phonons with respect to the wave vector  $\mathbf{q}$ , we can classify them as transverse or longitudinal. This gives rise to a subclassification according to the nature of the phonons: transverse optical (TO), longitudinal optical (LO), transverse acoustic (TA), and longitudinal acoustic (LA) [26]. It is important to highlight that the **number of branches** present in the phonon dispersion relation is conditioned by the number of atoms in the unit cell and its degrees of freedom. An example is shown in Fig. 2.5b.

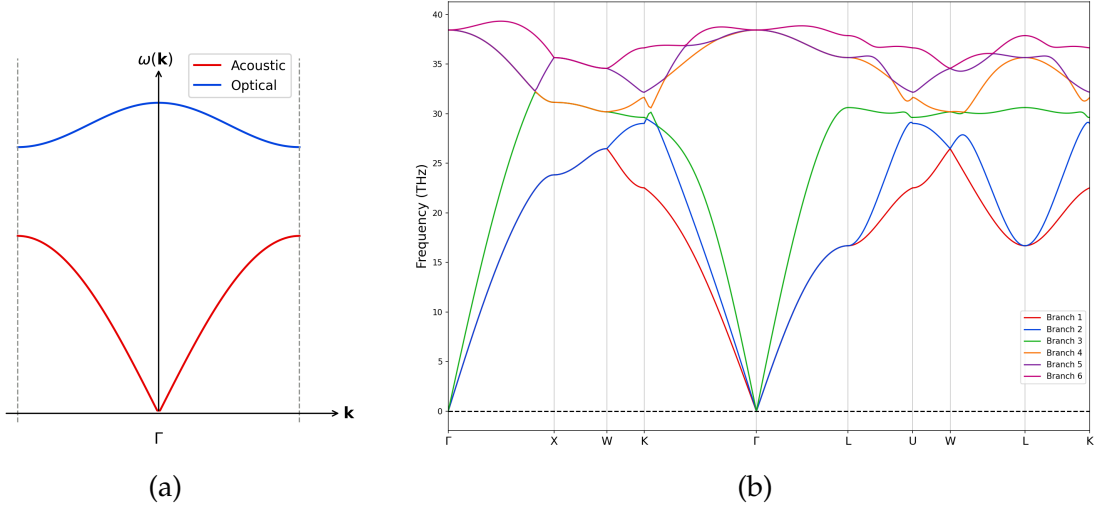


Figure 2.5: (a) Representation of optical and acoustic phonon branches for a 1D diatomic chain. (b) The primitive cell of diamond has 2 atoms, so its phonon dispersion relation is expected to show 6 branches.

On the other hand, to properly represent phonon dispersion relations in polar materials, long-range Coulomb interactions must also be considered. This phenomenon is known as LO-TO splitting and usually occurs at the  $\Gamma$ -point. Here, a correction known as the non-analytical term correction (NAC) must be introduced [29], [30]. This is given by:

$$\omega_{LO}^2(q) = \omega_{TO}^2 + \frac{4\pi e^2}{\Omega_0} \sum_{\alpha\beta} \frac{Z_\alpha^* Z_\beta^*}{\epsilon_\infty q^2}, \quad (2.28)$$

where  $e$  is the electron charge,  $\Omega_0$  is the unit cell volume,  $\epsilon_\infty$  is the electronic dielectric tensor and  $Z_i^*$  are the Born effective charges. Fig. 2.6 shows the phonon dispersion relation for cubic boron nitride, where the LO-TO splitting can be observed. Note that when the correction is not introduced, the branches are degenerate at the  $\Gamma$ -point.

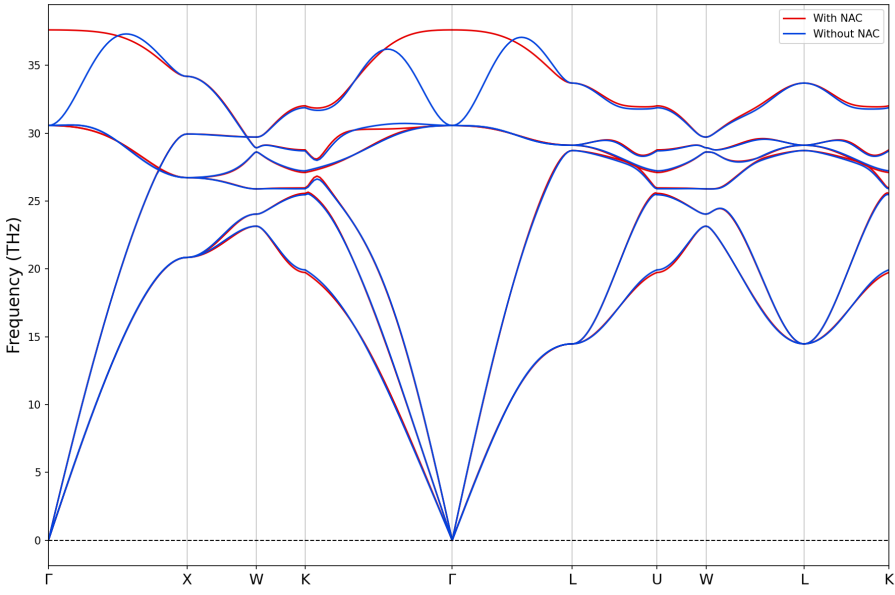


Figure 2.6: The phonon dispersion relation for cubic boron nitride is shown in both cases: without NAC and with NAC. At the  $\Gamma$ -point, the LO-TO splitting can be observed due to the long-range Coulomb interactions in polar materials.

## 2.4 Physics of semiconductors

Semiconductors are materials with properties intermediate between conductors and insulators. These properties give them the capacity to conduct electricity and, more importantly, allow us to manipulate them for technological applications.

### 2.4.1 Types of materials

Within the wide range of crystal materials, they can be classified into three types: conductors, semiconductors and insulators. The main feature that differentiates them is their capacity to conduct electricity. The case of metallic materials is characterized by their high conductivity. This property is due to the overlap between the conduction and valence bands, which allows the electrons to move freely through the material.

On the other hand, semiconductor and insulator materials exhibit a forbidden region between the conduction and valence bands, known as the band gap ( $E_g$ ). This energy gap is a prohibited region for the electrons; that is, they can not occupy energy states within this region. Semiconductors and insulators can be distinguished by the size of their band gap, according to their functionality. Semiconductor materials have a band gap of up to approximately 1.5 eV, which facilitates the movement of electrons from the valence band to the conduction band with minimal excitation energy. This property allows semiconductors to exhibit electrical conductivity. On the other hand, a material can be considered an insulator when its band gap exceeds approximately 3.5 eV. This means that

a significant amount of energy is required to promote an electron from the valence band to the conduction band, making them poor conductors of electricity. However, this latter definition is not absolute, as several insulating materials can exhibit semiconductor characteristics through doping. An example of the above cases is depicted in **Fig. 2.7**.

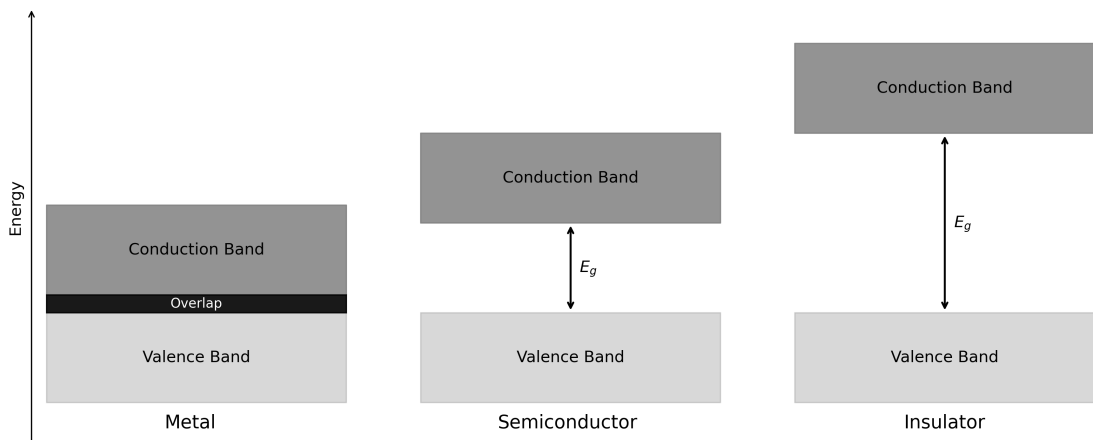


Figure 2.7: Energy level diagrams for different types of materials.

#### 2.4.2 Band structure

In a semiconductor, the valence band is fully occupied by electrons, whereas the conduction band is empty. Take into account that this definition is valid under conditions where the temperature is  $T = 0$  K. When the temperature is increased, the electrons can gain enough energy to be promoted to the conduction band, allowing conduction to take place. This jump is usually performed from the highest energy level of the valence band, known as the valence band maximum (VBM), to the lowest energy level of the conduction band, known as the conduction band minimum (CBM). The energy difference between those two energy values is what is known as the band gap energy ( $E_g$ )

$$E_g = E_{CBM} - E_{VBM}. \quad (2.29)$$

The electron transitions can occur in two ways: directly or indirectly. The main difference lies in whether the momentum ( $\mathbf{k}$ ) is conserved. It is called a direct band gap when the transition occurs from the VBM to the CBM at the same momentum, as shown in **Fig. 2.8a**. This means that the electron only needs to absorb a photon with energy greater than or equal to the band gap energy to reach the CBM. These types of direct transitions are typically observed at the gamma point ( $\Gamma$ ) of band structures. On the other hand, in a material with an indirect band gap, in addition to the photon, a phonon is also involved. This is because the VBM and CBM are at different momenta as shown in **Fig. 2.8b**. The interaction with the phonon (lattice vibration) is required to conserve momentum, since the photon has very little momentum. Both direct and indirect transitions can also occur oppositely to what was described above, that is, through a recombination

process. A radiative recombination occurs when the electron falls back from the CBM to the VBM emitting a photon, whereas a non-radiative recombination does not emit a photon; instead, excess energy is dissipated as heat through the emission of phonons [25].

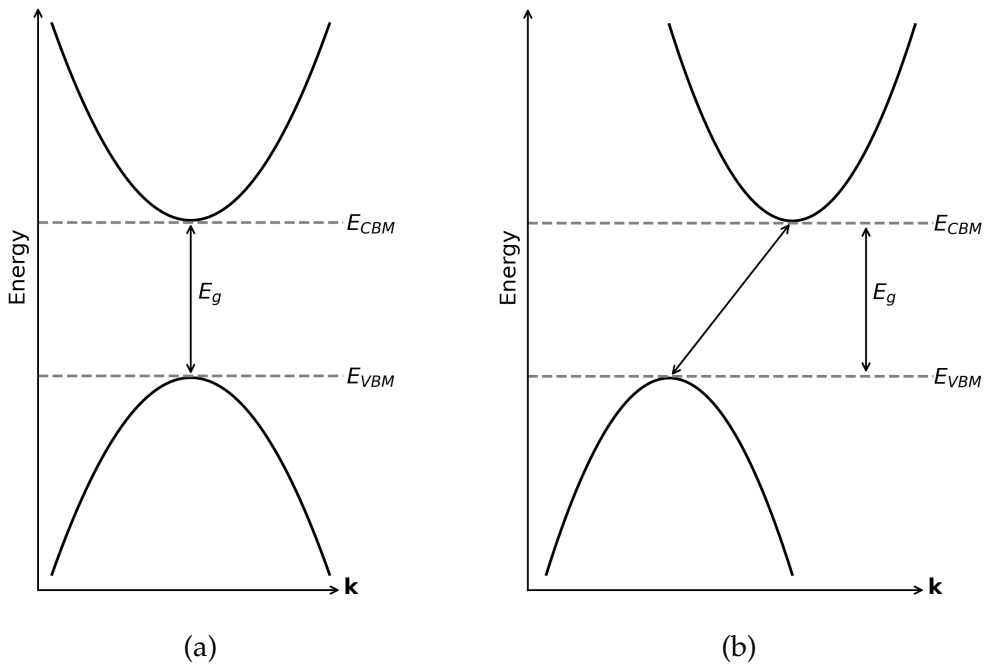


Figure 2.8: Parabolic Band Approximation for semiconductors (a) In a direct band gap semiconductor, the maximum of the valence band and the minimum of the conduction band occur at the same crystal momentum ( $\mathbf{k}$ ). (b) In an indirect band gap semiconductor, the transition occurs at different crystal momenta, with the maximum of the valence band and the minimum of the conduction band located at distinct ( $\mathbf{k}$ ) values

### 2.4.3 Types of semiconductors: Doping

Semiconductor materials in their natural form, called intrinsic, do not offer such interesting properties for electronic applications. However, highly useful properties can be obtained by intentionally introducing impurities. This method of introducing impurities into the material is known as doping, which in semiconductors produces the so-called extrinsic or doped semiconductors. There are two types of extrinsic semiconductors: n- and p-type [31]. When the doping produces an excess of electrons, the semiconductor is called n-type, where n refers to the negative charge of the electron. On the other hand, when the impurities produce an excess of holes, it is called p-type, where p refers to positive due to the absence of electrons.

This practice significantly increases the free carrier density, either electrons or holes, which makes it highly applicable to electronic devices. A highly relevant case that currently leads the technological field due to the interesting properties it offers is silicon (Si). A Si-based n-type semiconductor is created when, in a Si

lattice, an atom is replaced by a Group V species such as phosphorus, arsenic, antimony, and so on. That is, a tetravalent Si atom (four valence electrons) is substituted by a pentavalent impurity (five valence electrons). We can note that there will be an extra unbound electron by each impurity added, which contributes to the majority of carriers being electrons. These impurities that provide an extra electron are known as donors. In an energy level diagram, it can be depicted as Fig. 2.9, where the Fermi level lies between the donor energy level and the conduction band. However, when Si atoms are replaced by a Group III species, the electrons become the minority carriers. This is because the atoms such as boron, aluminium, gallium and so on, are trivalent impurities (three valence electrons), which means that instead of contributing an extra electron, a hole is created, with holes being the majority carriers. These types of impurities that create holes are known as acceptors, creating p-type semiconductor. In an energy level diagram, as shown the Fig. 2.9, unlike the n-type, the Fermi level here lies between the valence band and the acceptor energy level [31].

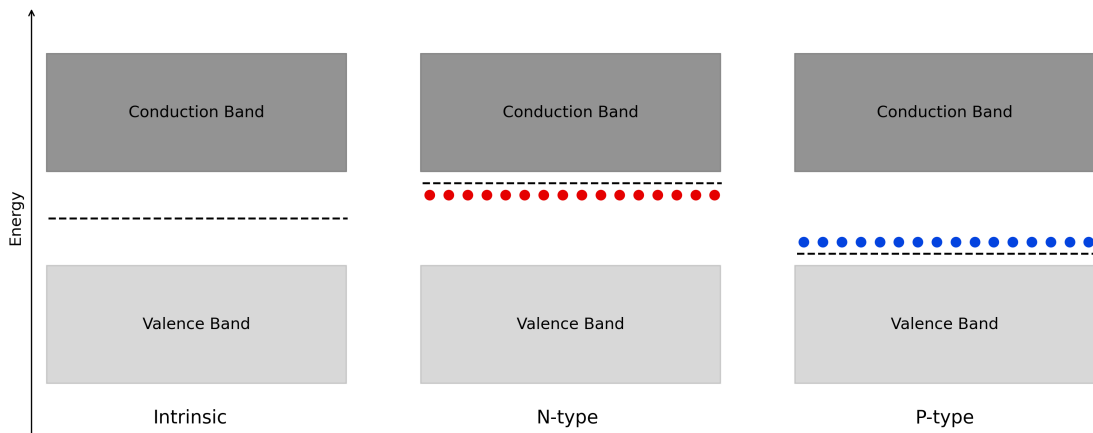


Figure 2.9: Energy level diagrams for intrinsic and extrinsic semiconductors. The panel on the left side depicts the intrinsic semiconductor, that is, without doping. The figure in the middle shows the n-type semiconductor, which is characterized by having extra electrons close to the conduction band. Finally, the right panel shows the p-type semiconductor, where the holes are the majority carriers. The dashed lines represent the Fermi level, red balls are the electrons, and blue balls are the holes.

The behavior of electrons as a function of the probability of occupation of energy states can be described by the Fermi-Dirac distribution function  $f(E)$  at a given temperature ( $T$ ). This function is given as:

$$f(E) = \frac{1}{1 + e^{(E-E_F)/k_B T}}, \quad (2.30)$$

where  $E_F$  is the Fermi energy and  $k_B$  is the Boltzmann's constant. We can note that this distribution depends strongly on the temperature, and that when  $E = E_F$  the probability of finding the state occupied by an electron is 50 %. The number

of available states in the material is defined by the density of states (DOS). This concept tells us how many energy states are accessible to be occupied by electrons. In semiconductors, this can be defined for both the conduction band and the valence band as:

$$g_C(E) = \frac{1}{2\pi^2} \left( \frac{2m_n^*}{\hbar^2} \right)^{3/2} \sqrt{E - E_{CBM}}, \quad (2.31)$$

$$g_V(E) = \frac{1}{2\pi^2} \left( \frac{2m_p^*}{\hbar^2} \right)^{3/2} \sqrt{E_{VBM} - E}, \quad (2.32)$$

where  $g_C(E)$  is the density of states in the conduction band,  $g_V(E)$  is the density of states in the valence band, and  $\hbar$  is the reduced Planck constant. Moreover,  $m_n^*$  and  $m_p^*$  represent the effective masses of electrons and holes, respectively. These effective masses are defined based on the interaction between electrons and holes with the periodic potential created by the lattice. Both effective masses are defined in the same way, since the bands exhibit quadratic behavior, either near the conduction band or the valence band:

$$\frac{1}{m_n^*} = \frac{1}{m_p^*} = \frac{1}{\hbar^2} \frac{d^2E}{dk^2}. \quad (2.33)$$

Visually, this can be identified by the curvature of the band: flatter bands have a larger effective mass, whereas steeper bands have a lower effective mass. Furthermore, take into account that effective mass can be negative.

On the other hand, carrier concentrations can be determined using the density of states and the Fermi-Dirac distribution function. Electron concentration in the conduction band is given as:

$$n = \int_{E_{CBM}}^{\infty} g_C(E)f(E)dE, \quad (2.34)$$

where by replacing Eqs. 2.30 and 2.31, we find that:

$$n = N_C e^{-(E_{CBM} - E_F)/k_B T}. \quad (2.35)$$

$N_C$  is an effective density of states, which contains the effective mass, defined by:

$$N_C = 2 \left( \frac{2\pi m_n^* k_B T}{\hbar^2} \right)^{3/2}. \quad (2.36)$$

Analogously, we can define the hole concentration in the valence band as:

$$p = \int_{-\infty}^{E_{VBM}} g_V(E)[1 - f(E)]dE, \quad (2.37)$$

where, once again, by replacing Eqs. 2.30 and 2.32, the hole concentration can be rewritten as:

$$p = N_V e^{-(E_F - E_{VBM})/k_B T}. \quad (2.38)$$

In this case, the effective density of states  $N_V$  is defined similarly to Eq. 2.36, with the difference being that  $m_p^*$  is replaced by  $m_n^*$ . If we assume the description of an intrinsic semiconductor, then the concentrations will be given by:

$$n_i = p_i = \sqrt{N_C N_V} e^{-E_g / 2k_B T}, \quad (2.39)$$

where  $E_g$  has already been defined in Eq. 2.29.

## 2.5 Defects in crystalline materials

Materials found in nature or produced through growth methods contain inevitable imperfections in their structure, making it impossible to achieve pure materials. However, the level of these imperfections can be reduced through highly sophisticated methods, allowing for the discovery of useful properties in a wide range of applications. These imperfections, also called defects, are flaws within the crystalline structure, which can be classified based on their dimensionality as follows: Point defects (0D), line defects (1D), surface defects (2D), and volume defects (3D) [26], [27]. The focus of this section will be exclusively on point defects.

### 2.5.1 Point defects

Point defects are zero-dimensional (0D) defects consisting of only one or a few atoms, which affect only their surroundings. They are known as 0D because they are confined at a single point or a very small region within the crystal structure. These types of defects can be classified into the following groups.

- Vacancy: it is characterized by the absence of an atom from its lattice position. The notation used for this defect is given as  $V_X$ , where  $V$  refers to the vacancy and the subscript  $X$  represents the chemical symbol of the absent or removed atom.
- Interstitial: occurs when an atom is positioned in a location other than those defined by the lattice positions. The notation used is  $X_i$ , where  $X$  represents the chemical symbol of the added atom, and the subscript  $i$  refers to the interstitial.
- Antisite: occurs when an atom occupies a lattice position different from its original position. This type of defect is observed in crystal lattices where two types of atoms exist ( $X$  and  $Y$ ), such that atom  $X$  can replace atom  $Y$  or vice versa. The notation is given as  $X_Y$ .
- Substitutional: occurs when a foreign atom  $Z$  replaces a host atom  $Y$ . The notation is the same as the antisite case:  $Z_Y$ .
- Frenkel pair: results from the displacement of an atom from its original lattice position to a nearby interstitial position, leaving behind a vacancy. The combination of the interstitial atom and the vacancy makes up the defect.

- Schottky defect: occurs when an equal number of anions and cations are removed from the crystal lattice, leaving vacancies. This type of defect preserves the material's electrical neutrality.
- Complexes: composed of at least two individual defects, such as vacancy-vacancy (divacancy), antisite-vacancy, Frenkel, Schottky, and so on.

**Fig. 2.10** shows a two-dimensional representation of the defects mentioned above in a material composed of two types of atomic species. When defects involve only host atoms, they are called native or intrinsic. These host atoms can give rise to defects such as vacancies, antisites, interstitials, substitutions, or even complex defects, as seen in **Fig. 2.10a-2.10d**, **2.10f**, **2.10g**, and **2.10i**. Respectively, the defects involving foreign atoms are called extrinsic; they can create interstitial, substitutions, and complex defects, as shown in **Fig. 2.10e**, **2.10h**, and **2.10k**. Note that the combination of a host atom with a foreign atom can also create a complex defect, as shown in **Fig. 2.10j**. On the other hand, although Frenkel and Schottky defects also involve host atoms, they are mentioned separately, since they are typically observed in ionic materials. Examples are shown in **Fig. 2.10l** and **2.10m**.

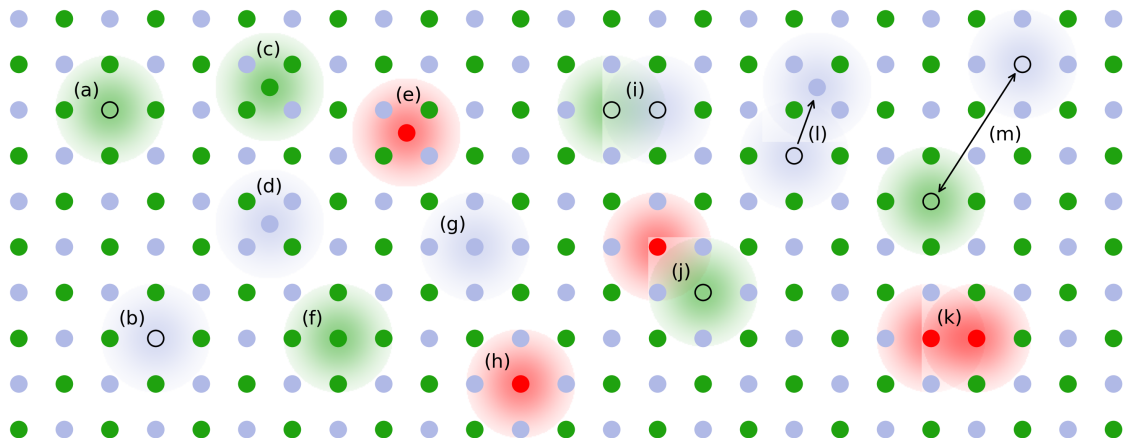


Figure 2.10: Representation of point defects in a material with two atomic species, where (a) and (b) are vacancies; (c) and (d) are interstitial; (e) is also an interstitial, but it is caused by a foreign atom; (f) and (g) are antisites; (h) is a substitutional defect, where a host atom has been replaced by a foreign atom; (i), (j) and (k) are complex defects composed of different single defects; (l) is the Frenkel pair defect and finally (m) is a Schottky defect. Host atoms are depicted by green and gray balls, while foreign atoms are depicted by red balls.

### 2.5.2 Thermodynamic approach

Now that we know that perfect materials do not exist at temperatures above absolute zero ( $T > 0$ ), we can ask ourselves in what proportion or concentration such defects exist. A very useful way to understand this is through the thermodynamics of the system [32].

A crystalline system is in a state of thermodynamic equilibrium — characterized by constant variables such as temperature and pressure — when its Gibbs

free energy reaches a minimum. However, this equilibrium state is not devoid of defects; even at finite temperatures, there are inherently present imperfections, as atoms gain enough energy to move to positions other than their original ones, thus creating vacancies. To find the equilibrium concentration of these vacancies, we can start by assuming that in a given crystal system, there are  $n$  vacancies and  $N$  lattice positions. The change in Gibbs free energy will then be given as:

$$\Delta G = G - G_0, \quad (2.40)$$

where  $G$  is the Gibbs free energy for the crystal system with vacancies, and  $G_0$  is the Gibbs free energy for a reference system (perfect crystal system). This last equation can be rewritten as:

$$\Delta G = \Delta H - T\Delta S. \quad (2.41)$$

Here,  $\Delta H$  is the change in enthalpy and  $\Delta S$  the change in entropy associated with the formation of vacancies. Furthermore,  $\Delta H$  can be expressed in terms of the enthalpy of formation of a single vacancy ( $\Delta h$ ),

$$\Delta H = n\Delta h. \quad (2.42)$$

On the other hand,  $\Delta S$  can be expressed as the sum of the change in vibrational entropy and the change in configurational entropy:

$$\Delta S = \Delta S_{vib} + \Delta S_{conf}. \quad (2.43)$$

$\Delta S_{vib}$  arises due to the vibrations of the atoms in the vicinity of the vacancy, and is expressed as:

$$\Delta S_{vib} = n\Delta s_{vib}, \quad (2.44)$$

where  $\Delta s_{vib}$  is the change in vibrational entropy per vacancy. Subsequently,  $\Delta S_{conf}$  is associated with the different ways in which vacancies can be distributed in the lattice positions. This is determined by Boltzmann formula,

$$\Delta S_{conf} = k_B \ln \left( \frac{\Omega}{\Omega_0} \right) = k_B \ln \Omega, \quad (2.45)$$

where  $k_B$  is the Boltzmann constant,  $\Omega_0$  is the number of possible configurations in the reference system, and its value is 1 since the reference system has only one configuration; and  $\Omega$  is the number of ways to distribute the vacancies in the lattice points. This latter can be expressed as:

$$\Omega = \binom{N}{n} = \frac{N!}{n!(N-n)!}. \quad (2.46)$$

If we rewrite Eq. 2.41 using Eqs. 2.42 - 2.46, we find that:

$$\Delta G = n(\Delta h - T\Delta s_{vib}) - T k_B \ln \left( \frac{N!}{n!(N-n)!} \right). \quad (2.47)$$

To find the equilibrium concentration, we must minimize  $\Delta G$ , which implies:

$$\frac{\partial \Delta G}{\partial n} \Big|_{n=n_{eq}} = 0. \quad (2.48)$$

At this point, we can see that the most complicated term to derive will be the second term in [Eq. 2.47](#). However, using Stirling's approximation, which approximates factorials for large numbers, simplifies the derivative,

$$\ln x! = x \ln x - x. \quad (2.49)$$

After solving [Eq. 2.48](#), we find that the equilibrium concentration  $x_v$  is given by:

$$x_v = \frac{n_{eq}}{N} = \exp\left(\frac{\Delta s_{vib}}{k_B}\right) \exp\left(-\frac{\Delta h}{k_B T}\right), \quad (2.50)$$

where we can see that it depends strongly on temperature.

### 2.5.3 Point defects for quantum technologies

Quantum technology has opened a new era of innovation by harnessing the principles of quantum mechanics. This cutting-edge field uses principles such as entanglement and superposition to develop advanced technologies, including quantum computers. These quantum computers use qubits as their basic units of information. Qubits serve the same function as bits in classical computers, but offer a significant advantage: they can exist in a superposition of their basic units. Nevertheless, the scope of quantum technology extends beyond quantum computing, including fields such as quantum communication, quantum sensing and so on [[1](#)]. However, all these applications share a common fundamental unit: the qubit.

Therefore, a primary challenge is to identify platforms that house the qubits. There are currently several potential platforms such as superconducting qubits, trapped ions, quantum dots, topological qubits, and solid-state qubits [[1](#)]. Superconducting qubits are well-established today; however, they face challenges related to scalability, short coherence times, and operation at cryogenic temperatures. On the other hand, defect-based solid-state qubits are particularly promising due to their capacity to operate at room temperature and their long coherence times. A wide range of host semiconductor materials, including diamond, silicon carbide, aluminum nitride, and boron nitride, can be utilized for this purpose. Notably, the nitrogen-vacancy (NV) center in diamond stands out as the most recognized example of a defect-based qubit.

Although the characteristics that make a host semiconductor material suitable as a platform for quantum technologies are not yet well-defined or mature, some initial conditions must be met, such as a wide band gap, weak spin-orbit interaction and host elements with zero nuclear spin [[33](#)]. On the other hand, when a point defect is introduced into the host semiconductor material, certain conditions or criteria must also be met for it to be considered a promising defect for quantum technology applications. Although most promising defects have

been discovered by chance alone, these criteria have been proposed mostly based on the NV center in diamond [33]. The criteria are described as follows:

#### Requirements for Point Defect-Based Qubits

- A. The point defect must introduce energy levels within the band gap of the host material.
- B. The energy levels must give rise to highly localized electronic states.
- C. The highly localized states must be optically active.
- D. The point defect must exhibit a paramagnetic ground state.
- E. The spin state must exhibit long coherence times.

When a defect is created in a host material, it tends to alter the electronic structure, potentially introducing energy levels within the band gap that did not exist in the pristine material. These new energy levels are particularly important since they represent charge transition levels. Furthermore, the states (electrons or holes) associated with these energy levels must be highly localized, which in turn requires that the desirable energy levels lie near the mid-gap. This ensures their isolation from the valence and conduction bands and, consequently, their strong localization. In addition, an optical cycle between a ground state and an excited state must be allowed. This phenomenon can occur through a capture process, where the charge state changes, or through internal excitation, where the charge state is not altered [7]. An important quantity to identify at this stage is the zero phonon line, along with its corresponding wavelength, which is desirable in the visible or telecom windows. On the other hand, the point defect must be paramagnetic, meaning it should possess a desired spin state of  $1/2$  or  $1$ . This condition enables effective spin manipulation using external magnetic fields. Finally, the spin state must have a long lifetime to ensure that no information is lost. Therefore, it is advantageous for the host material to have zero nuclear spin, as this helps prevent decoherence. However, this requirement is not strictly essential [34].

## 2.6 Cubic boron nitride

Cubic boron nitride (c-BN) is an insulating material due to its large band gap. However, it can become a wide band gap semiconductor through doping. It was predicted through machine learning methods as a suitable candidate for quantum technologies [35]. Its properties such as a wide band gap and low spin-orbit coupling, which are similar to those of diamond, have drawn researchers attention to this material in recent years [33]. Efforts to exploit the properties of this material have focused mainly on point defects.

### 2.6.1 Crystal structure

c-BN is a material with an FCC structure, which is similar to the diamond structure known as zinc-blende. The material is composed of boron (B) and nitrogen (N) atoms, where its primitive cell contains only 2 atoms as shown **Fig. 2.11a**, whereas its conventional cell contains 8 atoms as shown **Fig. 2.11b**. Take into account that both cells allow the crystal to be reconstructed using translational symmetry, but the parameters of the conventional cell are usually reported since it is more symmetrical than the primitive cell. This was discussed in **Section 2.1.2**.

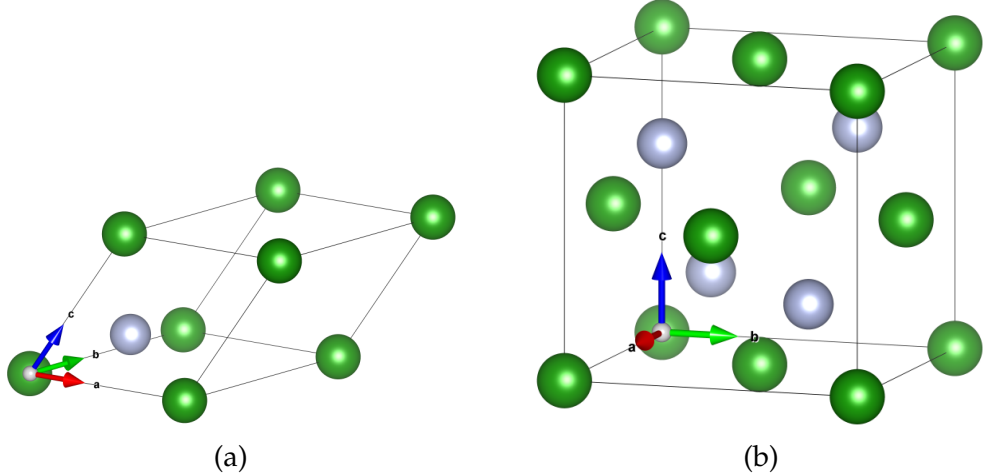


Figure 2.11: c-BN crystal structure, where the (a) primitive cell is a triclinic cell with 2 atoms and (b) conventional cell is a FCC cell with 8 atoms. The figures were designed with VESTA [36].

The experimental lattice parameters for the conventional cell are  $a = b = c = 3.616 \text{ \AA}$  [37], where as expected, in a cubic cell  $\alpha = \beta = \gamma = 90^\circ$ . The band gap is indirect, from  $\Gamma$  to  $X$ , with a value of 6.36 eV [38]. Since the c-BN has a FCC structure, it generate a BCC lattice in reciprocal space, with the truncated octahedron being its 1BZ. The high symmetry points in this 1BZ are given as  $\Gamma$ ,  $X$ ,  $L$ ,  $W$ ,  $U$  and  $K$  [39]. The coordinates of the high symmetry points and their representation in the 1BZ are shown in **Fig. 2.12** and **Table 2.13**.

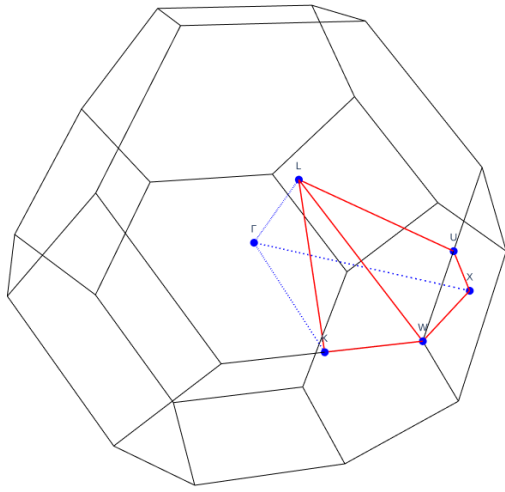


Figure 2.12: Distribution of high symmetry points in the 1BZ.

Figure 2.13: High symmetry points and their respective coordinates.

High symmetry point	Coordinates
$\Gamma$	(0, 0, 0)
$X$	$(\frac{1}{2}, 0, \frac{1}{2})$
$L$	$(\frac{3}{8}, \frac{3}{8}, \frac{3}{4})$
$W$	$(\frac{1}{2}, \frac{1}{2}, \frac{1}{2})$
$U$	$(\frac{5}{8}, \frac{1}{4}, \frac{5}{8})$
$K$	$(\frac{1}{2}, \frac{1}{4}, \frac{3}{4})$

## 2.6.2 Point defects in c-BN

In this thesis, we have taken as a starting point the available literature on the host material c-BN to gather a moderate range of information about the candidate defects. This small database includes native defects, impurity-based defects, and combinations of both in the form of complex defects. The methodology for the screening process is explained in **Section 4.9**. However, a list of the defects included in the database is provided in **Table 2.2**.

Table 2.2: A database of candidate defects gathered from the available literature.

Types	Defects
Native	$V_B, V_N, B_N, N_B$
Impurity	$C_B, C_N, O_B, O_N$
Complex	$V_B - C_B, V_N - C_N, B_N - V_B,$ $N_B - V_N, V_B - V_N, C_B - V_N,$ $C_N - V_B, V_B - O_N, V_B - Si_B,$ $C_B - C_N, C_B - C_B, C_N - C_N$

After the analysis, four defects have emerged as promising candidates for use in qubit platforms. A native defect, involving the substitution of a boron atom by a nitrogen atom  $N_B$ ; a complex defect composed of single native defects, specifically boron and nitrogen vacancies  $V_B - V_N$ ; and two impurity-based complex defects. These two latter are composed of a boron vacancy combined with a substitutional impurity. In the first case, the impurity is a carbon atom replacing a boron atom  $V_B - C_B$ ; in the second, it is a silicon atom replacing a boron atom  $V_B - Si_B$ . These defects are represented in the **Fig. 2.14**, where the definitions given in **Section 2.5** have been taken into account for their design.

The defects selected for the study of this thesis are the same as those previously described, but associated with a charge state. For  $N_B$ , a charge state +1 is of interest, while all complex defects are studied in the neutral charge state. The notation is given as follows:  $N_B^{+1}$ ,  $(V_B - V_N)^0$ ,  $(V_B - C_B)^0$  and  $(V_B - Si_B)^0$ , respectively.

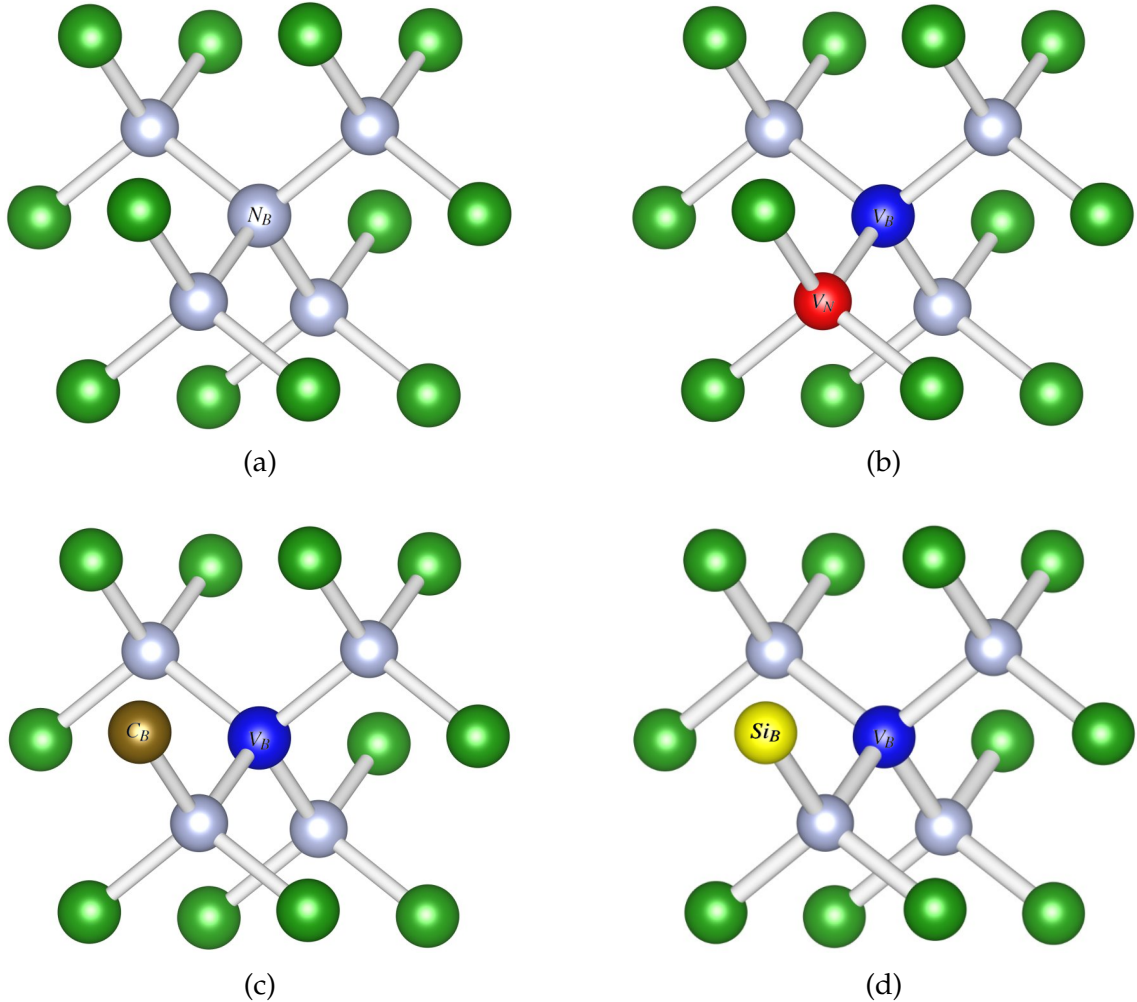


Figure 2.14: Promising defects for quantum technologies in c-BN: (a)  $N_B$ , (b)  $V_B - V_N$ , (c)  $V_B - C_B$  and (d)  $V_B - Si_B$ . Here, the green balls are boron and the gray balls are nitrogen. The figures were designed with VESTA [36].

# Chapter 3

## Fundamentals of Density Functional Theory

This chapter provides an introduction to the fundamental concepts of quantum mechanics for the analysis of many-body systems, as well as a review of the essential components needed to formulate Density Functional Theory (DFT). The starting point will be the formulation of the Schrödinger equation for the many-body problem, which will be separated into two pseudo-independent problems through the Born-Oppenheimer approximation. Then, the issue of the symmetry of the wavefunction will be addressed through the Hartree and Hartree-Fock approximations. This will be important for a good understanding of the final section, which includes the development of the Hohenberg-Kohn theorems and the Kohn-Sham equations.

### 3.1 Quantum mechanics in many-body systems

Our curiosity to understand the fundamental phenomena in nature leads us to confront interacting systems, that is, systems with many particles that interact with each other on either a microscopic or macroscopic level. The many-body problem is a problem of great historical significance for the physicists and mathematicians.

In solid state physics, materials are composed of thousands of particles which we can treat as a many-body problem but it will be necessary to use the laws of quantum mechanics for a good description.

Facing a problem like that is a huge challenge even using numerical calculations, since in the quantum world we must use the Schrödinger equation, which is impossible to solve exactly for large systems. However, it can be solved using certain approximations. Some of these are outlined below.

#### 3.1.1 The Schrödinger equation

The starting point of our study will be crystal systems, where we must take into account the behavior of nuclei and electrons. These considerations introduce

Coulomb interactions such as those between electron-electron, nucleus-nucleus or nucleus-electron. Therefore, the Schrödinger equation is given by

$$\hat{H}^{en}\Psi^{en}(\mathbf{r}, \mathbf{R}) = E^{en}\Psi^{en}(\mathbf{r}, \mathbf{R}), \quad (3.1)$$

where  $e$  refers to electrons and  $n$  to nuclei. In Eq. 3.1 we have included the positions for the electrons ( $\mathbf{r}$ ) and nuclei ( $\mathbf{R}$ ). The wavefunction  $\Psi(\mathbf{r}, \mathbf{R})$  contains all the information or properties of crystal system.  $E^{en}$  is the total energy and  $\hat{H}^{en}$  the Hamiltonian, which contains the interactions between electrons, nuclei and any external potentials.

The Hamiltonian for the many-body problem will be split into two terms [40],

$$\hat{H}^{en} = \hat{H}_{el} + \hat{H}_n, \quad (3.2)$$

where  $\hat{H}_{el}$  and  $\hat{H}_n$  are the hamiltonians for electrons and nuclei. The first Hamiltonian is given as

$$\hat{H}_{el} = \hat{T}_i + \hat{U}_{ij} + \hat{U}_{i\alpha}, \quad (3.3)$$

$$\hat{H}_{el} = - \sum_{i=1}^{N_e} \frac{\hbar^2 \nabla_i^2}{2m_e} + \frac{1}{4\pi\epsilon_0} \sum_{i < j}^{N_e} \frac{q^2}{|\mathbf{r}_i - \mathbf{r}_j|} - \frac{1}{4\pi\epsilon_0} \sum_{i,\alpha}^{N_e, N_n} \frac{q^2 Z_\alpha}{|\mathbf{r}_i - \mathbf{R}_\alpha|}, \quad (3.4)$$

while the second Hamiltonian is

$$\hat{H}_n = \hat{T}_\alpha + \hat{U}_{\alpha\beta}, \quad (3.5)$$

$$\hat{H}_n = - \sum_{\alpha=1}^{N_n} \frac{\hbar^2 \nabla_\alpha^2}{2m_\alpha} + \frac{1}{4\pi\epsilon_0} \sum_{\alpha < \beta}^{N_n} \frac{q^2 Z_\alpha Z_\beta}{|\mathbf{R}_\alpha - \mathbf{R}_\beta|}. \quad (3.6)$$

From Eqs. 3.3 and 3.5,  $\hat{T}$  is the total kinetic energy for all electrons (index  $i$ ) with mass  $m_e$  or for all nuclei (index  $\alpha$ ) with mass  $m_\alpha$ .  $\hat{U}_{ij}$  is the repulsive interaction between electron-electron,  $\hat{U}_{i\alpha}$  is the attractive interaction between electron-nucleus and  $\hat{U}_{\alpha\beta}$  is the repulsive interaction between nucleus-nucleus.

Before we explain some important considerations, keep in mind that the number of electrons in a system is represented by  $N_e$  and for nuclei by  $N_n$ . In the second term on the right in Eqs. 3.4 and 3.6, we must take care to neglect the self-interaction between electrons and nuclei. Restrictions such as  $i \neq j$  and  $\alpha \neq \beta$  allow to do so, besides remove the double counting with  $i < j$  and  $\alpha < \beta$ . Here,  $q$  is the charge and  $Z_\alpha$  or  $Z_\beta$  is the atomic number.

### 3.1.2 Born-Oppenheimer approximation

The fundamental premise of this approach is related to the mass of the atomic nucleus and the electron [41]. Since the atomic nuclei are much heavier than electrons, these can be considered with fixed positions and their reaction to changes in their surroundings is slower. Movement of the electrons is faster given their mass, that is,  $m_e \ll m_\alpha$ .

Using these considerations, we can separate the wavefunction into a product of two functions

$$\Psi^{en}(\mathbf{r}, \mathbf{R}) = \Psi^{en}(\mathbf{r}_1, \mathbf{r}_2, \dots, \mathbf{r}_{N_e}, \mathbf{R}_1, \mathbf{R}_2, \dots, \mathbf{R}_{N_n}), \quad (3.7)$$

$$\Psi^{en}(\mathbf{r}, \mathbf{R}) \simeq \Psi(\mathbf{r}, \mathbf{R})\Phi(\mathbf{R}), \quad (3.8)$$

where  $\Psi(\mathbf{r}, \mathbf{R})$  is the electronic part, while  $\Phi(\mathbf{R})$  is the nuclear part. The Hamiltonian can also be split into two terms as shown in Eq. 3.2 (electronic and nuclear), where each Hamiltonian is given by Eqs. 3.4 and 3.6.

These two assumptions, a separable wavefunction and splitting the Hamiltonian into a nuclear and an electronic part, allow us to build two pseudo-independent equations

$$\hat{H}_{el}\Psi(\mathbf{r}, \mathbf{R}) = E_{el}(\mathbf{R})\Psi(\mathbf{r}, \mathbf{R}), \quad (3.9)$$

$$[\hat{H}_n + E_{el}(\mathbf{R})]\Phi(\mathbf{R}) = E^{en}\Phi(\mathbf{R}). \quad (3.10)$$

Both equations are Schrödinger type, i.e., eigenvalue equations. Eqs. 3.9 and 3.10 are referred to as pseudo-independent because they are coupled through the total electronic energy  $E_{el}(\mathbf{R})$ . We can note that Eq. 3.9 depends on the nuclear configuration, that is, the electronic Hamiltonian, eigenstates and eigenvalues depend only parametrically on  $\mathbf{R}$ . This approximation allows us to calculate the electronic structure of a crystal without describing the behavior of the nuclei.

To compute the total energy of the system,  $E^{en}$ , we must first solve the electronic Schrödinger equation. Once we have done this, we can write an effective Hamiltonian for the nuclei

$$\hat{H}_{eff} = \hat{H}_n + E_{el}(\mathbf{R}) \quad (3.11)$$

$$= \hat{T}_\alpha + \hat{U}_{\alpha\beta} + E_{el}(\mathbf{R}). \quad (3.12)$$

Since the movement of the nuclei is considered to be infinitely slow compared to the movement of electrons, the first term on the right in Eq. 3.12 can be neglected ( $\hat{T}_\alpha = 0$ ). The effective Hamiltonian is called the potential energy surface (PES), which is the sum between the nucleus-nucleus interaction and total electronic energy, and describes the potential energy of the nuclei in terms of their positions. In other words, Eq. 3.12 can be rewritten as

$$E_p(\mathbf{R}) = \hat{U}_{\alpha\beta} + E_{el}(\mathbf{R}). \quad (3.13)$$

### 3.1.3 Hartree method

Although we have managed to separate the Schrödinger equation into two parts, electronic and nuclear, for both the Hamiltonian and the wavefunction through the Born-Oppenheimer approximation, the electronic wavefunction  $\Psi(\mathbf{r}, \mathbf{R})$  still depends on the position of all electrons.

To simplify this further, we can employ the Hartree approximation where the wavefunction for a system with  $N$  electrons can be approximated as a product of single-electron wavefunctions [42], [43]:

$$\Psi(\mathbf{r}_1, \mathbf{r}_2, \dots, \mathbf{r}_N) = \psi_1(\mathbf{r}_1)\psi_2(\mathbf{r}_2)\dots\psi_N(\mathbf{r}_N). \quad (3.14)$$

However, this approximation has strong limitations since it does not take into account the electron correlation or exchange interaction, where the electronic correlation is associated with how the movement of an electron is influenced by the presence of all other electrons in the system. Therefore, neglecting electron correlation introduces a mean-field approximation, where each electron moves in an average potential created by the other electrons ( $N - 1$ ).

The lack of exchange interaction is due to the symmetry of the wavefunction. Since the electrons are indistinguishable fermions and obey the Pauli exclusion principle, the wavefunction that satisfies these considerations must be antisymmetric, however we note that Eq. 3.14 is symmetric.

### 3.1.4 Hartree-Fock method

Fock improved the Hartree method by introducing the exchange interaction [44]. For that, the wavefunction was reformulated as a Slater determinant [45], which ensures the Pauli exclusion principle for fermions and thus antisymmetric wavefunction [46]. Now the wavefunction for the same system in Eq. 3.14 can be rewritten as a determinant of single-electron wavefunctions:

$$\Psi(\mathbf{r}_1, \mathbf{r}_2, \dots, \mathbf{r}_N) = \frac{1}{\sqrt{N!}} \begin{vmatrix} \psi_1(\mathbf{r}_1) & \psi_2(\mathbf{r}_1) & \dots & \psi_N(\mathbf{r}_1) \\ \psi_1(\mathbf{r}_2) & \psi_2(\mathbf{r}_2) & \dots & \psi_N(\mathbf{r}_2) \\ \vdots & \vdots & \ddots & \vdots \\ \psi_1(\mathbf{r}_N) & \psi_2(\mathbf{r}_N) & \dots & \psi_N(\mathbf{r}_N) \end{vmatrix}, \quad (3.15)$$

where  $(N!)^{-1/2}$  is a normalization factor. The properties of the determinant are in keeping with the Pauli exclusion principle through the interchange of two rows or columns, since that interchange will modify the sign of the total wavefunction.

However, electron correlation is still neglected, so electrons are still treated through the mean field approximation. There are post-Hartree-Fock methods to include the electron correlation such as Configuration Interaction, Coupled Cluster, Møller-Plesset perturbation theory and so on.

## 3.2 Foundations of the Density Functional Theory

### 3.2.1 The Hohenberg-Kohn theorems

The initial approach to Density Functional Theory (DFT) takes as a key point the ground state electron density  $n(\mathbf{r})$ , which like the wavefunction, contains all the information of the system. This premise is set out within two fundamental theorems known as Hohenberg-Kohn theorems [47], where the electron density in three dimensions is given by

$$n(\mathbf{r}) = |\Psi(\mathbf{r}_1, \mathbf{r}_2, \dots, \mathbf{r}_N)|^2. \quad (3.16)$$

## 1. Theorem I: Existence Theorem

### Theorem I

Given a stationary quantum mechanical system, any observable (including energy) can be calculated (in principle exactly) by knowing only the **ground state electron density**,

$$E = F[n_{gs}(\mathbf{r})].$$

$E$  is the total energy, and it is a functional ( $F$ ) of the ground state electron density  $n_{gs}(\mathbf{r})$ . This first theorem can be proven through contradiction.

**Proof:**

We begin by assuming that  $n_{gs}(\mathbf{r})$  is known and  $\Psi_{gs}$  is non-degenerate. So given a  $n_{gs}(\mathbf{r})$  for two different systems ( $A$  and  $B$ ), there must exist different potentials, Hamiltonians, wavefunctions and energies:

Table 3.1: Assumptions to prove **HK Theorem I** by contradiction.

	A	B
Potentials	$V_{ext}$	$V'_{ext}$
Hamiltonians	$H$	$H'$
Wavefunctions	$\Psi$	$\Psi'$
Energies	$E_0 = \langle \Psi   H   \Psi \rangle$	$E'_0 = \langle \Psi'   H'   \Psi' \rangle$

If  $|\Psi'\rangle$  is not an eigenstate of  $H$ , then

$$E_0 < \langle \Psi' | H | \Psi' \rangle = \langle \Psi' | H' | \Psi' \rangle + \langle \Psi' | H - H' | \Psi' \rangle, \quad (3.17)$$

$$= E'_0 + \int n(\mathbf{r}) [V_{ext} - V'_{ext}] d\mathbf{r}. \quad (3.18)$$

Therefore,

$$E_0 < E'_0 + \int n(\mathbf{r}) [V_{ext} - V'_{ext}] d\mathbf{r}. \quad (3.19)$$

For the other wavefunction  $\Psi$  and hamiltonian  $H'$ ,

$$E'_0 < \langle \Psi | H' | \Psi \rangle = \langle \Psi | H | \Psi \rangle + \langle \Psi' | H' - H | \Psi \rangle, \quad (3.20)$$

$$= E_0 - \int n(\mathbf{r}) [V_{ext} - V'_{ext}] d\mathbf{r}, \quad (3.21)$$

and

$$E'_0 < E_0 - \int n(\mathbf{r}) [V_{ext} - V'_{ext}] d\mathbf{r}. \quad (3.22)$$

Adding Eqs. 3.19 and 3.22 gives

$$E_0 + E'_0 < E'_0 + E_0. \quad (3.23)$$

We note that Eq. 3.23 contradicts itself. Thus, it is concluded that each physical system has a **ground state electron density**  $n_{gs}(\mathbf{r})$  which defines the total energy exactly.

## 2. Theorem II: Variational Principle

### Theorem II

The **ground state electron density** can be calculated, in principle exactly, using a variational method that involves only the density,

$$F[n] \implies \frac{\delta F[n]}{\delta n} \implies n_{gs}(\mathbf{r}).$$

To apply the variational principle, a constraint must be considered: the number of electrons  $N$  must remain constant. The  $n_{gs}(\mathbf{r})$  term is an extremal, which allow us to minimize the functional of energy.

#### Proof:

Let  $n(\mathbf{r}) \geq 0$ , where  $n(\mathbf{r})$  is a trial density (we do not know if it is the ground state) and the number of particles  $N$  is given by

$$N = \int n(\mathbf{r}) d\mathbf{r}. \quad (3.24)$$

Therefore, it holds that the trial density functional (trial energy) is the upper bound to the ground state density functional (ground state energy), and when  $n = n_{gs}$ , the functional reaches its minimum value

$$E_0 \hat{=} E[n_{gs}] \leq E[n] = \langle \Psi_{trial} | H | \Psi_{trial} \rangle. \quad (3.25)$$

Furthermore, we can reformulate the constraint on the number of particles as

$$\left( \int n(\mathbf{r}) d\mathbf{r} \right) - N = 0. \quad (3.26)$$

With this information and using the unknown Lagrange-Euler multipliers, we can construct the Lagrange functional

$$L[n] = E[n] - \mu \left( \int n(\mathbf{r}) d\mathbf{r} - N \right). \quad (3.27)$$

The minimization will be given by

$$\delta \left\{ E[n] - \mu \left( \int n(\mathbf{r}) d\mathbf{r} - N \right) \right\} = 0, \quad (3.28)$$

where  $\delta N = 0$ , since  $N$  is a constant. Now we can rewrite Eq. 3.28 as

$$\delta E[n] - \mu \delta \left( \int n(\mathbf{r}) d\mathbf{r} \right) = 0. \quad (3.29)$$

Note: Variation of a functional

$$F[f + \delta f] - F[f] = \delta F, \quad (3.30)$$

$$= \int \left( \frac{\delta F}{\delta f(x)} \right) \delta f(x) dx. \quad (3.31)$$

Through the variation  $\delta E[n]$  it is possible to find that

$$\int \left\{ \frac{\delta E[n(\mathbf{r})]}{\delta n(\mathbf{r})} - \mu \right\} \delta n(\mathbf{r}) d\mathbf{r} = 0, \quad (3.32)$$

and

$$\mu = \frac{\delta E[n(\mathbf{r})]}{\delta n(\mathbf{r})}. \quad (3.33)$$

From this last relation, the Lagrange-Euler multiplier  $\mu$  is the electronic chemical potential of the system. Moreover,  $E[n]$  can be separated into two terms:

$$E[n] = F_{HK}[n] + V_{ext}[n], \quad (3.34)$$

$$= T[n] + V_{ee}[n] + V_{ext}[n], \quad (3.35)$$

where  $F_{HK}[n]$  is the unknown Hohenberg-Kohn functional, which is an universal functional.  $T[n]$  is the kinetic energy functional of the interacting electron system,  $V_{ext}[n]$  is the potential energy functional and  $V_{ee}[n]$  is the interaction energy functional, which takes into account all the electron-electron interactions.

### 3.2.2 The Kohn-Sham equations

The Kohn-Sham approach takes the idea from the Hartree method and uses a product of single-electron wavefunctions, which will be called Kohn-Sham orbitals. Keep in mind that the orbitals are auxiliary wavefunctions, since they do not directly represent the true wavefunctions of the system. According to Hartree theory, we approximate the total electronic wavefunction according to

$$\Psi(\mathbf{r}_1, \mathbf{r}_2, \dots, \mathbf{r}_N) = \phi_1^{KS}(\mathbf{r}_1)\phi_2^{KS}(\mathbf{r}_2)\dots\phi_N^{KS}(\mathbf{r}_N). \quad (3.36)$$

The orthonormality is also a key requirement that orbitals must satisfy, i.e.,

$$\int \phi_i^{*KS}(\mathbf{r})\phi_{i'}^{KS}(\mathbf{r}') d\mathbf{r} d\mathbf{r}' = \delta_{ii'}. \quad (3.37)$$

Additionally, the electron density is given by:

$$n(\mathbf{r}) = \sum_j |\phi_j^{KS}(\mathbf{r}_j)|^2. \quad (3.38)$$

The motivation for the formulation of the Kohn-Sham equations [48] is the search for the ground state electron density, which can minimize the energy functional and give us the exact energy. This energy functional was given in Eq. 3.35, which through certain techniques, can be expressed as

$$E[n] = T_s[n] + V_{ext}[n] + E_H[n] + (T[n] - T_s[n]) + (V_{ee}[n] - E_H[n]), \quad (3.39)$$

where  $T_s[n]$  is the kinetic energy of non-interacting electrons.  $V_{ext}[n]$  is the interaction energy between electrons and external potential.  $E_H[n]$  is the Hartree energy due to the electron-electron repulsion and the last four terms on the right constitute the exchange-correlation energy. This exchange-correlation energy includes all the energy contributions that have not been considered in the other terms such as exchange interaction and electron correlation. Each term is given by:

$$T_s[n] = -\frac{\hbar^2}{2m} \sum_j^N \int \phi_j^{*KS}(\mathbf{r}) \nabla^2 \phi_j^{KS}(\mathbf{r}) d\mathbf{r}, \quad (3.40)$$

$$V_{ext}[n] = \int V_{ext}(\mathbf{r}) n(\mathbf{r}) d\mathbf{r}, \quad (3.41)$$

$$E_H[n] = \frac{1}{2} \frac{q^2}{4\pi\epsilon_0} \iint \frac{n(\mathbf{r}) n(\mathbf{r}')}{|\mathbf{r} - \mathbf{r}'|} d\mathbf{r} d\mathbf{r}', \quad (3.42)$$

$$E_{xc}[n] = (T[n] - T_s[n]) + (V_{ee}[n] - E_H[n]) = \Delta T + \Delta V. \quad (3.43)$$

Now once again we will use the variational method to obtain the ground state energy. Unlike in Eq. 3.28, where the constraint was the number of particles, here we will consider orthonormality. The minimization will be with respect to  $\phi_j^{*KS}(\mathbf{r})$ :

$$\frac{\delta}{\delta \phi_j^{*KS}(\mathbf{r})} \left\{ E[n] - \sum_{i,i'} \lambda_{ii'} \left( \int \phi_j^{*KS}(\mathbf{r}) \phi_{i'}^{KS}(v\mathbf{r}') d\mathbf{r} d\mathbf{r}' - \delta_{ii'} \right) \right\} = 0. \quad (3.44)$$

Performing the calculation, we will find that:

$$\frac{\delta T_s[n]}{\delta \phi_j^{*KS}(\mathbf{r})} = -\frac{\hbar^2}{2m} \nabla_j^2 \phi_j^{KS}(\mathbf{r}), \quad (3.45)$$

$$\frac{\delta V_{ext}[n]}{\delta \phi_j^{*KS}(\mathbf{r})} = V_{ext}(\mathbf{r}) \phi_j^{KS}(\mathbf{r}), \quad (3.46)$$

$$\frac{\delta E_H[n]}{\delta \phi_j^{*KS}(\mathbf{r})} = V_H(\mathbf{r}) \phi_j^{KS}(\mathbf{r}), \quad (3.47)$$

$$\frac{\delta E_{xc}[n]}{\delta \phi_j^{*KS}(\mathbf{r})} = V_{xc}(\mathbf{r}) \phi_j^{KS}(\mathbf{r}), \quad (3.48)$$

where  $V_H(\mathbf{r})$  is the Hartree potential and  $V_{xc}(\mathbf{r})$  is the exchange-correlation potential, both given by:

$$V_H(\mathbf{r}) = \frac{q^2}{4\pi\epsilon_0} \int \frac{n(\mathbf{r}')}{|\mathbf{r} - \mathbf{r}'|} d\mathbf{r}', \quad (3.49)$$

$$V_{xc}(\mathbf{r}) = \frac{\delta E_{xc}[n]}{\delta n(\mathbf{r})}. \quad (3.50)$$

After deriving Eq. 3.44, we obtain the Kohn-Sham equations

$$\left( -\frac{\hbar^2}{2m} \nabla_j^2 + V_{ext}(\mathbf{r}) + V_H(\mathbf{r}) + V_{xc}(\mathbf{r}) \right) \phi_j^{KS}(\mathbf{r}) = \varepsilon_j^{KS} \phi_j^{KS}(\mathbf{r}), \quad (3.51)$$

where  $\varepsilon_j^{KS}$  are Kohn-Sham eigenvalues. Furthermore, we can make it a bit more compact by considering an effective potential  $V_{eff}(\mathbf{r})$  as the sum of the terms  $V_{ext}(\mathbf{r})$ ,  $V_H(\mathbf{r})$  and  $V_{xc}(\mathbf{r})$ ,

$$\left( -\frac{\hbar^2}{2m} \nabla_j^2 + V_{eff}(\mathbf{r}) \right) \phi_j^{KS}(\mathbf{r}) = \varepsilon_j^{KS} \phi_j^{KS}(\mathbf{r}). \quad (3.52)$$

The effective potential is the potential that the electrons will experience. It plays a key role, since it allows us to study an interacting many-electron system as if it were a system composed of non-interacting electrons. The solutions for this set of equations are Kohn-Sham orbitals and Kohn-Sham eigenvalues. Then, through the orbitals, it is possible to obtain the ground state electron density. An important objective is also the true total energy, which is given by:

$$E[n] = \sum_j \varepsilon_j^{KS} - \int V_H(\mathbf{r}) n(\mathbf{r}) d\mathbf{r} + E_{xc}[n] - \int V_{xc}(\mathbf{r}) n(\mathbf{r}) d\mathbf{r}. \quad (3.53)$$

Although we have achieved to formulate the total energy in several known terms, the exchange-correlation term remains unknown. Modeling this exchange-correlation energy is not straightforward; it is the most significant challenge in DFT, which leads to the use of approximations such as Local Density Approximation (LDA), Generalized Gradient Approximation (GGA), or Hybrid Functionals.

# Chapter 4

## Methodology

This chapter will be dedicated to describing the methods required to simulate defects in a host material. Topics such as self-consistent field method, exchange-correlation energy through functionals, convergence tests, chemical potentials, finite-size corrections, formation energy diagrams, optical transitions and spin coherence will be included.

### 4.1 Self-consistent field method

The implementation of the Density Functional Theory (DFT) is done through a self-consistent field method, which is an iterative method that consists of solving the Kohn-Sham equations (Eq. 3.52) and updating the density. The workflow can be framed within a group of steps, where the atomic structure must be specified in advance:

1. Start with an initial guess for the electron density  $n(\mathbf{r})$ .
2. The effective potential will be calculated through the electron density  $n(\mathbf{r})$  (a suitable  $V_{xc}[n]$  functional is chosen).
3. Solve the Kohn-Sham equations.
4. The Kohn-Sham orbitals allow for obtaining a new electron density  $n'(\mathbf{r})$ .
5. Filter: Check if the energy is self-consistent ( $E[n] \approx E[n']$ ).
  - If self-consistency was not reached, repeat step 2 with the new density  $n'(\mathbf{r})$  until it is reached (iterative method).
  - If self-consistency is achieved, output information (energies, forces, pressure and so on) will be provided for the atomic structure.
6. Filter: If the resultant forces are not sufficiently small, the atomic configuration must be updated, that is, repeat from step 2.
7. When the forces are sufficiently small and do not alter the atomic configuration, new output information will be provided, thereby concluding the process.

## 4.2 Exchange-correlation functionals

As we mentioned in [Section 3.2.2](#), obtaining the true form of the exchange-correlation term is a challenge that researchers are actively working on to this day, since determining it would allow us to know the exact energy of a given system. Nevertheless, until now, our best tools to face these challenges have been the approximations. Various approximation methods have been proposed, but only 3 of them will be described here.

### 4.2.1 Local density approximation

The local density approximation (LDA) derives the exchange-correlation energy from a non-interacting uniform electron gas, that is, energy depends only on the local electron density at each point in space. The term is expressed as:

$$E_{xc}^{LDA}[n] = \int n(\mathbf{r})\epsilon_{xc}[n(\mathbf{r})]d\mathbf{r}, \quad (4.1)$$

where  $n(\mathbf{r})$  is the electron density and  $\epsilon_{xc}[n(\mathbf{r})]$  is the exchange-correlation energy per electron. Note that this approximation is only valid when the electron density varies slowly with respect to the position [48]. On the contrary, in systems where the density varies rapidly the approximation fails. A notable example of where LDA fails is the estimation of the band gaps in semiconductors.

### 4.2.2 Generalized-gradient approximation

The generalized-gradient approximation (GGA) is characterized by suggesting that in addition to the dependence on the electron density, its gradient must also be included. The expression is given by:

$$E_{xc}^{GGA}[n] = \int n(\mathbf{r})\epsilon_{xc}[n(\mathbf{r}), \nabla n(\mathbf{r})]d\mathbf{r}, \quad (4.2)$$

where  $\epsilon_{xc}[n(\mathbf{r}), \nabla n(\mathbf{r})]$  is also the exchange-correlation energy per electron, but including the gradient. This makes it much more accurate than LDA and also allows us to consider systems where the electron densities vary significantly. However, this still has shortcomings for a complete and accurate study of semiconductors, since it still underestimates the band gap. Furthermore, it fails to describe strongly correlated systems.

There are several GGA functionals, a family, which are different from each other by certain tunable parameters. These parameters are often modified according to the calculation needs, thus satisfying a specific class of materials. When the parameters are adjusted to match experimental data, they are known as empirical parameters, whereas when they are derived from the first-principles, they are known as non-empirical parameters. An example among this huge family is the PBE functional, which was derived by Perdew, Burke and Ernzerhof [17]. This last functional will be used throughout the thesis.

### 4.2.3 Hybrid functional

This functional is an improvement on the previous cases by using the Hartree-Fock theory. This improvement is due to the combination of exchange-correlation contributions from LDA or GGA functionals with a fraction of the exact Hartree-Fock exchange. This mixture of functionals, as in the GGA case, also creates a variety of hybrid functionals determined by certain parameters. Although the computational cost is significantly increased, the hybrid functionals provides a more accurate description of the systems.

One of the most prominent hybrid functionals is the HSE functional, which was introduced by Heyd, Scuseria and Ernzerhof [18], because it manages to reduce the computational cost without affecting the accuracy. In this functional, they propose the introduction of a screening parameter, which allows the exchange interaction to be decomposed into two components: a long-range (LR) and a short-range (SR) part. This decomposition can be represented as:

$$\frac{1}{r} = \frac{\operatorname{erfc}(\omega r)}{r} + \frac{\operatorname{erf}(\omega r)}{r}, \quad (4.3)$$

where the complementary error function ( $\operatorname{erfc}$ ) represents the SR part, the error function ( $\operatorname{erf}$ ) is the LR part and  $\omega$  is the screening parameter. Note that when  $\omega = 0$ , the LR part is zero, meaning that the entire exchange is treated as Hartree-Fock. On the other hand, when  $\omega \rightarrow \infty$ , the SR part is zero, making the exchange purely semi-local.

Here, only for the SR part contains the exact Hartree-Fock exchange, whereas the LR part is reduced by a screened Coulomb potential, thus assuming the role of a semi-local functional such as PBE. Therefore, the exchange-correlation energy is given as:

$$E_{xc}^{HSE} = \alpha E_x^{HF,SR}(\omega) + (1 - \alpha) E_x^{PBE,SR}(\omega) + E_x^{PBE,LR}(\omega) + E_c^{PBE}, \quad (4.4)$$

where  $\alpha$  is the fraction of the exact Hartree-Fock exchange and the Hartree-Fock exchange energy is give by:

$$E_x^{HF,SR}(\omega) = -\frac{1}{2} \sum_{i,j} \iint d\mathbf{r} d\mathbf{r}' \frac{\operatorname{erfc}(\omega|\mathbf{r} - \mathbf{r}'|)}{|\mathbf{r} - \mathbf{r}'|} \times \psi_i^*(\mathbf{r}) \psi_j^*(\mathbf{r}') \psi_i(\mathbf{r}') \psi_j(\mathbf{r}), \quad (4.5)$$

where  $\psi_i$  and  $\psi_j$  are the wave functions of the  $i$ -th and  $j$ -th electrons at positions  $\mathbf{r}$  and  $\mathbf{r}'$ , and  $r = |\mathbf{r} - \mathbf{r}'|$ . In addition to the PBE functional, the hybrid functional known as HSE06 will also be used in this thesis. Its parameters are defined as  $\alpha = 0.25$  and  $\omega = 0.2$ .

## 4.3 Convergence tests

The computational cost is an important factor to consider in simulations, since it can require significant computational resources. One way to mitigate demanding calculations without compromising the accuracy of the results is to perform convergence testing. The main parameters to be converged before a simulation

are energy cutoff and  $\mathbf{k}$ -density. On the other hand, in a defect study, it is also important to perform convergence tests for supercell size.

Energy cutoff convergence is a treatment to determinate the number of plane wave used to describe wave functions, which are governed by Bloch's theorem. These wave functions are an expansion of plane waves, which contain reciprocal lattice vectors ( $\mathbf{G}$ ) related to the periodicity of the crystal. In an ideal framework, we would need infinite number of plane waves to perform an exact calculation. However, given the limits of computational resources, this is not feasible. To make the calculations computationally feasible, a limit must be imposed by truncating the number of plane waves. Since each plane wave is related to a kinetic energy, we can impose the limit on them in such a way that we control the number of plane waves included in the expansion [49], given by:

$$E_{kin} = \frac{\hbar^2}{2m} |\mathbf{k} + \mathbf{G}|^2 \leq E_{cut}. \quad (4.6)$$

This tells us that only plane waves with kinetic energy less than or equal to the energy cutoff will be included in the expansion. Furthermore, the energy cutoff is:

$$E_{cut} = \frac{\hbar^2}{2m} \mathbf{G}_{cut}^2. \quad (4.7)$$

To carry out this analysis, it is necessary to use several energy cutoffs in different configurations of the same system. The objective of using different configurations is to eliminate systematic errors through energy differences, known as relative energies.

Once the energy cutoff is determined, the next parameter for convergence is the  $\mathbf{k}$ -density. This parameter is associated with the  $\mathbf{k}$ -point mesh in the reciprocal space used in the calculation of the Brillouin integrals. That is, the density of this mesh is determined by the number of points  $\mathbf{k}$  used to sample the reciprocal space in the 1BZ. The integrals to be evaluated are given as:

$$g = \frac{V_{cell}}{(2\pi)^3} \int_{BZ} g(\mathbf{k}) d\mathbf{k} \quad (4.8)$$

where  $V_{cell}$  is the volume of the cell and involves the volume of Brillouin zone by:

$$V_{cell} = \frac{(2\pi)^3}{V_{BZ}}. \quad (4.9)$$

Solving the integrals in Eq. 4.8 computationally is too extensive. Fortunately, the Monkhorst and Pack method reduces the computational cost by exploiting the symmetry of the Brillouin zone [50]. This means that it is not necessary to evaluate the integral over the entire Brillouin zone, but only over a reduced region. Here, the  $\mathbf{k}$ -point mesh is uniform and is centered in the origin,  $\Gamma$ . The analysis process is similar to that of energy cutoff, but using various  $\mathbf{k}$ -densities. Relative energies are also calculated here.

Finally, convergence for supercells aims to find the optimal supercell size for defect calculations. This is because the larger the supercell size, the greater the

computational resources required. However, we must also keep in mind that it should not be too small, since in a defect study we seek to capture properties as accurately as possible. Another important point for the use of supercells is to mitigate the electrostatic interaction between the defect and its periodic images [8]. We can note that once again this convergence involves taking into account a balance between accuracy and computational cost. In this case, several supercells with different sizes will be created by 3D replication of the unit cell.

## 4.4 Chemical potentials

The chemical potential represents the free energy per atom that is absorbed or released when an atom is added or removed from the crystal structure, thus representing the reservoir for the atoms used in the creation of a given defect [8]. These atoms move along a gradient of chemical potential, that means, they tend to move from regions of higher chemical potential to lower ones until reaching equilibrium. In gaseous systems, it depends on variables as pressure and temperature, while in solids, its dependence is more complex, since it relies on the concentration of the element and its interactions within the material.

In materials such as c-BN with only two species, the chemical potentials must satisfy:

$$\mu_{cBN} = \mu_B + \mu_N, \quad (4.10)$$

$$\Delta H_f(cBN) = \mu_{cBN} - \mu_B^{elemental} - \mu_N^{elemental}, \quad (4.11)$$

where  $\mu_{cBN}$  and  $\Delta H_f(cBN)$  represent the chemical potential and the enthalpy of formation of c-BN, while the chemical potentials  $\mu_B$  and  $\mu_N$  are constrained by their most stable phases, given by:

$$\mu_B \leq \mu_B^{elemental}, \quad (4.12)$$

$$\mu_N \leq \mu_N^{elemental}, \quad (4.13)$$

Here  $\mu_i^{elemental}$  are the chemical potentials of the most stable phases of B and N. Both chemical potentials are defined as the total energy per atom. From Eq. 4.10 and the constraints in Eqs. 4.12 and 4.13, we can define the rich conditions for species B (B-rich), given by:

$$\mu_B = \mu_B^{elemental}, \quad (4.14)$$

$$\mu_N = \mu_{cBN} - \mu_B^{elemental}, \quad (4.15)$$

and rich conditions for species N (N-rich), given by:

$$\mu_N = \mu_N^{elemental}, \quad (4.16)$$

$$\mu_B = \mu_{cBN} - \mu_N^{elemental}. \quad (4.17)$$

A useful way to use the chemical potential limits is to take them with respect to elemental chemical potentials. Therefore, B-rich can be redefined as:

$$\mu_B^* = \mu_B - \mu_B^{elemental} = \mu_B^{elemental} - \mu_B^{elemental} = 0, \quad (4.18)$$

$$\mu_N^* = \mu_N - \mu_N^{elemental} = \mu_{cBN} - \mu_B^{elemental} - \mu_N^{elemental}, \quad (4.19)$$

whereas  $N$ -rich is redefined as:

$$\mu_N^* = \mu_N - \mu_N^{elemental} = \mu_N^{elemental} - \mu_N^{elemental} = 0, \quad (4.20)$$

$$\mu_B^* = \mu_B - \mu_B^{elemental} = \mu_{cBN} - \mu_N^{elemental} - \mu_B^{elemental}. \quad (4.21)$$

## 4.5 Finite-size corrections

Finite-size effects arise when studying defects in materials. In first-principles calculations such as DFT, these defects are modeled using supercells to make the simulation as realistic as possible. However, because the supercell is periodically repeated in all directions, spurious interactions arise as a consequence of the interactions between the defects and their periodic images. For example, a charged defect can introduce long-range Coulomb interactions with its neighboring periodic images, thus introducing an overestimation or underestimation of the formation energy. One solution would be to use very large supercells so that the defect and its periodic images are widely separated, thus mitigating spurious interactions. However, this leads to computational problems, since the calculations would be excessively expensive. The convergence for supercell explained in [Section 4.3](#) is a way to reduce these unphysical interactions; however, it is still necessary to introduce corrections.

The Freysoldt-Neugebauer-Van de Walle (FNV) method computes the magnitude of these interactions by introducing charge corrections and potential alignment [51]. The energy correction is expressed as:

$$E_{corr} = E^{lat}[q^{model}] - q\Delta V, \quad (4.22)$$

where  $E^{lat}[q^{model}]$  is the screened lattice energy to a model charge density  $q^{model}$ ,  $q$  is the charge and  $\Delta V$  is an alignment term. The success of this approach is due to the fact that it splits the Coulomb interaction into short-range (SR) and long-range (LR) terms as:

$$V(\mathbf{r}) = V^{SR}(\mathbf{r}) + V^{LR}(\mathbf{r}), \quad (4.23)$$

which allows LR interactions to be treated from a charge density model as:

$$V^{LR}(\mathbf{r}) = \int \frac{q^{model}(\mathbf{r}')}{\epsilon|\mathbf{r} - \mathbf{r}'|} d^3\mathbf{r}, \quad (4.24)$$

while the alignment term is given by:

$$\Delta V = \frac{1}{\Omega} \int V^{SR}(\mathbf{r}) d^3\mathbf{r}, \quad (4.25)$$

where  $\Omega$  is the volume of the supercell and  $\epsilon$ , from [Eq. 4.24](#), is a dielectric tensor. An improved version of the FNV method was given by Kumagai and Oba [52]. This new method, known as extended FNV, introduced the anisotropic form of the dielectric tensor through a point charge model. This latter method is implemented in PyDefect package [51], [52], which will be used to compute the energy corrections in this thesis.

## 4.6 Formation energy

Formation energy is a thermodynamic quantity that represents the amount of energy required to form a defect in a perfect crystal. Furthermore, this energy can be calculated through first-principles calculations.

### 4.6.1 Master equation

The master equation for calculating formation energy relates various terms, each of which can be calculated independently. For a defect with charge  $q$ , the equation is given as:

$$E_{form}^q = E_{def}^q - E_{perf} - \sum_i n_i \mu_i^* + q(E_{Fermi} + E_{VBM}) + E_{corr}, \quad (4.26)$$

where  $E_{form}^q$  is the formation energy,  $E_{def}^q$  is the total energy of the defective supercell,  $E_{perf}$  is the total energy of the perfect supercell, and  $n_i$  is an integer, where  $n_i > 0$  when atoms are added and  $n_i < 0$  when atoms are removed.  $\mu_i^*$  is the chemical potential,  $E_{Fermi}$  is the Fermi level,  $E_{VBM}$  is the valence band maximum (VBM) energy of the host and  $E_{corr}$  is the energy correction. Sometimes the fourth and fifth term on the right-hand side is represented as:

$$\mu_e = E_{Fermi} + E_{VBM}, \quad (4.27)$$

where  $\mu_e$  is known as electronic chemical potential.

### 4.6.2 Diagram

Once all the terms of Eq. 4.26 have been calculated, except for the fourth term, we can plot the diagram corresponding to a defect with several charge states by varying  $E_{Fermi}$  within a range determined by the band gap,

$$0 \leq E_{Fermi} \leq E_g. \quad (4.28)$$

Note that now the master equation is reduced to only two terms,

$$E_{form}^q = qE_{Fermi} + \xi_{form}^q, \quad (4.29)$$

where  $E_{Fermi}$  acts as a variable and  $\xi_{form}^q$  as a constant, thus assuming the characteristics of a linear function. That is why the curves are straight lines with slopes  $q$ . The diagrams, such as Fig. 4.1, helps us observe which defect charge states are thermodynamically stable. Low formation energies suggest that a defect may be energetically favorable, while charge states, with changing slopes, indicate the Fermi level ranges where a defect acquires a specific charge.

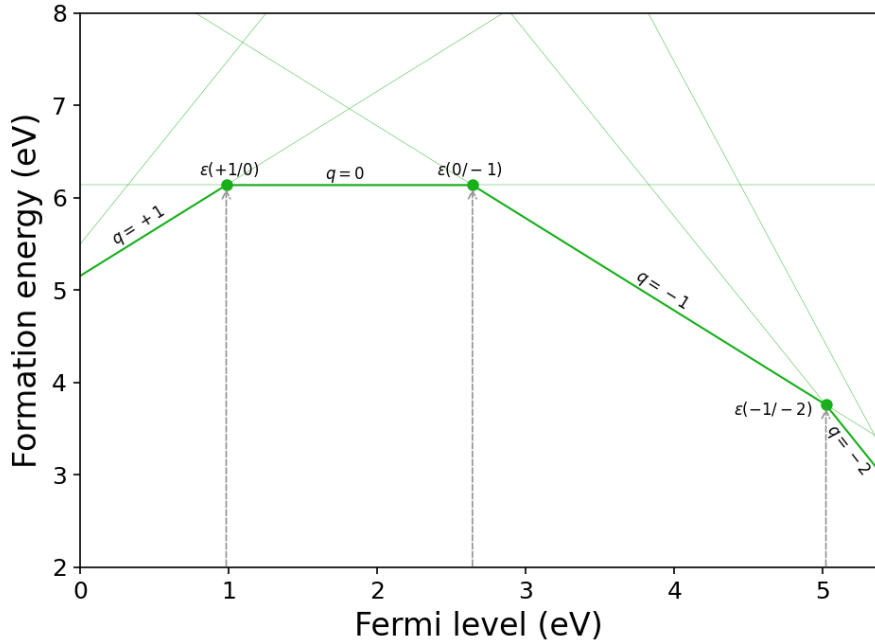


Figure 4.1: Formation energy diagram, where the slopes are determined by  $q$  and the intersections are known as transition levels  $\varepsilon(q_1, q_2)$ .

The intersection points observed in [Fig. 4.1](#) are known as thermodynamic transition levels, which show at which Fermi level two charge states have the same formation energy. This can be computed by:

$$\varepsilon(q_1, q_2) = \frac{\xi_{form}^{q_1} - \xi_{form}^{q_2}}{q_2 - q_1}. \quad (4.30)$$

## 4.7 Optical transitions

The study of optical transitions is an important physical phenomenon, since it allows us to determine whether a defect is optically active. A very useful tool to visualize the process of these transitions is through the well-known configuration coordinate (CC) diagrams. This representation is based on the Franck-Condon principle, which assumes that electronic transitions occur so rapidly that atomic configurations vary insignificantly. Furthermore, the potential energy surfaces (PES) of the ground and excited states are represented as parabolas through the harmonic oscillator approximation. Here, we must remember that the PES relates the change in the total energy of a system as a function of atomic displacements. This is shown in [Fig. 4.2](#), where the absorption energy ( $E_{abs}$ ) represents the energy required to excite a system from its ground state to an excited state and the emission energy ( $E_{emi}$ ) is the energy emitted during the reverse process. On the other hand, the energies associated with relaxations are known as Stokes ( $E_S$ ) and anti-Stokes ( $E_{AS}$ ) shifts [53], whereas  $\Delta Q$  is the displacement between the excited

and ground state and is given as:

$$\Delta Q = \sqrt{\sum_i m_i (\Delta R_i)^2}, \quad (4.31)$$

where  $m_i$  is the atomic mass and  $\Delta R_i$  is the displacement vector of atom  $i$  between the excited and ground state.

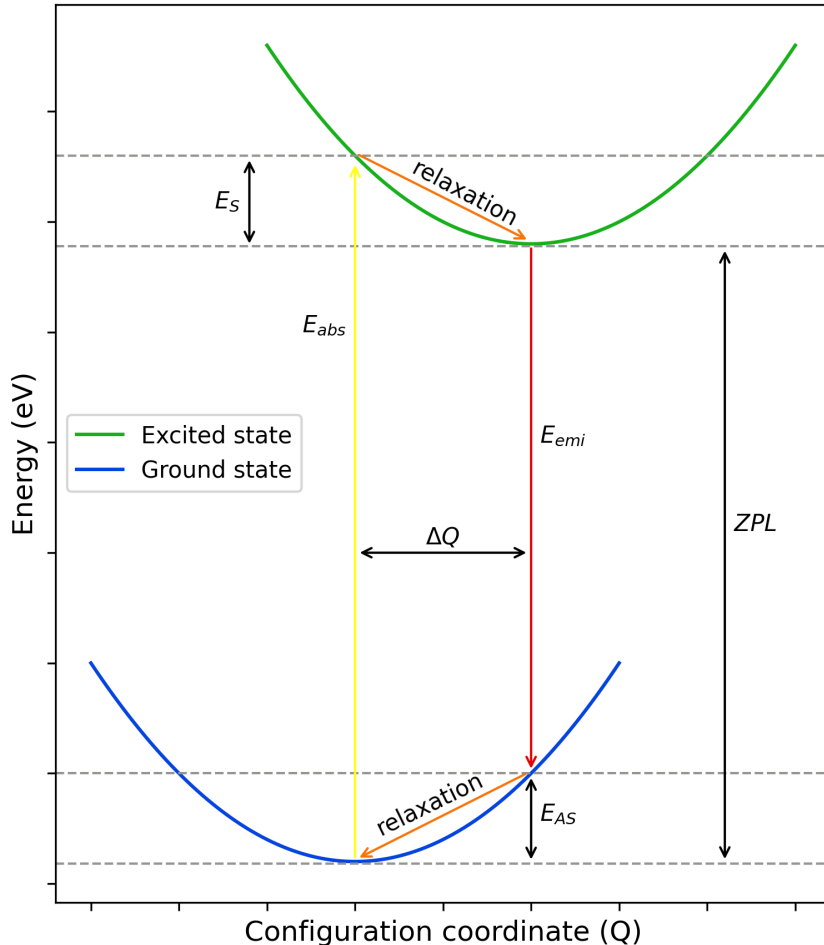


Figure 4.2: Representation of a CC diagram for the ground and excited states of the defect.

Finally, the most important factor for quantum technologies is known as the zero phonon line (ZPL), which represents the transition without the participation of phonons between the lowest PES of the ground and excited states. Therefore, ZPL is given by:

$$ZPL = E_{es}(R_{es}) - E_{gs}(R_{gs}), \quad (4.32)$$

where  $E_{es}$  and  $E_{gs}$  are the total energies of the excited and ground states, and  $R_{es}$  and  $R_{gs}$  are the geometries corresponding to these states. In addition, the wavelength ( $\lambda$ ) associated to this ZPL is given by:

$$\lambda = \frac{hc}{ZPL}, \quad (4.33)$$

where the  $hc$  factor, composed of Planck's constant and speed of light, is approximately 1241 eV.nm.

## 4.8 Spin coherence

For quantum technologies, the point defect is desired to have a non-zero spin, since the amount of light emitted by the defect depends on it. This is very important, since it enables an optical cycle between the ground and excited states of the defect, thus allowing the optical readout and state initialization. This allows us to obtain a spin-based qubit. However, the qubit's lifetime is also crucial. Therefore, since the qubit fundamentally depends on spin, its behavior under various interactions must also be understood.

The defect spin, being in a crystalline environment, is primarily affected by its interactions with nuclear spins and impurity spins. The nuclear spins are associated to the atomic nuclei, while impurity spins are related to the electron spins of others defects in the crystal. In addition, it is desirable (though not strictly required) for the elements constituting the host material to be spinless. Unfortunately, this is not always the case; however, in some cases, it can be solved through isotope engineering [33], [34].

Therefore, the problem is mainly reduced to the study of the defect spin and its interaction with the nuclear spins. Fortunately, PyCCE package implements the study of this phenomenon using the Cluster Correlation Expansion (CCE) method [19]. Here, the dynamics of a central spin and its interaction with a spin bath are studied. Note that the central spin refers to the defect spin and the spin bath is composed of the nuclear spins. The method starts from the construction of a Hamiltonian, given as follows:

$$\hat{H} = \hat{H}_S + \hat{H}_{SB} + \hat{H}_B, \quad (4.34)$$

where  $\hat{H}_S$  is the Hamiltonian of the free central spin,  $\hat{H}_{SB}$  is Hamiltonian for the interactions between central spin and spin bath and  $\hat{H}_B$  is the Hamiltonian for the interaction between spins belonging to the spin bath. However, when each term of the Hamiltonian in Eq. 4.34 is split, the different contributions that must be taken into account can be observed:

$$\hat{H} = \underbrace{\mathbf{SDS}}_{(I)} + \underbrace{\mathbf{B}\gamma_S\mathbf{S}}_{(II)} + \underbrace{\sum_i \mathbf{SA}_i\mathbf{I}_i}_{(III)} + \underbrace{\sum_i \mathbf{I}_i\mathbf{P}_i\mathbf{I}_i}_{(IV)} + \underbrace{\mathbf{B}\gamma_i\mathbf{I}_i}_{(V)} + \underbrace{\sum_{i>j} \mathbf{I}_i\mathbf{J}_{ij}\mathbf{I}_j}_{(VI)}. \quad (4.35)$$

Terms I and II belong to the Hamiltonian  $\hat{H}_S$ . They describes the dynamics of the central spin via the electron-electron spin interactions tensor  $\mathbf{D}$ , known as Zero Field Splitting (ZFS) term; and its interaction with an external magnetic field ( $\mathbf{B}$ ) via the tensor  $\gamma_S$ , known as Zeeman tensor term. In addition, the term III belongs to  $\hat{H}_{SB}$ . This term describes the interactions between the central spin and the spin bath via the tensor  $\mathbf{A}_i$ , this term is known as Hyperfine interaction term. Finally, the terms IV, V and VI belong to  $\hat{H}_B$ , they describe all the interaction between

the spins of bath and a  $\mathbf{B}$ .  $\mathbf{P}_i$  is also a ZFS tensor, but for the nuclear spins;  $\gamma_i$  is a tensor that describes the interaction between nuclear spins and the  $\mathbf{B}$ ; and  $J_{ij}$  describe the interactions between nuclear spins. The tensor  $\mathbf{S}$  refers to the spin operators of the central spin, while  $\mathbf{I}$  are operators for the spin bath. Therefore, this hamiltonian  $\hat{H}$ , in a nutshell, contains all the interactions that influence the behavior of the central spin (spin defect).

CCE method use this previous formulation of the Hamiltonian ([Eq. 4.34](#)) and implements it into its theoretical framework as an Hamiltonian composed of two effective Hamiltonians. The rlation is give as:

$$\hat{H} = |0\rangle\langle 0| \otimes \hat{H}^{(0)} + |1\rangle\langle 1| \otimes \hat{H}^{(1)}, \quad (4.36)$$

where  $\hat{H}^{(\alpha)}$  is the effective Hamiltonian acts acting only on the bath when the qubit is in a given state  $|\alpha\rangle$ . Note that both effective Hamiltonians are conditioned by the qubit level of the central spin. Therefore, for a given state  $|\alpha\rangle$ , taking into account the [Eq. 4.34](#), the effective Hamiltonian is represented as:

$$\hat{H}^{(\alpha)} = E_\alpha + \langle \alpha | \hat{H}_{SB} | \alpha \rangle + \hat{H}_B + \hat{H}_{PT}^{(\alpha)}, \quad (4.37)$$

where  $E_\alpha$  is the expectation value of the central spin and  $\hat{H}_{PT}^{(\alpha)}$  contains high order perturbations terms. This is where the power of the CCE comes into play. Instead of directly tackling the problem by simulating the central spin interacting with the whole spin bath, CCE reduces the spin bath to small subsets of spins called clusters. These clusters are the ones that interact with the central spin. Thus, the Hamiltonian for each cluster can be represented as  $\hat{H}_C^{(\alpha)}$ . This is crucial, since it provides the chance to construct the coherence function. This function shows how coherence of the central spin decays over time, which is extremely important for our purposes. Thus, coherence function is give as:

$$L_C = \text{Tr} \left( \hat{U}_C^{(0)}(t) \hat{\rho}_C \hat{U}_C^{(1)\dagger}(t) \right), \quad (4.38)$$

where  $\hat{U}_C^{(\alpha)}(t)$  is the time propagator and  $\hat{\rho}_C$  is the reduced density matrix of the cluster interacting with the central spin. The CCE method is focused on pure dephasing of the central spin, so matrix density is also crucial. This is because the decay of the off-diagonal element of the density matrix captures the decoherence of the central spin [\[54\]](#). On the other hand, time propagators provide the possibility of manipulating the state of the central spin through pulses, which alters the interaction between the central spin and the spin bath. This change the evolution of the bath and can extend the lifetime of the state of the central spin. An used method fo this propose is the Han-echo sequence, which applied a  $\pi$ -pulse on the qubit. Here, the time propagators can be defined as:

$$\hat{U}_C^{(0)} = \exp \left( -\frac{i}{\hbar} \hat{H}_C^{(1)} \frac{t}{2} \right) \exp \left( -\frac{i}{\hbar} \hat{H}_C^{(0)} \frac{t}{2} \right), \quad (4.39)$$

$$\hat{U}_C^{(1)} = \exp \left( -\frac{i}{\hbar} \hat{H}_C^{(1)} \frac{t}{2} \right) \exp \left( -\frac{i}{\hbar} \hat{H}_C^{(0)} \frac{t}{2} \right). \quad (4.40)$$

Now that coherence has been obtained through the interaction between the central spin and the clusters, the global coherence must be constructed. This can be expressed as a factorized function due to the correlated contributions from the clusters,

$$\mathcal{L}(t) = \prod_C \tilde{L}_C(t). \quad (4.41)$$

Here, each cluster contribution is obtained recursively. Thus,  $\tilde{L}_C(t)$  is given as:

$$\tilde{L}_C = \frac{L_C}{\prod_{C'} \tilde{L}_{C' \subset C}}. \quad (4.42)$$

Finally, it should be noted that the cluster size defines the approximation order in the CCE method.

## 4.9 Selection of point defects in a host material

Once the semiconductor host material has been determined, a screening process must be carried out to determine the most promising defects based on the **A**, **B** and **D** requirements outlined in [Section 2.5.3](#). [Fig. 4.3](#) shows the workflow for this screening process. The starting point, as we already know, is our host material: c-BN, in which several defects will be created. This group of defects generates a small database, around 20 defects, which includes native, impurity, and complex defects (see [Table 2.2](#)). Remember that native defects involve only atoms that make up the host material, impurity-based defects involve atoms that are not present in the host material, and complex defects can be created from the combination of the above defects. Once the database is collected, the first calculations can be carried out using the PBE method, which employs the PBE functional. At this point, an analysis of thermodynamic stability, the arrangement of Kohn-Sham energy levels within the band gap, localized states, and spin state will determine whether the defect is a potential QT candidate. If the defect does not meet the required characteristics, it is discarded from further investigations. Otherwise, if the defect meets the required characteristics, additional more detailed calculations will be performed, but this time using the HSE06 method, which employs the HSE06 functional. Finally, the results are analyzed once again based on the previous requirements. If these final defects satisfy the requirements, they are selected for further calculations such as ZPL and spin coherence.

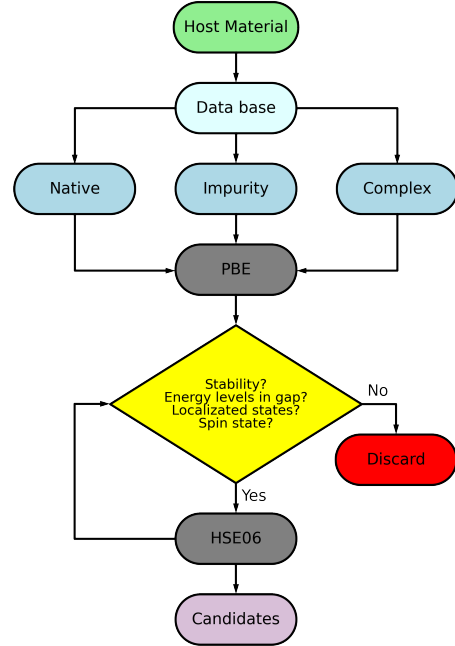


Figure 4.3: Workflow for obtaining potential point defects in c-BN.

# Chapter 5

## Computational Aspects

This section will report parameters such as the energy cutoff and  $\mathbf{k}$ -density for c-BN and stables phases. Both must be defined through convergence tests before performing the main calculations. In addition, the convergence test for supercell size will also be included. As explained in [Section 4.3](#), this is good practice to balance accuracy and computational cost. The results presented here and in the next chapter were calculated using the Vienna Ab initio Simulation Package (VASP) [11]–[14], along with effective pseudopotentials and the Projector augmented wave (PAW) method [15], [16], and were implemented on the Saga supercomputer provided by the Norwegian research infrastructure services (NRIS). Parameters such as energy convergence criterion for electronic self-consistency and criterion for the ionic optimization are set to  $1 \times 10^{-6}$  and 0.03, respectively. The first criterion reaches convergence when the difference between successive total energies is less than the specified value, while the second achieves it when the magnitude of the force on atoms is also less than the specified value. Both must be defined in the INCAR file as EDIFF and EDIFFG tags.

### 5.1 Convergence tests: Primitive cell

As mentioned earlier, the first parameter to converge is the energy cutoff. This latter can be defined in the INCAR file as ENCUT tag. Here, we have used three different configurations for testing: one is the pristine cell (reference cell), and the others are obtained by modifying the lattice constant of the pristine cell. Therefore, the three cells will be distinguished by their volumes. The modified cells will be known as increased-volume cells and decreased-volume cells, where their lattice constants are altered by  $\Delta a = \pm 0.02$  with respect to the pristine cell.

The pristine cell used is the primitive cell of the c-BN, which has a lattice constant  $a = 2.56 \text{ \AA}$ . The convergence tests carried out for this first case show that a energy cutoff of 500 eV is optimal. [Fig. 5.1a](#) gives us a visual perspective of the behavior of the curves, while [Table 5.1](#) shows us the details of the calculations, where each term is defined as follows:  $E_{\text{prist}}$  is the total energy of the pristine cell,  $E_{\text{dec}}$  is the total energy of the decreased-volume cell,  $E_{\text{inc}}$  is the total energy of the increased-volume cell and the relative energies  $E_{\{\text{dec},\text{inc}\}}^{\text{rel}}$  are the difference of the

total energies between the modified cells and pristine cell, given as:

$$E_{\{dec,inc\}}^{rel} = |E_{\{dec,inc\}} - E_{prist}|. \quad (5.1)$$

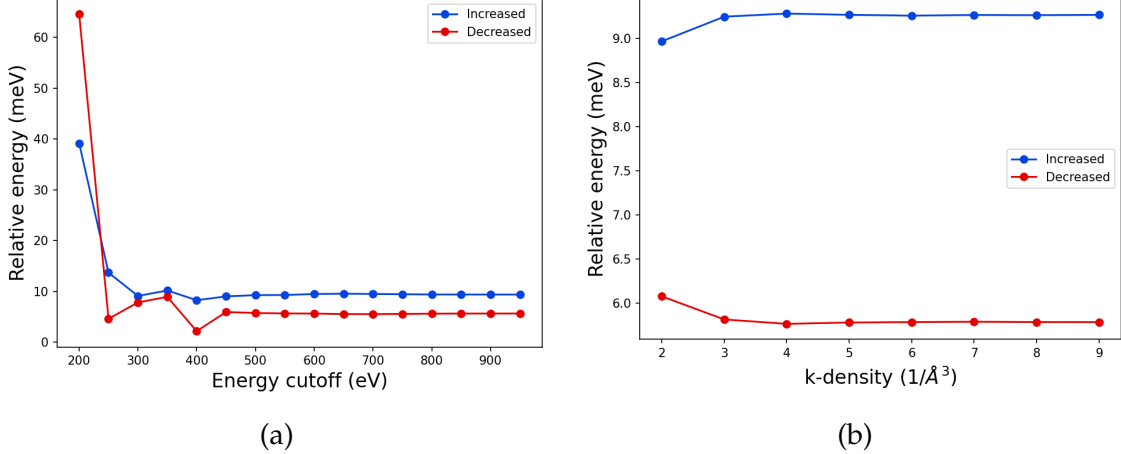


Figure 5.1: (a) Energy cutoff and (b)  $\mathbf{k}$ -density convergence for primitive cell using three configurations: pristine, increased-volume and decreased-volume cells. Relative energies are the difference of the total energies between the modified cells and pristine cell.

Table 5.1: Detailed information on the total energies and relative energies for each energy cutoff. An energy cutoff of 500 eV was chosen for c-BN under a convergence criterion of 1 meV (gray shaded area). A complete version of the table can be found in **Table A.1**.

ENCUT (eV)	$E_{prist}$ (eV)	$E_{dec}$ (eV)	$E_{inc}$ (eV)	$E_{dec}^{rel}$ (meV)	$E_{inc}^{rel}$ (meV)
400	-17.449	-17.447	-17.441	2.190	8.284
450	-17.454	-17.448	-17.445	5.954	9.034
500	-17.451	-17.446	-17.442	5.769	9.279
550	-17.452	-17.446	-17.442	5.677	9.308
600	-17.455	-17.449	-17.445	5.652	9.500

Taking this into account, we can observe that the relative energies converge under a criterion of 1 meV for energy cutoffs equal to or greater than 500 eV.

Now that we have chosen an energy cutoff, we can continue with the  $\mathbf{k}$ -density convergence. Unlike the first case, where the tag is defined in the INCAR

file, here we must define the  $\mathbf{k}$ -point mesh in the KPOINTS file. Following the same analysis above, we can note in **Table 5.2** that all relative energies converge under a criterion of 1 meV. Thus, a  $\mathbf{k}$ -density of 4 was chosen. **Fig. 5.1b** gives us a visual perspective of the behavior of the curves.

Table 5.2: Detailed information on the  $\mathbf{k}$ -density convergence for c-BN. A  $\mathbf{k}$ -density of 4 was chosen under a convergence criterion of 1 meV (gray shaded area). A complete version of the table can be found in **Table A.2**.

$\mathbf{k}$ -density ( $1/\text{\AA}^3$ )	$E_{prist}$ (eV)	$E_{dec}$ (eV)	$E_{inc}$ (eV)	$E_{dec}^{rel}$ (meV)	$E_{inc}^{rel}$ (meV)
2	-17.435	-17.429	-17.426	6.080	8.964
3	-17.451	-17.445	-17.442	5.818	9.243
4	-17.451	-17.446	-17.442	5.769	9.279
5	-17.451	-17.446	-17.442	5.784	9.264
6	-17.451	-17.446	-17.442	5.789	9.255

## 5.2 Convergence test: Stable Phases

The procedure for analyzing the convergence tests for the stable phases of the species that make up the c-BN is identical to that performed for the primitive cell. The motivation for these tests is that chemical potentials are required to calculate the formation energies of the defects and subsequently plot the diagrams.

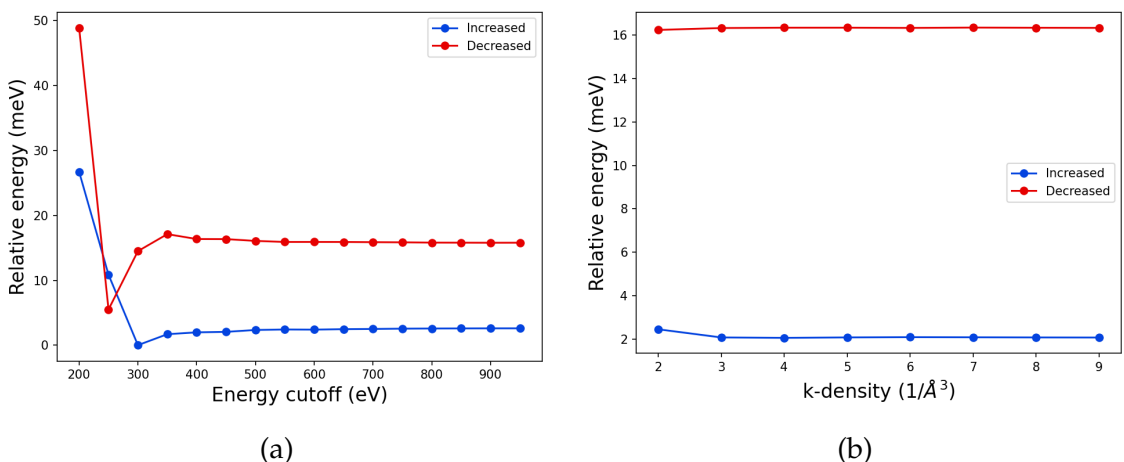


Figure 5.2: (a) Energy cutoff and (b)  $\mathbf{k}$ -density convergence for rhombohedral  $\alpha$ -boron using three configurations: pristine, increased-volume and decreased-volume cells. Relative energies are the difference of the total energies between the modified cells and pristine cell.

For boron, its  $\alpha$ -Rhombohedral phase has been used with a lattice constant  $a = 5.04 \text{ \AA}$ . Similarly to c-BN, modified cells have also been created here by the same variation  $\Delta a = \pm 0.02$ . The results of the energy cutoff convergence are shown in **Table 5.3**, where we can note that the relative energies converge under a criterion of 1 meV for energies cutoff equal to or greater than 450 eV. **Fig. 5.2a** shows the curves for these cases.

Table 5.3: Detailed information on the energy cutoff convergence for rhombohedral  $\alpha$ -boron. An energy cutoff of 450 eV was chosen under a convergence criterion of 1 meV (gray shaded area). A complete version of the table can be found in **Table A.4**.

ENCUT (eV)	$E_{prist}$ (eV)	$E_{dec}$ (eV)	$E_{inc}$ (eV)	$E_{dec}^{rel}$ (meV)	$E_{inc}^{rel}$ (meV)
350	-80.419	-80.402	-80.417	17.112	1.691
400	-80.437	-80.421	-80.435	16.360	1.977
450	-80.436	-80.420	-80.434	16.347	2.052
500	-80.440	-80.424	-80.438	16.069	2.342
550	-80.446	-80.430	-80.444	15.909	2.419

Regarding  $\mathbf{k}$ -density convergence, the results are shown in **Table 5.4** and plotted in **Fig. 5.2b**. Here, once again, all relative energies converge under a criterion of 1 meV, so the  $\mathbf{k}$ -density was chosen as 4.

Table 5.4: Detailed information on the  $\mathbf{k}$ -density convergence for rhombohedral  $\alpha$ -boron. A  $\mathbf{k}$ -density of 4 was chosen under a convergence criterion of 1 meV (gray shaded area). A complete version of the table can be found in **Table A.3**.

$\mathbf{k}$ -density ( $1/\text{\AA}^3$ )	$E_{prist}$ (eV)	$E_{dec}$ (eV)	$E_{inc}$ (eV)	$E_{dec}^{rel}$ (meV)	$E_{inc}^{rel}$ (meV)
2	-80.492	-80.476	-80.490	16.244	2.446
3	-80.428	-80.411	-80.426	16.331	2.071
4	-80.434	-80.420	-80.435	16.347	2.052
5	-80.438	-80.421	-80.436	16.347	2.072
6	-80.438	-80.421	-80.436	16.337	2.083

On the other hand, nitrogen is a gas, so we only need to perform the energy

cutoff convergence. This is because for gases only one k-point is required (at  $\Gamma$ ). However, we will use the same methodology as in the previous cases to confirm this. Here, a nitrogen dimer has been used in a cell with a lattice constant  $a = 10 \text{ \AA}$ . Energy cutoff convergence is plotted in **Fig. 5.3a**, while its detailed information is presented in **Table 5.5**. The energy cutoff found for this case is 500 eV under a criterion of 1 meV, and the initial assumption about the k-density convergence is confirmed through **Fig. 5.3b** and **Table 5.6**.

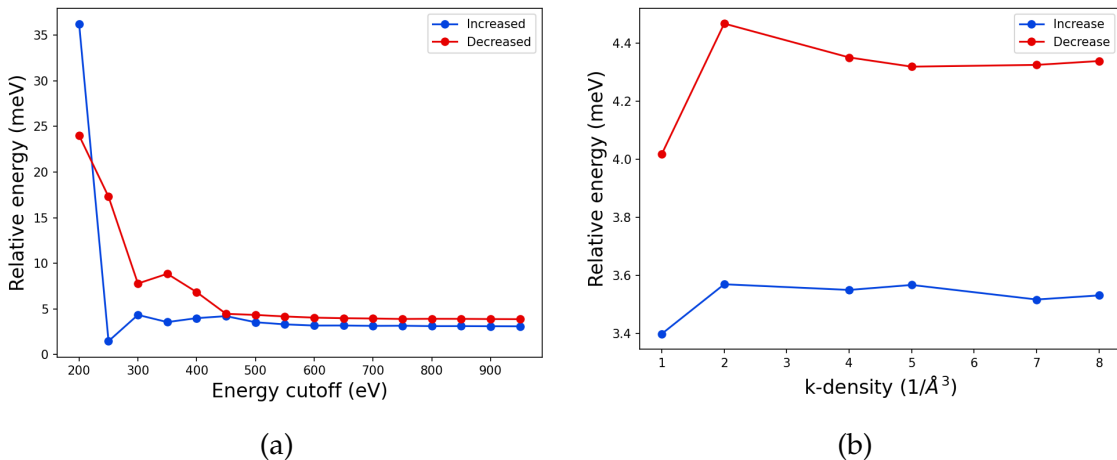


Figure 5.3: (a) Energy cutoff and (b) k-density convergence for nitrogen gas in a cell with a lattice constant  $a = 10 \text{ \AA}$ , using three configurations: pristine, increased-volume and decreased-volume cells. Relative energies are the difference of the total energies between the modified cells and pristine cell.

Table 5.5: Detailed information on the energy cutoff convergence for nitrogen gas. An energy cutoff of 500 eV was chosen under a convergence criterion of 1 meV (gray shaded area). A complete version of the table can be found in **Table A.5**

ENCUT (eV)	$E_{prist}$ (eV)	$E_{dec}$ (eV)	$E_{inc}$ (eV)	$E_{dec}^{rel}$ (meV)	$E_{inc}^{rel}$ (meV)
400	-16.591	-16.584	-16.595	6.846	3.997
450	-16.615	-16.610	-16.619	4.469	4.218
500	-16.623	-16.619	-16.627	4.352	3.549
550	-16.629	-16.624	-16.632	4.182	3.316
600	-16.633	-16.629	-16.636	4.053	3.187

Table 5.6: Detailed information on the  $\mathbf{k}$ -density convergence for nitrogen gas. The data confirm that the  $\Gamma$  point is sufficient (gray shaded area). An extended version of the table can be found in **Table A.6**.

$\mathbf{k}$ -density ( $1/\text{\AA}^3$ )	$E_{prist}$ (eV)	$E_{dec}$ (eV)	$E_{inc}$ (eV)	$E_{dec}^{rel}$ (meV)	$E_{inc}^{rel}$ (meV)
1	-16.623	-16.619	-16.627	4.018	3.398
2	-16.623	-16.619	-16.627	4.468	3.569
4	-16.623	-16.619	-16.627	4.352	3.549

### 5.3 Convergence test: Supercell

For this test, native defects such as boron and nitrogen vacancies will be used. Each defect will be introduced into supercells of different sizes. Therefore, formation energies will be calculated using a reduced form of **Eq. 4.26**, given as:

$$E_{form}^{q=0}[V_i] = E_{def}^{q=0}[V_i] - E_{perf} + \mu_i^{elemental} \quad (5.2)$$

where defects are also considered in their neutral states, that is,  $q = 0$ . Since the parameters for the stable phases were defined with convergence tests, the elemental chemical potentials for each case can be calculated from the bulk's relaxation as follows:

$$\mu_i^{elemental} = \frac{E_{tot}[i]}{N} \quad (5.3)$$

where  $E_{tot}[i]$  is the total energy and  $N$  the number of atoms. For both cases their values are defined as:  $\mu_B^{elemental} = -6.703$  eV and  $\mu_N^{elemental} = -8.317$  eV.

Table 5.7: Convergence test of supercell size for c-BN. Supercells were generated by replicating the conventional cell in a range from  $2 \times 2 \times 2$  to  $6 \times 6 \times 6$ .

N	$E_{prist}$ (eV)	$E_{def}[V_B]$ (eV)	$E_{def}[V_N]$ (eV)	$E_{form}[V_B]$ (eV)	$E_{form}[V_N]$ (eV)
64	-558.450	-542.435	-542.054	9.311	8.071
216	-1884.780	-1868.495	-1868.242	9.581	8.212
512	-4467.653	-4451.32	-4451.095	9.628	8.232
1000	-8725.994	-8709.647	-8709.423	9.643	8.245
1728	-15078.619	-15062.268	-15062.042	9.647	8.251

**Table 5.7** shows that for a supercell with 216 atoms, the formation energy at both defects converges within a criterion of 50 meV. In addition, **Fig. 5.4** shows the curves for both cases.

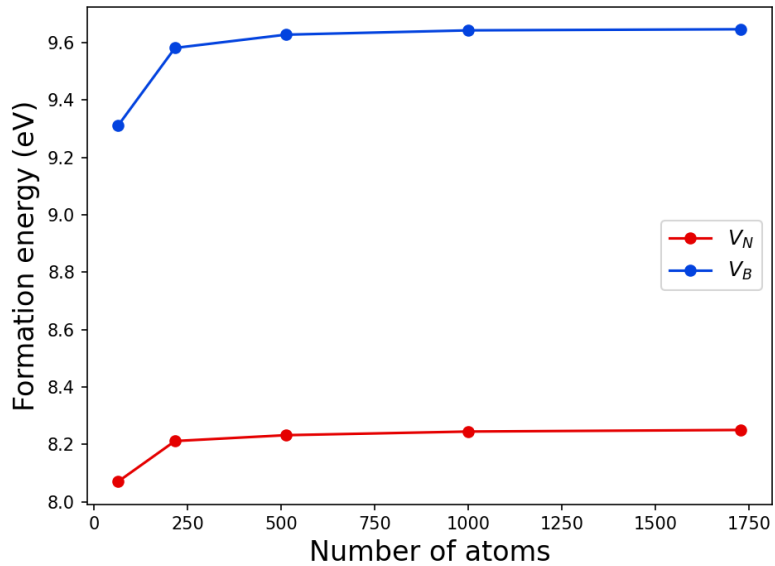


Figure 5.4: Convergence test for supercell size. The number of atoms in the supercell is analyzed with respect to the formation energy.

# Chapter 6

## Results

In this chapter, we will dive into the findings related to bulk properties of the host materials, as well as the formation energy diagrams, Kohn-Sham level diagrams, zero phonon line and spin coherence associated with point defects. Our starting point will be the study of the most notable host semiconductor material for point defects: diamond, which was taken as a benchmark for our main investigation. Then, the findings of our exploration of bulk properties and point defects for c-BN will be developed. As mentioned in [Chapter 5](#), the calculations were performed using VASP with two different functionals: PBE and HSE06. Here, the HSE06 functional was used with its default parameters:  $\alpha = 0.25$  and  $\omega = 0.2$ .

### 6.1 Studies of NV center in diamond

The studies in this section will focus on the NV center in diamond:  $\text{NV}^0$  and  $\text{NV}^{-1}$ . Details on bulk properties, dielectric tensor, formation energies, energy levels, highly localized states, and the zero-phonon line are studied through analysis of the lattice constant, band gap, band structure diagram, formation energy diagram, Kohn-Sham level diagrams, Inverse Participation Ratio, and the Delta Self-Consistent Field ( $\Delta\text{SCF}$ ) method.

#### 6.1.1 Bulk properties of diamond

The calculations for the unit cell of diamond were carried out using an energy cutoff of 500 eV and a  $\mathbf{k}$ -density of 4. The results for the lattice constant and band gap using the PBE and HSE06 methods are shown in [Table 6.1](#). We can note that, regarding lattice constant,  $a^{\text{PBE}} = 3.574$  and  $a^{\text{HSE06}} = 3.548$  Å. Here, the PBE method overestimates the value, while the HSE06 method underestimates it compared to the experimental value of  $a^{\text{exp}} = 3.567$  Å. Since ab initio simulations are performed at 0 K, the HSE06 method is in agreement with the experimental data [55]. On the other hand, both the PBE and HSE06 functionals underestimate the band gap values, where  $E_g^{\text{PBE}} = 4.157$  and  $E_g^{\text{HSE06}} = 5.369$  eV, compared to the experimental band gap measured at  $E_g^{\text{exp}} = 5.470$  eV [56]. However, the HSE06 method, as expected, is in much better agreement as compared to PBE, with a difference between theory and experiment of approximately 0.1 eV.

Table 6.1: Report of lattice constant and band gap obtained from DFT calculations using the PBE and HSE06 functionals for diamond. Both experimental values are reported at room temperature, while simulations are at 0 K.

Method	Lattice constant (Å)	Band gap (eV)
PBE	3.574	4.157
HSE06	3.548	5.369
Experimental	3.567 [55]	5.470 [56]

**Fig. 6.1** shows the band structure diagram computed for bulk diamond using the PBE (red lines) and HSE06 (blue lines) functional. Here, we can see that diamond exhibits an indirect gap. Note that the top of the valence band, called the valence band maximum (VBM), is located at  $\Gamma$ -point, while the bottom of the conduction band, called the conduction band minimum (CBM), is located near the X-point.

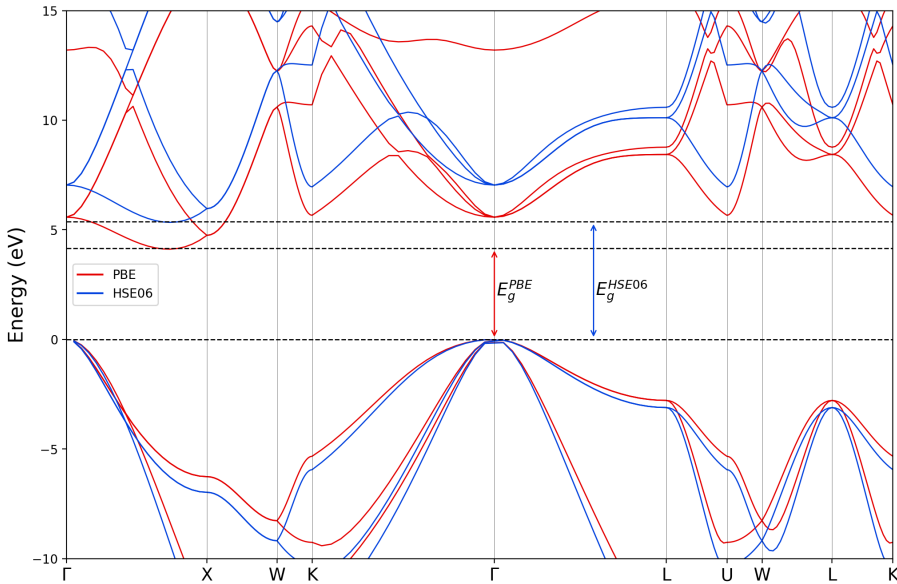


Figure 6.1: Band structure diagram computed for bulk diamond using the PBE (red) and HSE06 (blue) functionals. Both methods reveal an indirect band gap in diamond. However, the PBE method yields a band gap of 4.157 eV, while HSE06 calculations yield a band gap value of 5.369 eV when the fraction of exact Hartree-Fock exchange is set to 0.25. Here, HSE06 functional reports a much better agreement with the experimental value of 5.470 eV at 295 K [56].

Another bulk property associated with the host material is the dielectric tensor, which helps us understand the behavior of the material in the presence of an electric field. In the study of defects, spurious Coulomb-type interactions are usually introduced due to the defect-defect interaction and their associated charges. Since these long-range interactions are screened by the dielectric response of the material, it is important to take this response into account for a correct prediction of the phenomena. As we mentioned in **Section 4.5**, the dielectric tensor is needed to compute the finite size correction for charged defects, where  $\epsilon$  is replaced in **Eq. 4.24** depending on whether the material is isotropic or anisotropic. The dielectric tensor ( $\epsilon$ ) can be split as:

$$\epsilon = \epsilon_{ij}^0 + \epsilon_{ij}^\infty, \quad (6.1)$$

where  $\epsilon_{ij}^0$  is the ionic contribution and  $\epsilon_{ij}^\infty$  is the electronic contribution. After performing calculations using the PBE functional, it was found that the contributions are given by:

$$\epsilon_{ij}^0 = \begin{bmatrix} 0 & 0 & 0 \\ 0 & 0 & 0 \\ 0 & 0 & 0 \end{bmatrix}, \quad \epsilon_{ij}^\infty = \begin{bmatrix} 5.857 & 0 & 0 \\ 0 & 5.857 & 0 \\ 0 & 0 & 5.857 \end{bmatrix}. \quad (6.2)$$

Note that the off-diagonal elements in both matrices are zero. This was expected since the host material (diamond) is isotropic.

### 6.1.2 Formation energy diagram for the NV center

The NV center is a well-known defect complex in diamond, composed of a substitutional defect and a vacancy. This involves the replacement of a carbon atom by a nitrogen atom ( $N_C$ ) and the removal of a neighboring carbon atom ( $V_C$ ). For calculations of the NV center in diamond, a supercell of 216 atoms was used for the calculations with an energy cutoff of 500 eV at the  $\Gamma$ -point.

**Fig. 6.2** shows the formation energy diagram for NV center in diamond, which was plotted using a charge state range from  $-2$  to  $+2$  with both PBE and HSE06 methods. Here, the curve computed using the PBE method (dashed line) is incorporated into the HSE06 method plot for illustrative purposes only. This diagram shows that the thermodynamic stability of the defect is promising for neutral (0) and singly negative ( $-1$ ) charge states ( $NV^0$  and  $NV^{-1}$ ). Both charge states coexist when the Fermi level lies around the midgap, at 1.949 eV according to the PBE method and 2.640 eV according to the HSE06 method. However,  $NV^0$  is most stable when the Fermi level is closer to the valence band, while  $NV^{-1}$  is most stable when the Fermi level is closer to the conduction band.

Detailed information on thermodynamic transition levels can be found in **Table 6.2**. The values of the Fermi level and formation energy for each thermodynamic transition level are reported using the PBE and HSE06 methods.

In addition, **Table 6.3** presents information on the charge state, total energy of the defective supercell and energy corrections, which satisfy Eq. 4.26, using the HSE06 method. The  $\zeta_{form}^q$  values correspond to the second term in Eq. 4.29. The information for all the above terms using the PBE method is shown in **Table D.1**.

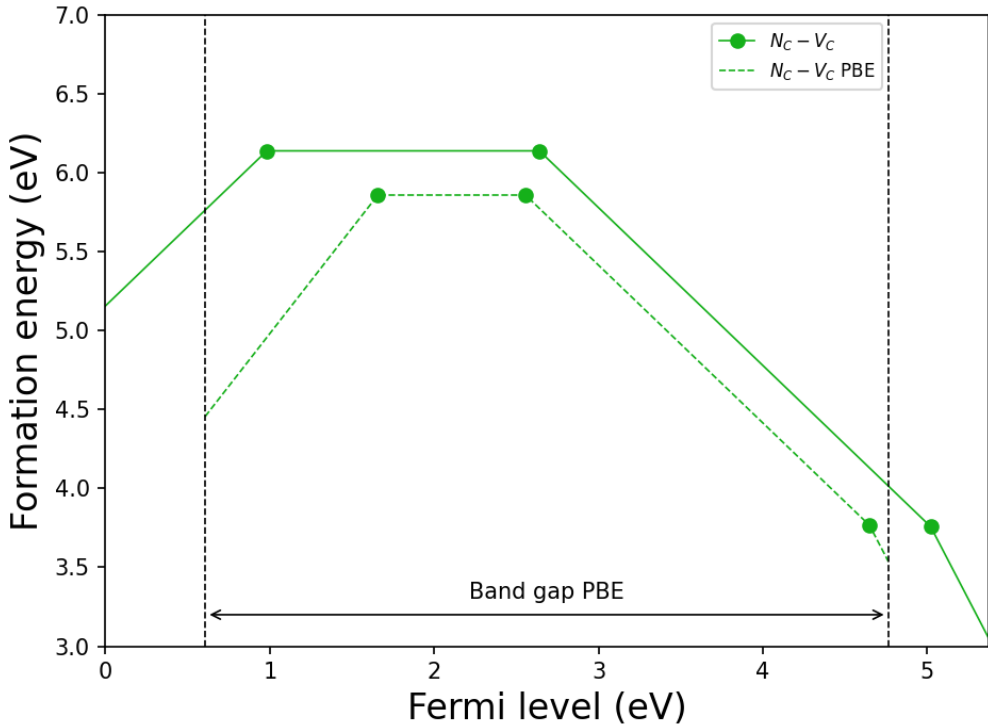


Figure 6.2: Formation energy diagram for NV center in diamond. Calculations were performed using PBE and HSE06 methods. The band gap obtained with PBE method is 4.157 eV, while with HSE06 method is 5.369 eV. The solid line represents the HSE06 method, while the dashed line corresponds to the PBE method. The curve computed using the PBE method is centered into the plot for illustrative purposes.

Table 6.2: Details of the thermodynamic transition levels with respect to the Fermi level and the defect formation energy for NV center in diamond using both PBE and HSE06 methods.

Thermodynamic transition levels	Fermi level (eV)		Formation energy (eV)	
	PBE	HSE06	PBE	HSE06
$\varepsilon(+1, 0)$	1.051	0.982	5.858	6.138
$\varepsilon(0, -1)$	1.949	2.640	5.858	6.138
$\varepsilon(-1, -2)$	4.042	5.020	3.766	3.758

Table 6.3: Values for the terms of Eqs. 4.26 and 4.29 which enable plotting of the formation energy diagram for the NV center in diamond using the HSE06 method. Here,  $E_{perf} = -2276.808$  eV and  $E_{VBM} = 9.329$  eV.

$q$	$E_{def}^q$ (eV)	$E_{corr}$ (meV)	$\xi_{form}^q$ (eV)
-2	-2234.863	1363	12.435
-1	-2248.237	388	8.390
0	-2259.818	0	6.138
+1	-2270.301	172	4.984
+2	-2279.912	800	4.701

### 6.1.3 Kohn-Sham level diagrams

The Kohn-Sham level diagrams depict the arrangement of single-particle Kohn-Sham levels for a given configuration. Their importance lies in approximate the energy levels created by defects within the band gap of a host material. Therefore, the Kohn-Sham level diagrams for  $NV^0$  and  $NV^{-1}$ , computed using the HSE06 method, are shown in Fig. 6.3. After the relaxation of the supercell, both defects reduce the  $O_h$  symmetry of diamond to  $C_{3v}$  symmetry. The diagram for  $NV^0$  in Fig. 6.3a has an arrangement of only non-degenerate levels within the band gap, where three of them are occupied and lie near the VBM. Moreover, the system exhibits a total spin state of  $S = 1/2$  (doublet). On the other hand, the diagram for  $NV^{-1}$  in Fig. 6.3b shows both non-degenerate and degenerate levels in both spin channels, where four of the electronic states are occupied. Here, the spin state associated with the ground state is  $S = 1$  (triplet). The channel of most interest in this case is the spin down channel, where the arrangement of levels within the band gap consists of an occupied non-degenerate level and a non-occupied degenerate level separated by approximately 2.95 eV in the Kohn-Shame picture. Table 6.4 lists the respective energies for each level within the band gap for the  $NV^{-1}$  defect using the HSE06 method. In addition, the band indices are included as well. Information for the  $NV^0$  defect can be found in Table D.2 in Appendix D.

An important feature that these defect-induced energy levels within the band gap must exhibit, in the context of applications in quantum technologies, is a high degree of localization. A useful way to quantify this localization is through the Inverse Participation Ratio (IPR) or the Projected Density of States (PDOS) onto  $s$ ,  $p$ , and  $d$  orbitals. In this thesis, localization will be analyzed using the IPR, which implies consideration of the wave function. In this context, IPR is given by

$$IPR = \frac{\sum_i |\psi_i|^4}{\left(\sum_i |\psi_i|^2\right)^2}, \quad (6.3)$$

where  $\psi_i$  is the wave function associated with the  $i$ -th Kohn-Sham state or band, while the denominator ensures the normalization of the wave function. Thus, Eq. 6.3 quantifies how localized or spread out a Kohn-Sham state is.

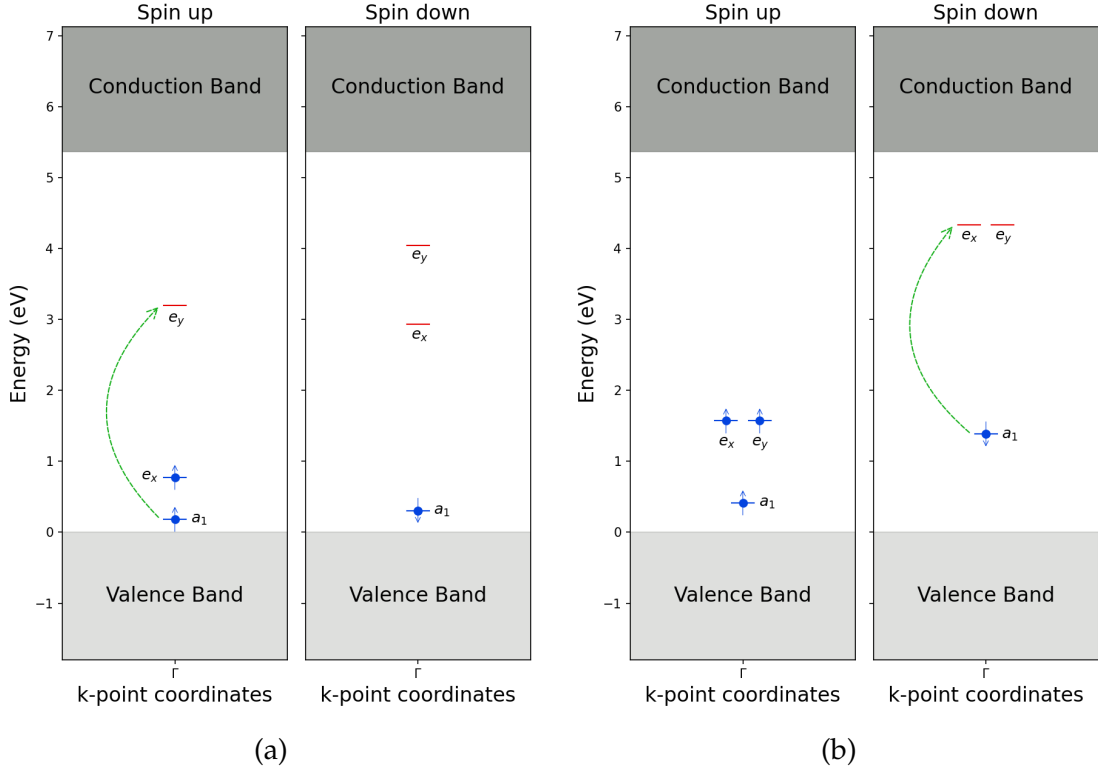


Figure 6.3: Kohn-Sham level diagrams of the (a)  $NV^0$  and (b)  $NV^{-1}$  defects in diamond calculated using the HSE06 functional. The occupied levels are depicted with a blue ball and either an upward or downward arrow, while the unoccupied levels are depicted by red solid lines. The green dashed curved arrow represents the promotion of an electron from an occupied level to an unoccupied level.

Table 6.4: Energies for each Kohn-Sham level within the band gap for the  $NV^{-1}$  defect in diamond calculated using HSE06 method. The table includes information for both spin channels and their respective band indexes. An asterisk indicates whether the level is occupied.

States	Band index	Energy (eV)	
		Spin up	Spin down
$a_1$	430	0.418 (*)	1.383 (*)
$e_x$	431	1.572 (*)	4.337
$e_y$	432	1.572 (*)	4.337

**Fig. 6.4** shows the localization (IPR) of all Kohn-Sham states within the band gap for the  $\text{NV}^{-1}$  defect as calculated using the HSE06 functional. Note that occupied electronic states that are degenerate are more localized (exhibit higher IPR) than the unoccupied states associated with non-degenerate levels in both spin channels. In addition, some unoccupied states (6) within the band gap can be observed in the lower right corner of both figures. These have not been taken into account, as they are delocalized. Information for the  $\text{NV}^0$  defect can be found in **Fig. D.1** in **Appendix D**.

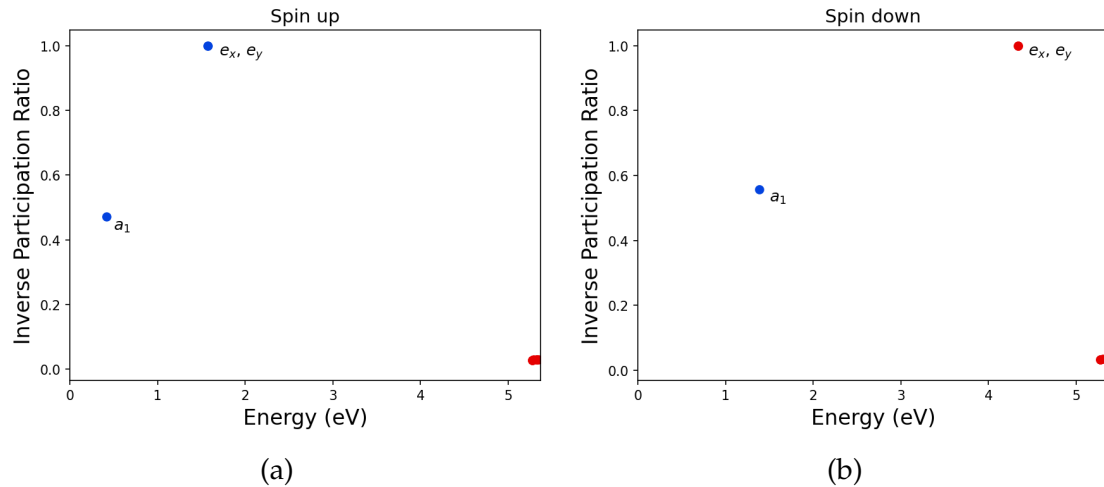


Figure 6.4: IPR for the  $\text{NV}^{-1}$  defect in diamond calculated using the HSE06 method for (a) the spin up channel and (b) the spin down channel. The occupied electronic states are represented by blue balls, while the unoccupied states are represented by red balls. The energy range goes from 0 to  $E_g = 5.369$  eV.

### 6.1.4 Zero Phonon Line

The Zero Phonon Line (ZPL) is an important quantity to determine whether a defect is optically active. The methodology for its calculation requires the total energies of the ground and excited states of the defect, without altering the charge state (internal excitation). This transition occurs without the emission or absorption of phonons.

The ground state of a given system is reached after its relaxation. However, to reach the excited state, which must also be relaxed, electrons must be promoted from the Highest Occupied Molecular Orbital (HOMO) to the Lowest Unoccupied Molecular Orbital (LUMO) according to the arrangement of levels in the Kohn-Sham level diagram of the ground state. The VASP software allows this process through the Delta Self-Consistent Field ( $\Delta\text{SCF}$ ) method, where electron promotion is configured in the INCAR file using the FERWE and FERDO tags.

The ZPL for the  $\text{NV}^0$  defect is described without numerical or convergence problems when an electron is promoted from the non-degenerate  $a_1$  level to another non-degenerate  $e_y$  level in the spin up channel (see **Fig. 6.3a**) using the HSE06 method [57]. Here, the configurations for both the ground and excited

states are given by  $^2A_2$  and  $^2E$ :

$$^2A_2 : a_1^2 e^1 \longrightarrow ^2E : a_1^1 e^2. \quad (6.4)$$

However, the HSE06 method faces numerical and convergence problems when promoting an electron from an occupied level to one of the unoccupied degenerate levels, as seen in the case of the  $NV^{-1}$  defect, where the electron must be promoted from  $a_1$  to  $e_x$  in the spin down channel (see **Fig. 6.3b**). Ideally, the configurations for both the ground and excited states are given by  $^3A_2$  and  $^3E$ :

$$^3A_2 : a_1^2 e^2 \longrightarrow ^3E : a_1^1 e^3. \quad (6.5)$$

As we mentioned earlier, hybrid functionals include a fraction of the exact Hartree-Fock exchange, where its energy is calculated via **Eq. 4.5**. Note that the energy depends explicitly on the wave functions of the electrons, which makes the functional non-local, thus complicating the description of degenerate levels. Furthermore, the Jahn-Teller distortion is also involved, since there are degenerate levels. These structural distortions tend to break the crystal symmetry in an effort to reduce the total energy by eliminating the degeneracy. This also leads to problems in electron promotion. Therefore, these numerical and convergence problems can be associated with how the Hartree-Fock exchange energy is calculated in the HSE06 method and the Jahn-Teller distortion. Otherwise, when the electron is promoted to the doubly degenerate level by assigning an equal occupancy (0.5 – 0.5), symmetry is preserved and convergence is facilitated [58]. Therefore the configurations are rewritten as follows:

$$^3A_2 : a_1^2 e^2 \longrightarrow ^3E : a_1^1 e_x^{1.5} e_y^{1.5}. \quad (6.6)$$

Although this apparently alleviates the problem, it could not be a correct description, due to spurious interactions. However, ZPL values using the HSE06 method are reported following the latter methodology.

**Table 6.5** shows a report of the ZPL values calculated for  $NV^0$  and  $NV^{-1}$  defects using the PBE and HSE06 methods. Note that the ZPL value calculated using the HSE06 method for the  $NV^0$  defect is 1.638 eV, which is an underestimation by approximately 0.52 eV compared to the experimental value [59]. On the other hand, for the  $NV^{-1}$  defect, the PBE and HSE06 methods yield ZPL values of 1.71 and 2.227 eV, respectively. Here, the PBE method underestimates the ZPL value by 0.24 eV, while the HSE06 method overestimates it by 0.28 eV compared to the experimental value [59].

Table 6.5: The ZPL values calculated using PBE and HSE06 methods for NV<sup>0</sup> and NV<sup>-1</sup> defects are compared with experimental data [59].

Defect	Method	$E_{gs}$ (eV)	$E_{es}$ (eV)	ZPL (eV)	$\lambda$ (nm)
NV <sup>0</sup>	HSE06	-2259.818	-2258.179	1.638	757
	Experimental	–	–	2.156	575
NV <sup>-1</sup>	PBE	-1934.981	-1933.271	1.710	726
	HSE06	-2248.237	-2246.010	2.227	557
	Experimental	–	–	1.945	637

## 6.2 Studies of c-BN

Our research in this section will focus on the bulk properties of c-BN and its constituent elements. Boron (B) will be studied in its  $\alpha$ -rhombohedral phase, while nitrogen (N) will be studied as gas through a dimer ( $N_2$ ). The bulk properties will be investigated through lattice constants, band gap, and dielectric tensor. Furthermore, the chemical potentials will be computed from the phases of the constituent elements.

### 6.2.1 Bulk properties of c-BN

c-BN is an insulating material that has recently begun to attract the attention of researchers due to its potential use as a wide-bandgap semiconductor in quantum technology applications. However, the bulk properties of this material, such as the lattice constant, band gap, and dielectric tensor, have not yet been well-determined. These properties are important for understanding the material's behavior when doped. Therefore, in this section, we focus our efforts on determining these properties to expand our understanding of this material. Here, ab initio simulations are used to predict the properties mentioned above. Calculations to obtain the lattice constant, band structure and Density of States (DOS) were performed using an energy cutoff of 500 eV and a  $k$ -density of 4. The analysis is reported in [Section 5.1](#).

The first property to be reported is the lattice constant, which was calculated using both the PBE and HSE06 functionals. After relaxation of the unit cell, it was found that the PBE functional report a lattice constant of  $a^{PBE} = 3.626 \text{ \AA}$ , while the HSE06 functional report  $a^{HSE06} = 3.598 \text{ \AA}$ . The analysis shows that the PBE method overestimates the value, while HSE06 method underestimates the lattice constant when compared to the experimental value of  $a^{exp} = 3.616 \text{ \AA}$  [38]. However, once again, it should be noted that the ab initio simulations are

performed at 0 K, while the experimental value was reported at 300 K. Therefore, the underestimated value obtained using the HSE06 method at 0 K is acceptable, since when the temperature increases, the lattice constant will tend to expand. A summary of the previously mentioned information is presented in **Table 6.6**.

Another significant value to report is the band gap in c-BN. **Table 6.6**, once again, shows the summary of the results for the band gap calculations using both the PBE and HSE06 functionals. The PBE functional report a band gap of  $E_g^{PBE} = 4.45$  eV, while the HSE06 functional yields a value of  $E_g^{HSE06} = 5.814$  eV. Unfortunately, to date, we have not found experimental measurements of the electronic band gap in c-BN. However, experimental measurements of the optical band gap in c-BN have been found. Some studies report optical band gaps of 6.36 and 6.2 eV [38], [60]. At this point, we must be careful when comparing the electronic and optical band gaps, as they are measured differently. An electronic band gap is measured as the energy required to promote an electron from the valence band maximum (VBM) to the conduction band minimum (CBM) via electrical or thermal excitation. However, the optical band gap is measured via photon excitation. Here, the photon is the key point of the difference. In indirect band gaps, such as c-BN, the VBM and CBM occur at different momenta ( $k$ ), which implies that the promotion of an electron requires a change in both energy and momentum. However, a photon does not have enough momentum to make that change. This implies a change in energy only, but not in momentum. This means that the optical band gap is measured as a direct transition, which can yield values higher than the electronic band gap. Since ab initio simulations predict electronic band gaps, we consider the value calculated of  $E_g^{HSE06} = 5.814$  eV using the HSE06 functional to be a good estimate of the band gap in c-BN.

Table 6.6: Report of lattice constant and band gap obtained from DFT calculations using the PBE and HSE06 functionals for c-BN. The experimental lattice constant is reported at room temperature, while simulations are at 0 K. No experimental data on the electronic band gap has been found.

Method	Lattice constant (Å)	Band gap (eV)
PBE	3.626	4.450
HSE06	3.598	5.814
Experimental	3.616 [37]	-

**Fig. 6.5** shows the band structure diagram computed for bulk c-BN using the PBE (red lines) and HSE06 (blue lines) functional, where the wide band gap can be observed. As we mentioned earlier, this diagram reveals an indirect band gap in both methods, where the VBM is located at the  $\Gamma$ -point and the CBM at the

X-point. Unlike diamond, this time the CBM is located exactly at the X-point. Furthermore, the total DOS, which is the sum of the contributions from the  $s$ ,  $p$ , and  $d$  orbitals of each atom, is shown in Fig. 6.6 using the PBE (red) and HSE06 (blue) methods. The contribution of each atom is shown through the local DOS in Appendix B.

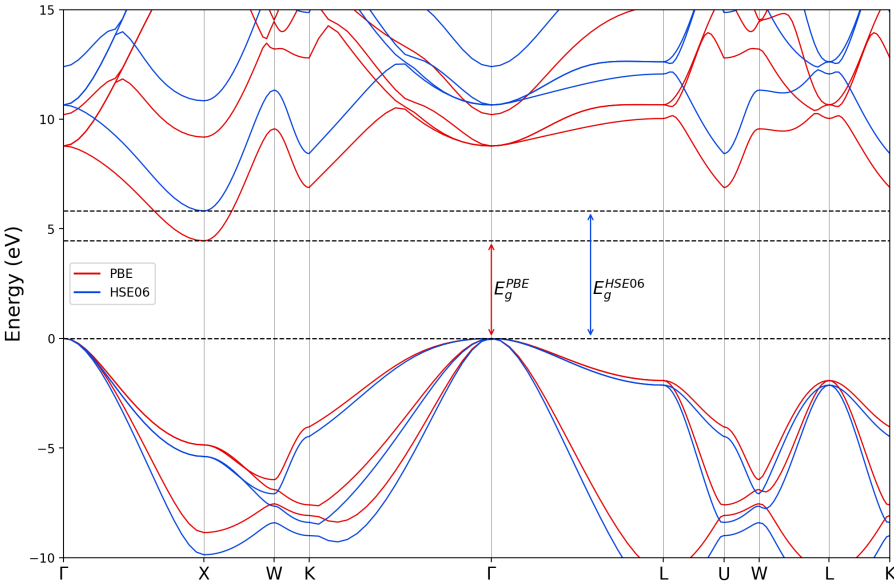


Figure 6.5: Band structure diagram computed for bulk c-BN using the PBE (red) and HSE06 (blue) functionals. Both methods reveal an indirect gap in c-BN. However, the PBE method yields a band gap of 4.450 eV, while HSE06 method yields a band gap value of 5.814 eV when the fraction of exact Hartree-Fock exchange is set to 0.25.

Considering that ab initio simulations are a powerful tool for predicting material properties, we would like to briefly dive into on the consequences of tuning the parameters in the HSE06 functional. An example in this context is when we attempt to adjust theoretical values to better match the experimental values. As mentioned in Section 4.2.3, hybrid functionals can be tuned using their  $\alpha$  and  $\omega$  parameters. For band structure calculations using Hartree-Fock theory, Koopmans' condition must be satisfied. Thus, in ab initio simulations with hybrid functionals, it is ideally assumed that the HOMO energy equals the negative ionization potential (IP), while the LUMO energy matches the negative electron affinity (EA). Although this adjustment allows for determining the band gap in agreement with experimental data, it can have some shortcomings if used improperly. An increase in  $\alpha$  tends to open the gap, but it leads to over-localization of states due to the lack of correlation effects, resulting in a lower (too negative) HOMO energy, thus violating Koopmans' condition. In addition, this also leads to less accurate total energies and spin states [61], [62]. Hence, for reliable use, the tuned  $\alpha$  and  $\omega$  parameters must first be tested with a wide range of materials.

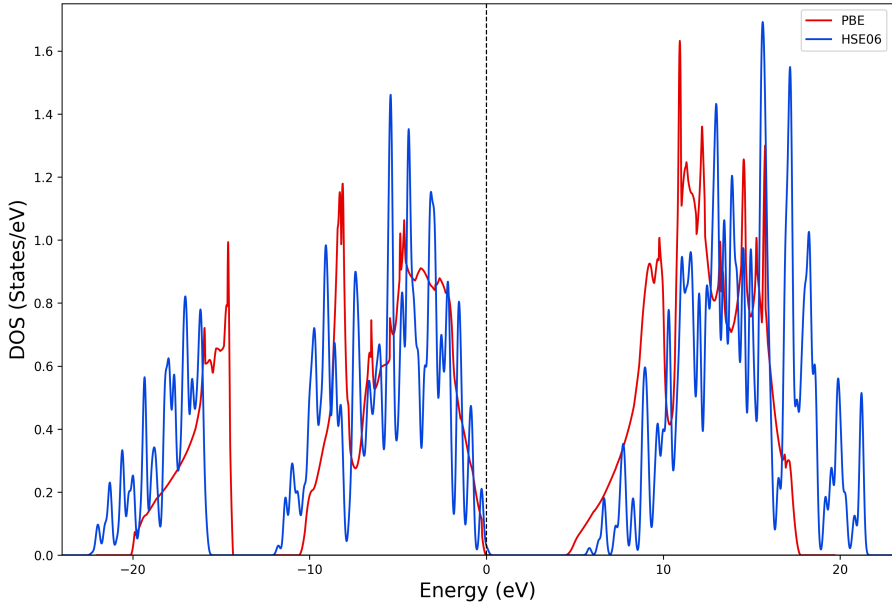


Figure 6.6: Total DOS computed for bulk c-BN using the PBE (red) and HSE06 (blue) methods.

Table 6.7: Results for the lattice constant and band gap in c-BN, when the fraction of the exact Hartree-Fock exchange ( $\alpha$ ) is varied from 0 to 1. The screening parameter was kept at its default value of  $\omega = 0.2$ . The default parameter of HSE06 was used (gray shaded area). A complete version of the table can be found in **Table C.1**.

$\alpha$	Lattice constant (Å)	Band gap (eV)
0.1	3.614	4.988
0.25	3.598	5.814
0.33	3.590	6.263

A benchmarking for the lattice constant and band gap of c-BN as a function of  $\alpha$  is shown in **Table 6.7**. The results show that an increase in  $\alpha$  significantly affects the band gap value, while the lattice constant changes slightly. For this analysis,  $\alpha$  was varied in a range from 0 to 1, that is, from a purely semi-local exchange to an entirely Hartree-Fock exchange. A point between them, when  $\alpha$  is set to 0.33, is striking, since the band gap value is then in close agreement with the experimental optical band gap (by 0.1 eV). However, as we mentioned earlier, this comparison is not correct due to the different nature of the band gaps. Even if the theoretical and experimental band gaps were of an electronic nature, the computed properties would still be incorrect. This is because tuning of the

parameters  $\alpha$  and  $\omega$  in a hybrid functional affects the prediction of the localization of states, total energies and spin states. **Fig. 6.7** illustrates the band gap and lattice constant values for c-BN as a function of  $\alpha$ .

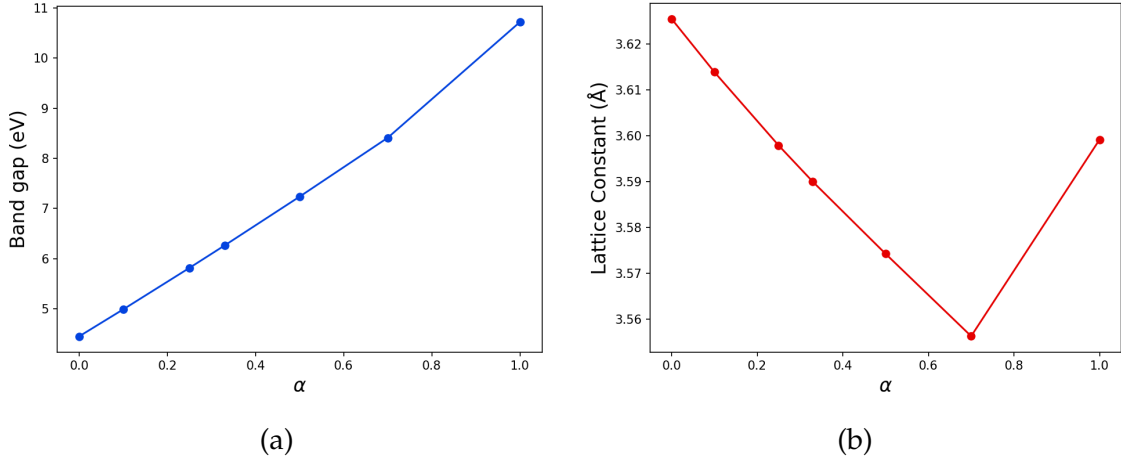


Figure 6.7: (a) Band gap and (b) Lattice constant versus the fraction of the exact Hartree-Fock exchange ( $\alpha$ ) for c-BN.

Finally, the dielectric tensor is also reported. This property is crucial to understanding the behavior of the material in the presence of an electric field. As we mentioned in **Section 4.5**, the dielectric tensor is needed to compute the finite size correction for charged defects. The ionic and electronic contributions to the dielectric tensor for c-BN computed using the PBE method are given by:

$$\epsilon_{ij}^0 = \begin{bmatrix} 2.339 & 0 & 0 \\ 0 & 2.339 & 0 \\ 0 & 0 & 2.339 \end{bmatrix}, \quad \epsilon_{ij}^\infty = \begin{bmatrix} 4.615 & 0 & 0 \\ 0 & 4.615 & 0 \\ 0 & 0 & 4.615 \end{bmatrix}. \quad (6.7)$$

Similar to diamond, c-BN is also an isotropic material, so it is expected that the off-diagonal elements will be zero. Unfortunately, no recent experimental studies on the dielectric properties of c-BN have been found. So we propose our results as a starting point for the exploration of this material.

## 6.2.2 Bulk properties of the elemental components

The bulk properties of the elements that make up the host material are vital to defining the chemical potentials for further calculations. Boron material is a semiconductor in its  $\alpha$ -rhombohedral phase, which is the most stable phase. The lattice constants and band gaps obtained for  $\alpha$ -boron using the PBE and HSE06 methods are shown in **Table 6.8** and compared to experimental values. The lattice constants,  $a^{PBE} = 5.05$  and  $a^{HSE06} = 5.028$  Å, are underestimated by both methods as compared to experiment ( $a^{exp} = 5.064$  Å). The bond angles are

reported as  $\alpha^{PBE} = \alpha^{HSE06} = 58.03^\circ$ , respectively. Both bond angles reported using the PBE and HSE06 functionals are in agreement with the experimental value of  $\alpha^{exp} = 58.09^\circ$  [63]. Regarding the band gap values, where  $E_g^{PBE} = 1.506$  eV and  $E_g^{HSE06} = 2.085$  eV, the HSE06 method is seen to be in better agreement with the experimental value, showing a difference of approximately 0.09 eV.

Table 6.8: Report of lattice constant and band gap obtained using PBE and HSE06 methods for pure boron in its  $\alpha$ -rhombohedral phase. The bond angles found are the same using both methods,  $\alpha = 58.03^\circ$ .

Method	Lattice constant ( $\text{\AA}$ )	Band gap (eV)
PBE	5.050	1.506
HSE06	5.028	2.085
Experimental	5.064 [63]	2 [64]

The other constituent of c-BN, nitrogen, is a gas, which means there are no defined lattice parameters. For the purposes of our calculations, where the goal is to calculate the chemical potentials, a nitrogen dimer ( $N_2$ ) is placed in a box. The elemental chemical potentials and enthalpy of formation for B and  $N_2$  are reported in **Table 6.9** and were calculated using **Eqs. 4.11** and **5.3**. After the relaxation of the primitive cell,  $\mu_{\text{cBN}}$  is found to be  $-17.451$  eV using the PBE method, and  $-20.365$  eV using the HSE06 method via **Eq. 4.10**. The chemical potential limits and chemical potential limits with respect to the elemental chemical potentials under different conditions are shown in **Table 6.10**.

Table 6.9: Elemental chemical potentials for boron and nitrogen using the PBE and HSE06 methods. Details of the enthalpy of formation are also added. The PBE method yields  $\mu_{\text{cBN}} = -17.451$  eV, while the HSE06 method yields  $\mu_{\text{cBN}} = -20.365$  eV.

Method	$\mu_B^{elemental}$ (eV)	$\mu_N^{elemental}$ (eV)	$\Delta H_f(\text{cBN})$ (eV)
PBE	-6.703	-8.317	-2.432
HSE06	-7.426	-10.240	-2.699

Table 6.10: The chemical potential limits ( $\mu_{\{B,N\}}$ ) and chemical potential limits with respect to the elemental chemical potentials ( $\mu_{\{B,N\}}^*$ ) under B-rich and N-rich conditions using the PBE and HSE06 methods.

Method	Conditions	$\mu_B$ (eV)	$\mu_N$ (eV)	$\mu_B^*$ (eV)	$\mu_N^*$ (eV)
PBE	B-rich	-6.703	-10.748	0	-2.432
	N-rich	-9.135	-8.317	-2.432	0
HSE06	B-rich	-7.426	-12.939	0	-2.699
	N-rich	-10.125	-10.240	-2.699	0

## 6.3 Point Defects in c-BN

Our research in this section will focus on point defects in c-BN. Four point defects are explored:  $N_B$ ,  $V_B - V_N$ ,  $V_B - C_B$ , and  $V_B - Si_B$ . Details on formation energies, energy levels, highly localized states, and the zero-phonon line are studied through analysis of the formation energy diagram, Kohn-Sham level diagrams, Inverse Participation Ratio, and the Delta Self-Consistent Field ( $\Delta$ SCF) method.

### 6.3.1 Initial defect selection

The four point defects selected for exploration in this thesis were previously analyzed, along with other potential point defects. The methodology is described in **Section 4.9**. Our small initial database consisted of native defects, impurities, and complexes. The data collection process was based primarily on the available literature and some other data proposed by us, taking into account promising point defects in other host materials. Native defects such as  $V_B$ ,  $V_N$ ,  $B_N$  and  $N_B$  were collected from literature due to their reported thermodynamic stability [65]–[67]. Although in cases such as  $B_N$  and  $N_B$  with high formation energies. Impurity defects such as  $C_B$ ,  $C_N$ ,  $O_B$  and  $O_N$  are also collected from the literature due to reports on thermodynamic stability through formation energy diagrams [66]–[68]. Continuously, complex defects such as  $V_B - C_B$ ,  $B_N - V_B$ ,  $N_B - V_N$ ,  $V_B - V_N$ ,  $V_B - O_N$  and  $V_B - Si_B$  are also included thanks to the information contained in the literature [68]–[70]. Although many of the point defects mentioned above have been studied from ab initio simulations only through their thermodynamic stability using formation energy diagrams, they are an excellent starting point. Other works also use ab initio simulations for a depth analysis of Kohn-Sham level diagrams, formation energy diagrams, ZPL, and so on. However, these works will not be used for comparison with our results, since their results are

obtained by modifying the fraction of the exact Hartree-Fock exchange ( $\alpha = 0.33$ ). As we explained in **Section 6.2.1**, we consider this modification to be inappropriate. Finally, we also propose complex defects such as  $V_N - C_N$ ,  $C_B - V_N$ ,  $C_N - V_B$ ,  $C_B - C_N$ ,  $C_B - C_B$  and  $C_N - C_N$  taking as examples some previous defects, NV center in diamond or by letting the imagination fly.

The first stage of this process was the PBE calculation, that is, the use of the PBE functional. All the previously mentioned defects were subjected to this initial calculation. A deep analysis was performed through formation energy diagrams, Kohn-sham states diagrams, spin state and localization of states. Point defects such as  $V_B^{-1}$ ,  $N_B^{+1}$ ,  $(V_B - C_B)^{-1}$ ,  $(V_B - C_B)^0$ ,  $(V_B - V_N)^{-1}$ ,  $(V_B - V_N)^0$  and  $(V_B - Si_B)^0$ , were notable due to their thermodynamic stability, band gap energy level introduction, highly localized states and desired spin states ( $S = 1$  or  $1/2$ ). Thus, these 6 defects were selected for the next stage.

The next step was to perform the calculations using the HSE06 functional, but only for the previously selected defects. Here, some of the selected defects, such as  $(V_B - C_B)^{-1}$  and  $(V_B - V_N)^{-1}$ , reported numerical and convergence problems in our calculations. Therefore, they were discarded. On the other hand, defects such as  $N_B^{+1}$ ,  $(V_B - C_B)^0$ ,  $(V_B - V_N)^0$  and  $(V_B - Si_B)^0$  continued to show the promising characteristics found with PBE calculations. Thus, they were selected for future calculations such as ZPL and spin coherence. In addition, the native defect  $V_B^{-1}$  showed some interesting characteristics; however, it was discarded for ZPL calculations. The reasons for this conclusion are presented in our results, since  $V_B^{-1}$  is taken as an example.

The details of our results for the  $N_B^{+1}$ ,  $(V_B - C_B)^0$ ,  $(V_B - V_N)^0$  and  $(V_B - Si_B)^0$  defects in the final stage, using the HSE06 functional, will be presented in the following sections. The analysis of the results includes a review of thermodynamic stability, formation energy diagrams, Kohn-Sham level diagrams, spin state, localized states and ZPL calculations.

### 6.3.2 Formation energy diagram

In this section, we will present the formation energy diagrams for the defects selected, which include curves with different charge states in defects such as  $V_B$ ,  $N_B$ ,  $V_B - V_N$ ,  $V_B - C_B$ ,  $V_B - Si_B$ .

After analyzing the final stage of the process selection using the HSE06 functional, six defects with specific charge states emerged as promising candidates due to their thermodynamic stability:  $N_B^{+1}$ ,  $(V_B - C_B)^0$ ,  $(V_B - V_N)^0$  and  $(V_B - Si_B)^0$ . All of them show charge transitions near the mid-gap, and although some have a high formation energy, they could be interesting to analyze further. **Fig. 6.8** shows the formation energy diagram for selected defects under Boron rich (B-rich) conditions, while **Fig. 6.9** shows the same diagram under Nitrogen rich (N-rich) conditions. Both were plotted using the PBE (dashed lines) and HSE06 (solid lines) methods. Here, the curve computed using the PBE method is incorporated into the HSE06 method plot for illustrative purposes only.

The curve for the boron vacancy  $V_B$  is plotted in **Fig. 6.8** and **Fig. 6.9** using a charge state range from  $-4$  to  $+1$ . It can be observed under B-rich conditions

that  $V_B^{-3}$  exhibits the lowest formation energy and is therefore the dominant defect charge state under n-type conditions in both PBE and HSE06 methods. In addition, boron vacancies are found to act as acceptors with no donor transitions in the band gap.

The  $N_B$  defect, which was plotted using a charge state range from  $-2$  to  $+3$ , has the highest formation energy among all defects under B-rich conditions (see Fig. 6.8). This means that when there is almost no nitrogen in the environment, it becomes more difficult to form  $N_B$  defects. However, the situation are more favorable under N-rich conditions, since the formation energy is lower (see Fig. 6.9). Here,  $N_B^{+2}$  has the lowest formation energy and donor behavior (p-type). On the other hand,  $V_B - V_N$ , which was plotted using a charge state range from  $-3$  to  $+3$ , is independent of the conditions in which it is found, since the formation energy is the same under both B-rich and N-rich conditions. The charge state with the lowest formation energy is  $(V_B - V_N)^{-2}$ , which is an acceptor. Finally,  $V_B - C_B$  and  $V_B - Si_B$ , which were plotted using a charge state range from  $-3$  to  $+2$ , are also favorable under N-rich conditions. Notably,  $V_B - Si_B$  is more favorable due to its the lowest formation energy, even lower than that of the other defects.

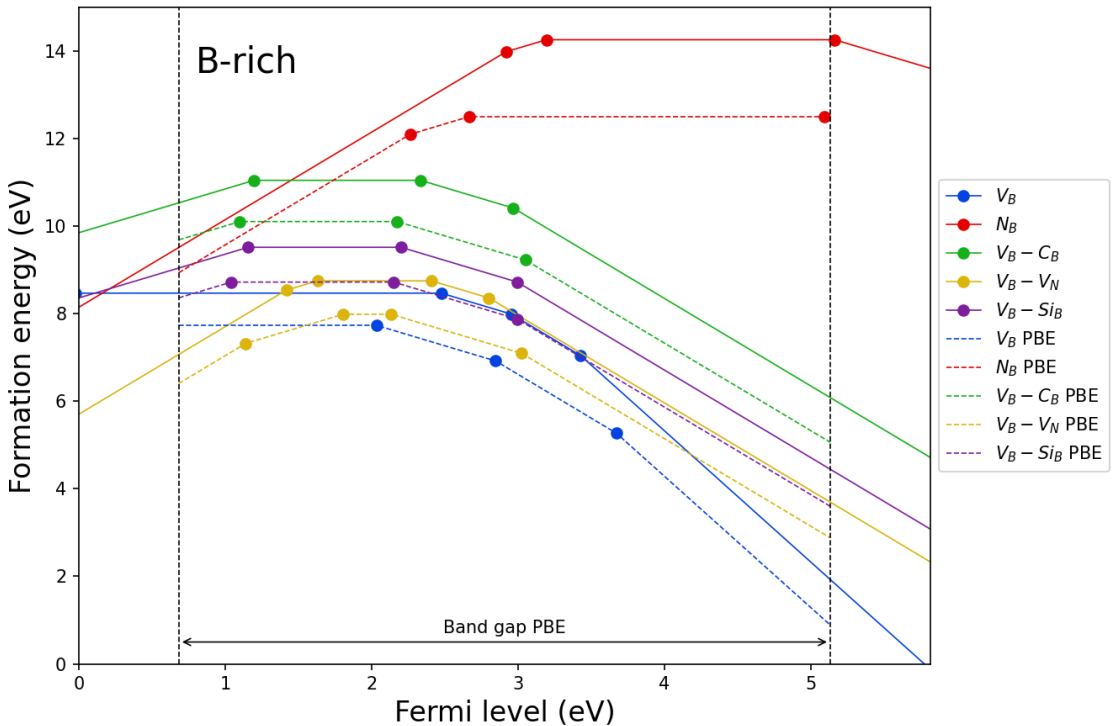


Figure 6.8: Formation energy diagram for point defects in c-BN under B-rich conditions. Calculations were performed using the PBE and HSE06 methods. The band gap obtained with the PBE method is 4.45 eV, while with the HSE06 method it is 5.814 eV. The solid lines represent the HSE06 method, while the dashed lines correspond to the PBE method. The curve computed using the PBE method is centered into the plot for illustrative purposes.

**Table 6.11** shows the detailed information on thermodynamic transition levels

for native and complex defects under B-rich and N-rich conditions, using both the PBE and HSE06 methods. Finite-size corrections were taken into account. In addition, a report on charge state, total energy of the defective supercell, energy corrections and  $\xi_{form}^q$ , which satisfy Eqs. 4.26 and 4.29, is given for native and complex defects under B-rich and N-rich conditions in **Tables E.1** and **E.2** using PBE method, and **Tables E.3** and **E.4** using HSE06 method in **Appendix E**.

For our purposes, defects near the midgap, such as  $V_B^{-2}$ ,  $V_B^{-1}$ ,  $N_B^0$ ,  $N_B^{+1}$ ,  $(V_B - C_B)^{-1}$ ,  $(V_B - C_B)^0$ ,  $(V_B - V_N)^{-1}$ ,  $(V_B - V_N)^0$ ,  $(V_B - Si_B)^{-1}$  and  $(V_B - Si_B)^0$  are assumed to be more interesting for QT applications. This is because they could introduce well-defined energy levels near the mid-gap, which is favorable for hosting highly localized states. However, we can not yet conclude that these defect states are suitable for quantum applications as SPEs or spin qubits, since they must also satisfy additional requirements. These requirements involve satisfying features such as energy levels within the band gap, highly localized electronic states, optically active defect, and a paramagnetic ground state.

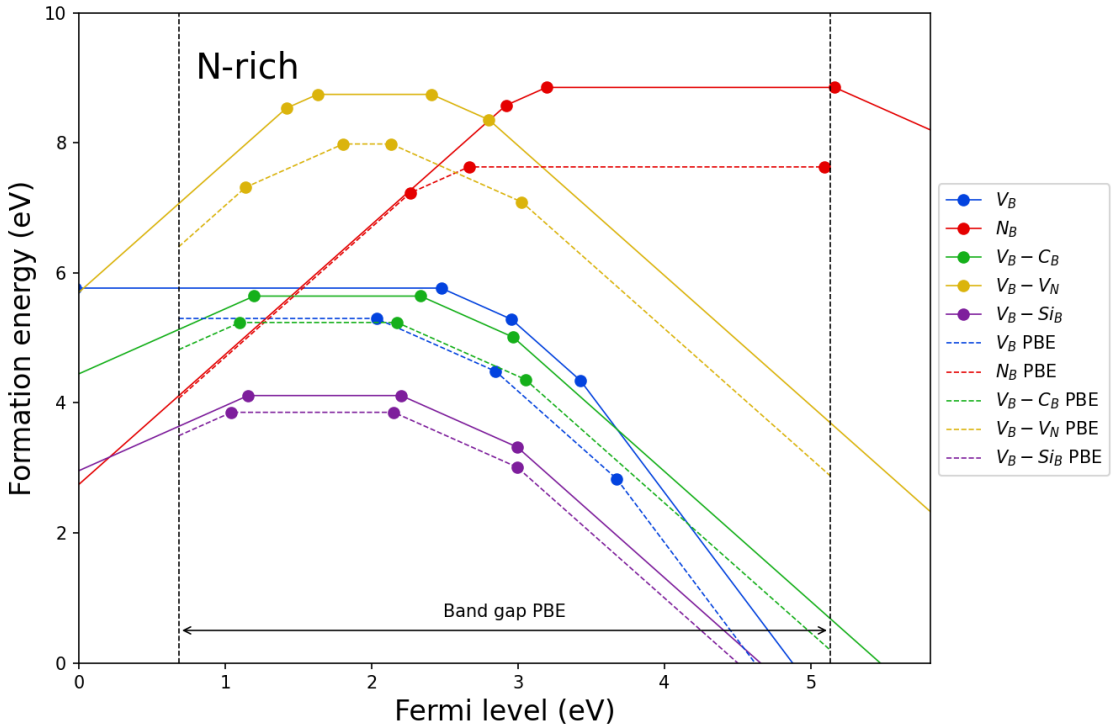


Figure 6.9: Formation energy diagrams for point defects in c-BN under N-rich conditions. Calculations were performed using the PBE and HSE06 methods. The band gap obtained with PBE method is 4.45 eV, while with HSE06 method is 5.814 eV. The solid line represents the HSE06 method, while the dashed line corresponds to the PBE method.

Table 6.11: Details of the thermodynamic transition levels with respect to the Fermi level ( $E_F$ ) and Formation energy for native and complex defects in c-BN under B-rich and N-rich conditions ( $E_{form}[\{B, N\}\text{-rich}]$ ). Both PBE and HSE06 methods are included.

Thermodynamic		$E_F$ (eV)		$E_{form}[\text{B-rich}]$ (eV)		$E_{form}[\text{N-rich}]$ (eV)	
Defect	transition levels	PBE	HSE06	PBE	HSE06	PBE	HSE06
$V_B$	$\varepsilon(0, -1)$	1.350	2.475	7.731	8.465	5.299	5.766
	$\varepsilon(-1, -2)$	2.165	2.954	6.916	8.465	4.485	5.286
	$\varepsilon(-2, -3)$	2.990	3.425	5.265	7.985	2.834	4.345
$N_B$	$\varepsilon(+2, +1)$	1.581	2.917	12.092	13.975	7.229	8.577
	$\varepsilon(+1, 0)$	1.982	3.193	12.493	14.251	7.630	8.853
	$\varepsilon(0, -1)$	4.409	5.161	12.493	14.251	7.630	8.853
$V_B - V_N$	$\varepsilon(+2, +1)$	0.459	1.417	7.318	8.533	7.318	8.533
	$\varepsilon(+1, 0)$	1.124	1.631	7.983	8.746	7.983	8.746
	$\varepsilon(0, -1)$	1.451	2.409	7.983	8.746	7.983	8.746
	$\varepsilon(-1, -2)$	2.343	2.801	7.090	8.355	7.090	8.355
$V_B - C_B$	$\varepsilon(+1, 0)$	0.419	1.197	10.100	11.041	5.237	5.643
	$\varepsilon(0, -1)$	1.491	2.334	10.100	11.041	5.237	5.643
	$\varepsilon(0 - 1, -2)$	2.367	2.967	9.224	10.408	4.361	5.010
$V_B - Si_B$	$\varepsilon(+1, 0)$	0.361	1.157	8.718	9.512	3.855	4.113
	$\varepsilon(0, -1)$	1.468	2.201	8.718	9.512	3.855	4.113
	$\varepsilon(-1, -2)$	2.311	2.994	7.875	8.718	3.011	3.320

### 6.3.3 Kohn-Sham level diagrams

Similar to the analysis for the NV center in diamond that was presented as a benchmark case in [Section 6.1.3](#), Kohn-Sham (KS) level diagrams will also here be used as useful tools to approximate the arrangement of internal defect energy levels within the c-BN band gap. Although diamond and c-BN share the same crystal structure, zincblende, they belong to different point groups. Diamond has an  $O_h$  symmetry, while c-BN has a  $T_d$  symmetry. Note that both materials have high symmetry.

The introduction of defects into the host materials tends to modify their

crystalline structures through the lattice distortions. However, this not only implies a geometric modification around the defect but also affects the symmetry of the host material and its band structure. This is why we will now examine in detail how the selected defects affect the symmetry and band structure in c-BN. After the relaxation of the system using the HSE06 functional, the  $V_B^{-1}$  defect does not break the initial symmetry of the host material, thus maintaining the  $T_d$  symmetry. This means that the geometric modification around the boron vacancy is minimal or insignificant. This  $T_d$  symmetry will be important for labeling the energy levels introduced for the defect, but no only that. In fact, there is more physics involved than we might think. Point group theory classifies crystal materials based on the collection of symmetries they present, such as rotations, reflections, inversions and so on. When a defect is introduced into a host material, the collection of symmetries is reduced (broken) due to the local effects of the defect. That is, all the initial symmetries of the host material are no preserved. Point groups have associated irreducible representations, which arise as a consequence of the symmetry operations. These irreducible representations can not be decomposed into simpler ones, and are closely related to the wave functions that describe the crystal. Thus, the wave functions associated with an energy level can be labeled according to the irreducible representations of a corresponding point group [26]. For example, in  $T_d$ , the irreducible representations are  $A_1$ ,  $A_2$ ,  $E$ ,  $T_1$  and  $T_2$ . Here,  $A_1$  and  $A_2$  represent non-degenerate levels,  $E$  represents doubly-degenerate levels, and  $T_1$  and  $T_2$  represent triply-degenerate levels. Note that, for correct labeling, an analysis of the wave function symmetries must be carried out. Although it may be obvious in some cases, in others it can lead to confusion. Thus, we would like to clarify that no symmetry analysis of the wave functions associated with the energy levels has been performed in this thesis. The labeling of the energy levels within the band gap was done by taking into account the correspondence of band indices between both spin channels. The labels used within the band gap are:  $a_1$ ,  $e_x$  and  $e_y$ . The KS level diagram for  $V_B^{-1}$  defect is shown in Fig. 6.10a. Although this defect exhibits the desired spin state  $S = 1$ , the arrangement of the levels is not the most favorable, since the difference energy between the promising levels in the spin down channel is too small (approximately 0.53 eV) to promote an electron. This makes the material susceptible to small thermal excitations, since electrons can be easily promoted from the HOMO to the LUMO. This is an important example demonstrating that features such as thermodynamic stability, highly localized states within the band gap and a desirable spin state are not sufficient on their own, but that a reasonable separation between the promising levels is also crucial. This is why this defect will be excluded from calculations for the ZPL.

**Fig. 6.10b** shows the degree of localization of the KS states within the band gap for both spin channels (spin up in top panel and spin down in bottom panel) for  $V_B^{-1}$ . The IPR measures the degree of localization of the KS states, ranging from 0 to 1 on the y-axis, while their corresponding energies within the band gap are shown on the x-axis. Note that all the KS states within the band gap are highly localized in both spin channels.

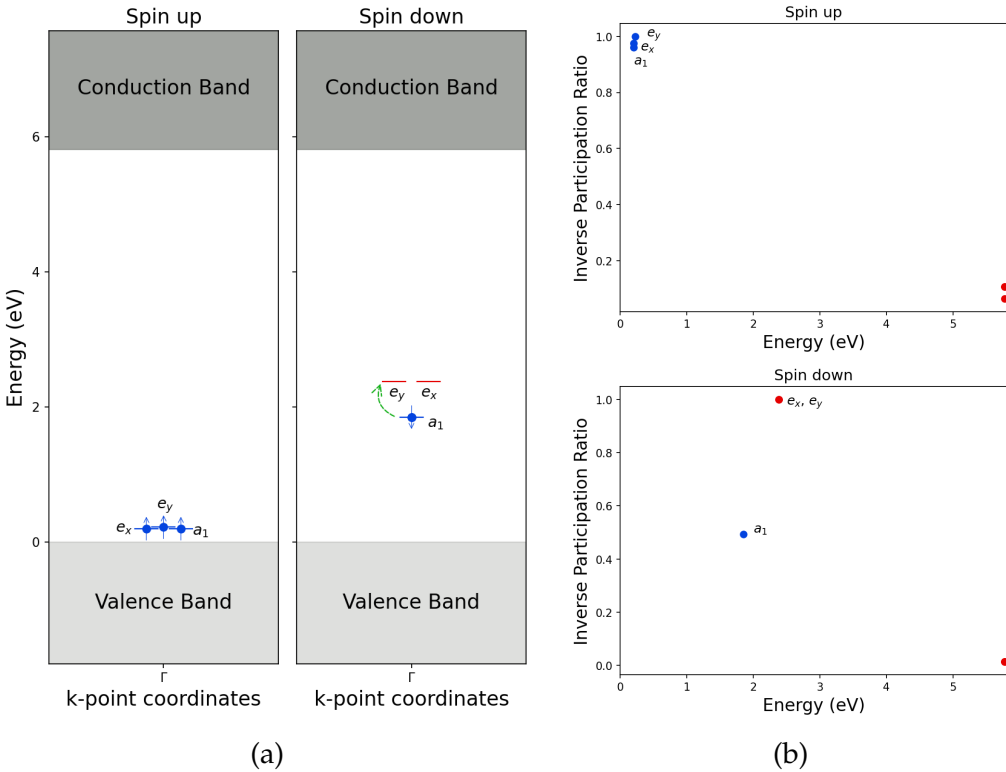


Figure 6.10: (a) Kohn-Sham level diagram and (b) IPR for the  $V_B^{-1}$  defect in c-BN computed using the HSE06 method. The occupied levels are depicted by blue balls and either an upward or downward arrow for spin up or down, respectively, while the unoccupied levels are depicted by red balls and solid lines. The green dashed curved arrow represents the promotion of an electron from an occupied level to an unoccupied level.

**Fig. 6.11** shows the next cases for our analysis. Both were selected due to their thermodynamic stability, as analyzed through formation energy diagrams. Additionally, characteristics that will be discussed below were also considered. The first of these is the  $N_B^{+1}$  defect. After the relaxation of the supercell, this defect also preserves the  $T_d$  symmetry of the lattice, but exhibits a spin state  $S = 1/2$ . Similar to the previous case ( $V_B^{-1}$ ), no symmetry analysis of the wavefunction associated with the energy levels has been carried out for this defect either. Thus, the labeling of the energy levels within the band gap was done by taking into account the correspondence of band indices between both spin channels. The labels used within the band gap are:  $a_1$  and  $t_2$ .

Regarding the arrangement of the single-particle levels, this is shown in **Fig. 6.11a**. The spin up channel reveals the most interesting case due the arrangement of the energy levels, where the  $a_1$  and  $t_2$  levels are separated by approximately 2.7 eV. Furthermore, the unoccupied triply degenerate level  $t_2$  lies 0.64 eV below the CBM. The high localization of states in both  $a_1$  and  $t_2$  levels is shown in **Fig. 6.12a**. Here, it can be observed that the  $a_1$  level has a occupied electronic state is more localized compared to the unoccupied state in the  $t_2$  level. This opens the door for us to promote an electron from the HOMO to the LUMO.

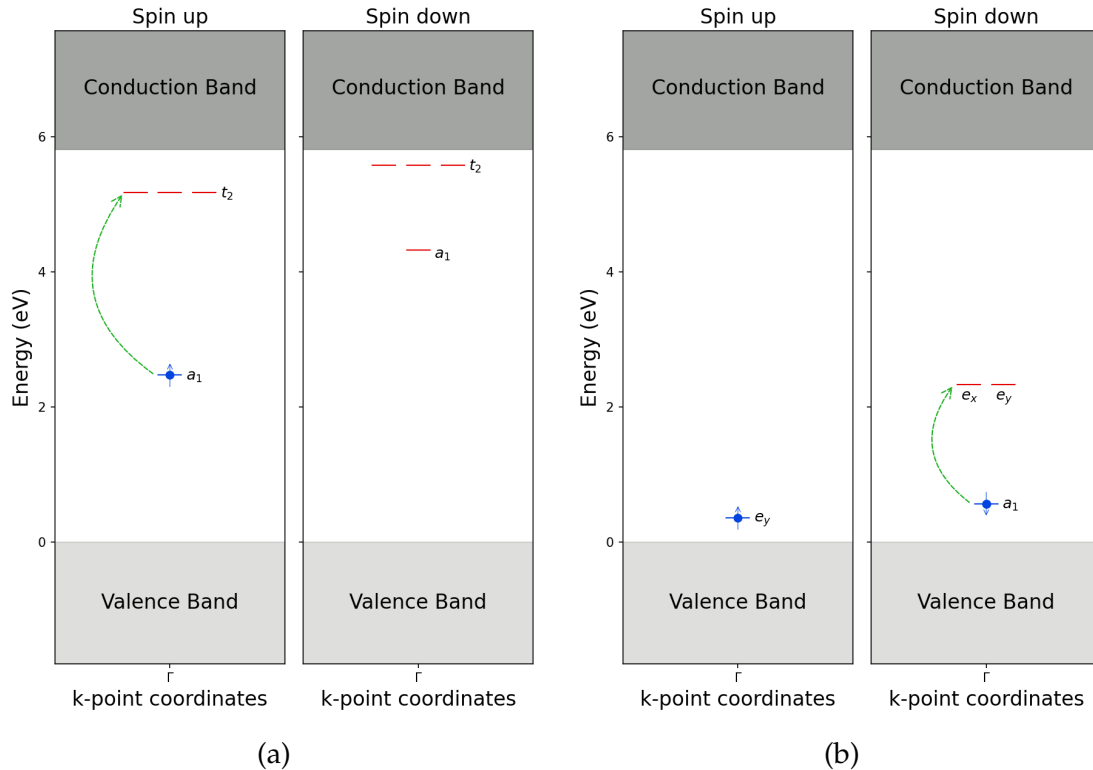


Figure 6.11: Kohn-Sham level diagrams of the (a)  $N_B^{+1}$  and (b)  $(V_B - V_N)^0$  defects in c-BN computed using the HSE06 method. The occupied levels are depicted by blue balls and either an upward or downward arrow, while the unoccupied levels are depicted by red balls and solid lines. The green dashed curved arrow represents the promotion of an electron from an occupied level to an unoccupied level.

This transition is therefore selected for further study and ZPL calculation.

The KS level diagram for  $(V_B - V_N)^0$  defect is shown in Fig. 6.11b. This figure shows an interesting arrangement of single-particle levels in the spin down channel, since it is similar to that of the  $NV^{-1}$  center in diamond, featuring both non-degenerate and degenerate levels. However, there is a smaller energy difference between the  $a_1$  and  $e_1$  ( $e_y$ ) levels for the  $(V_B - V_N)^0$  defect as compared to the  $NV^{-1}$  center of 2.954 eV, at approximately 1.77 eV. This similarity can be explained by the fact that, after the relaxation using the HSE06 functional, the di-vacancy reduces the symmetry of the host material from  $T_d$  to  $C_{3v}$  symmetry. The  $C_{3v}$  symmetry has irreducible representations  $A_1$ ,  $A_2$ , and  $E$ . Although this defect has the same symmetry as the NV center in diamond, we can not be sure that the labels correspond in the same way. Since we have not carried out a symmetry analysis of the wave function associated with the energy levels for this defect, the labeling of the energy levels within the band gap was done by taking into account the correspondence of band indices between both spin channels. The labels used within the band gap are:  $a_1$ ,  $e_x$  and  $e_y$ .

Additionally, Fig. 6.12b shows the localization of the states, where the unoccupied states in the doubly degenerate level are strongly localized. This

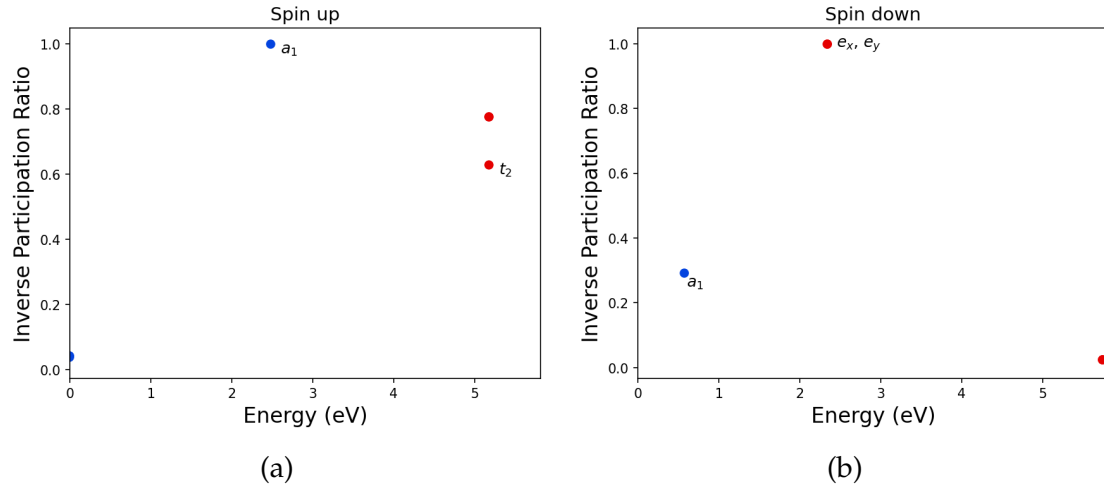


Figure 6.12: IPR for the (a)  $N_B^{+1}$  defect in the spin up channel and (b)  $(V_B - V_N)^0$  defect in the spin down channel computed using the HSE06 method. The occupied and unoccupied electronic states are represented by blue and red balls, respectively. The energy range goes from 0 to  $E_g = 5.814$  eV.

is crucial to promote an electron to them from a level with lower energy, thus enabling the ZPL calculation. This defect, similar to the  $NV^{-1}$  center in diamond, exhibits a spin state of  $S = 1$ .

Finally, the last two defects are shown in Fig. 6.13. Both were selected due to their thermodynamic stability, as analyzed through formation energy diagrams. Additionally, characteristics that will be discussed below were also considered. After the relaxation using the HSE06 functional, both  $(V_B - C_B)^0$  and  $(V_B - Si_B)^0$  defects yield a spin state of  $S = 1$ , in addition to reducing the symmetry of the host material to a  $C_{1h}$  symmetry. This abrupt reduction in symmetry is due to the most severe geometric distortion caused by the boron vacancy along with an substitutional impurity (carbon or silicon). Since the silicon atom is much larger than the carbon atom, it would not be illogical to expect a greater lattice deformation in the  $(V_B - Si_B)^0$  defect. However, our calculations report similar degrees of deformation around both defects. Here, the  $C_{1h}$  symmetry has the following irreducible representations:  $A'$  and  $A''$ . Same to the previous cases, we have not carried out a symmetry analysis of the wave function associated with the energy levels for this defect. Thus, the labeling of the energy levels within the band gap was done by taking into account the correspondence of band indices between both spin channels. The labels used within the band gap are:  $a_1$ ,  $a'$  and  $a''$ .

For  $(V_B - C_B)^0$ , Fig. 6.13a reveals that there are only non-degenerate levels within the band gap. The spin down channel is the most promising for the promotion of electrons and, consequently, for computing the ZPL. In the spin down channel, the energy difference between the levels located in HOMO and LUMO,  $a_1$  and  $a'$ , is approximately 1.41 eV. However, the energy difference between the two unoccupied levels,  $a'$  and  $a''$ , is much smaller (around 67 meV). In Fig. 6.14a, the highly localized states in spin down channel can be seen. All the

states are well-localized, thus confirming their suitability for computing the ZPL.

The KS level diagram for the  $(V_B - Si_B)^0$  defect is shown in Fig. 6.13b. The figure reveals an arrangement of levels very similar to the  $(V_B - C_B)^0$  defect in the spin down channel, but with a more noticeable separation between the  $a'$  and  $a''$  levels. This energy difference is approximately 337 meV, while the energy difference between  $a_1$  and  $a'$  is approximately 1.31 eV. Confirmation of the high localization of the states can be seen in Fig. 6.14b.

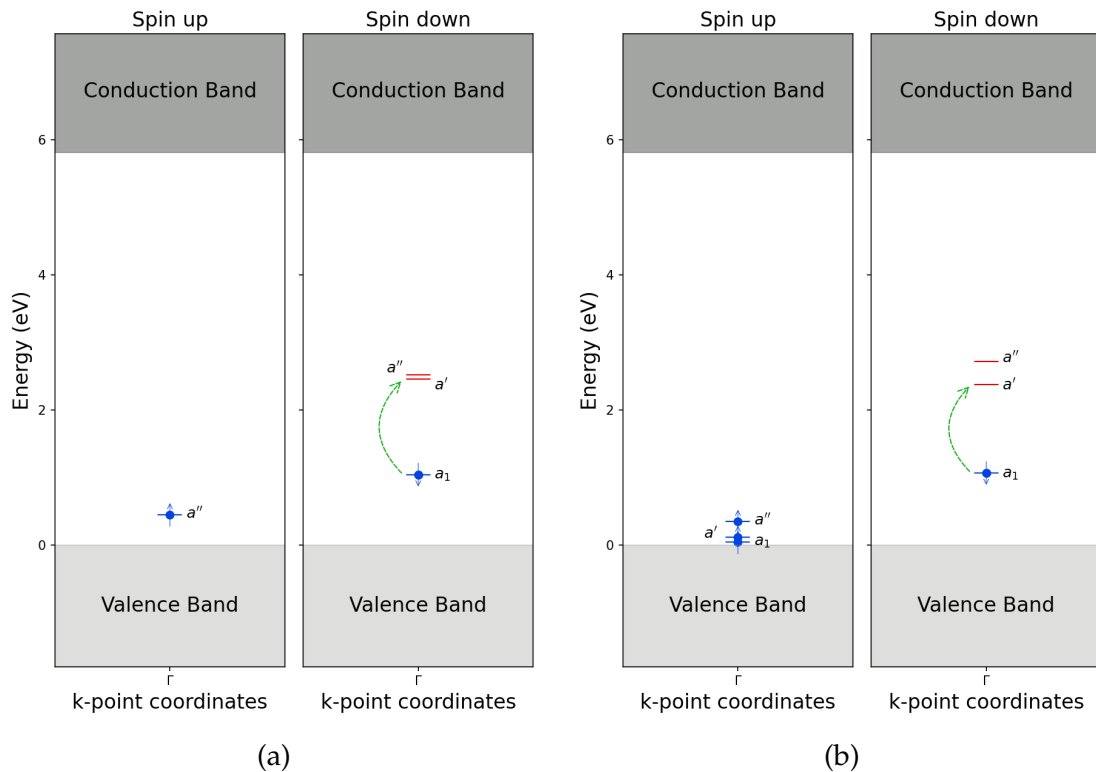


Figure 6.13: Kohn-Sham level diagrams of the (a)  $(V_B - C_B)^0$  and (b)  $(V_B - Si_B)^0$  defects in c-BN using the HSE06 method. The occupied levels are depicted by blue balls and either an upward or downward arrow, while the unoccupied levels are depicted by red balls and solid lines. The green dashed curved arrow represents the promotion of an electron from an occupied level to an unoccupied level.

At this point, after analyzing the promising spin channels for each defect, we can realize that energy levels near the mid-gap tend to have associated states that are more localized than those near the VBM and CBM. This behavior arises because these levels are well isolated, that is, they lie far from the valence and conduction bands. This separation prevents interaction or hybridization of the defect-associated states with states belonging to the valence and conduction bands, thus avoiding delocalization. As a complement to the KS level diagrams, Tables 6.12 and 6.13 provide detailed information on the internal energy levels within the band gap of the  $N_B^{+1}$ ,  $(V_B - V_N)^0$ ,  $(V_B - C_B)^0$  and  $(V_B - Si_B)^0$  defect charge states. This information focuses only on the most promising channels of the defects described above.

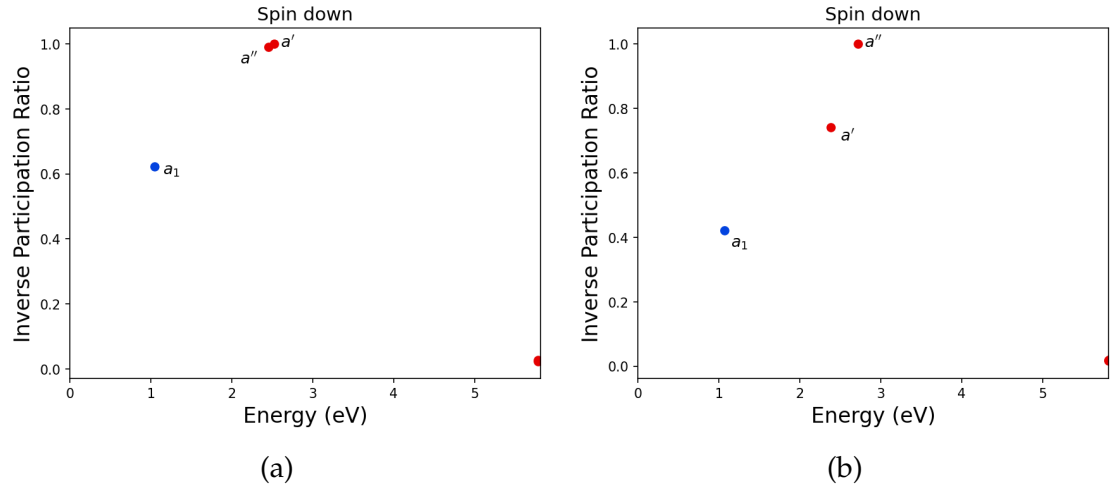


Figure 6.14: IPR for the (a)  $(V_B - C_B)^0$  defect and (b)  $(V_B - Si_B)^0$  defect, both in the spin down channel computed using the HSE06 method. The occupied electronic states are represented by blue balls, while the unoccupied states are represented by red balls. The energy range goes from 0 to  $E_g = 5.814$  eV.

Table 6.12: Energies for each level within the band gap for the native defects using HSE06 method. The table only includes information for the most promising channels, along with their band indices. An asterisk indicate the level is occupied.

Defect	Channel	States	Band index	Energy (eV)
$V_B^{-1}$	Spin down	$a_1$	430	1.849 (*)
		$e_x$	431	2.383
		$e_y$	432	2.383
$N_B^{+1}$	Spin up	$a_1$	433	2.474 (*)
		$t_2$	434	5.174
		$t_2$	435	5.174
		$t_2$	436	5.174

Table 6.13: Energies for each level within the band gap for the complex defects using HSE06 method. The table only includes information for the most promising channels, along with their band indices. An asterisk indicate the level is occupied.

Defect	Channel	States	Band index	Energy (eV)
$(V_B - V_N)^0$	Spin down	$a_1$	427	0.569 (*)
		$e_x$	428	2.335
		$e_y$	429	2.335
$(V_B - C_B)^0$	Spin down	$a'$	431	2.456
		$a''$	432	2.523
		$a_1$	430	1.044 (*)
$(V_B - Si_B)^0$	Spin down	$a'$	431	2.378
		$a''$	432	2.715
		$a_1$	430	1.068 (*)

### 6.3.4 Zero Phonon Line

In this section, electron promotion from HOMO to LUMO will be carried out to calculate the ZPL value. The methodology to compute the ZPL using the HSE06 method will be exactly the same as explained in **Section 6.1.4**. That is, the occupancies for a doubly degenerate level will be split in 0.5 – 0.5, while for a triply degenerate level, it will be split into 0.33 – 0.33 – 0.33.

For  $N_B^{+1}$ , electron promotion occurs from a non-degenerate level ( $a_1$ ) to a triply degenerate level ( $t_2$ ) in the spin up channel (see **Fig. 6.11a**). Ideally, using the HSE06 method, the configurations for its ground and excited states should be given by  $^2A$  and  $^2T$ :

$$^2A : a_1^1 t_2^0 \longrightarrow ^2T : a_1^0 t_2^1. \quad (6.8)$$

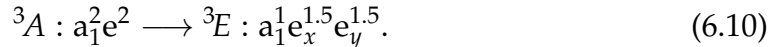
However, since the occupation is split equally, it is expressed as:

$$^2A : a_1^1 t_2^0 \longrightarrow ^2T : a_1^0 t_2^{0.33} t_2^{0.33} t_2^{0.33}. \quad (6.9)$$

We use the capital labels  $A$  and  $T$  simply to distinguish between the ground and excited states, while the superscript indicates the spin state multiplicity (triplet, doublet, singlet). The calculated ZPL values for this defect are reported in the top portion of **Table 6.14** and were obtained using the PBE and HSE06 methods. Importantly, the table shows that both methods yield very similar values for the  $N_B^{+1}$  defect. The energy difference is approximately 29 meV, while

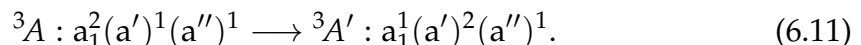
the wavelength difference is 14 nm. Both wavelengths calculated falls within the visible spectrum, specifically in the red region, which could enable the defect to act as a color center for the detection and control of qubits.

As mentioned earlier, the calculations for the  $(V_B - V_N)^0$  defect an arrangement of single-particle levels consisting of a non-degenerate and a degenerate level, separated by an energy of 1.77 eV. The electron promotion must occur between the  $a_1$  and  $e_x - e_y$  levels in the spin down channel (see **Fig. 6.11b**), so the occupancy will be split equally. Thus, the configuration for the ground and excited states is given by:



We use the capital labels  $A$  and  $E$  simply to distinguish between the ground and excited states, while the superscript indicates the spin state multiplicity (triplet, doublet, singlet). The results in **Table 6.14** show a ZPL value for the  $(V_B - V_N)^0$  defect, calculated using the PBE method, is too small for QT applications, around 0.11 eV. Consequently, the corresponding wavelength that too is larger, around 11266 nm. This is not relevant for our purposes. However, the ZPL value calculated using the HSE06 method is much more promising, since the defect emits at telecom wavelengths (S band). Here, the ZPL value is approximately 0.826 eV, which gives a wavelength of 1503 nm. This could be highly useful for quantum communication applications, such as fiber-optic networks. Although the S band is not as widely used as the C or L bands at present, it could become a potential option in the near future. Note that there is a large difference between the ZPL values calculated using PBE and HSE06 functionals; this could be a bit strange. However, no numerical or convergence problems have been reported in our calculations.

For the  $(V_B - C_B)^0$  defect, electron promotion occurs from an occupied non-degenerate level ( $a_1$ ) to an unoccupied non-degenerate level ( $a'$ ) in the spin down channel (see **Fig. 6.13a**). The configurations for both ground and excited states are given by  $^3A$  and  $^3A'$ :



We use the capital labels  $A$  and  $A'$  simply to distinguish between the ground and excited states, while the superscript indicates the spin state multiplicity (triplet, doublet, singlet). Regarding the ZPL values, these are also included in **Table 6.14**. Similar to the previous defect, this one also shows potential for quantum communication applications. The ZPL value calculated using the HSE06 method is approximately 0.933 eV, which is about 0.5 eV higher than the value calculated using the PBE method. The reported promising wavelength is 1331 nm, which falls within the telecom O-band.

Table 6.14: The ZPL values calculated using PBE and HSE06 methods for point defects defects in c-BN.

Defect	Method	$E_{gs}$ (eV)	$E_{es}$ (eV)	ZPL (eV)	$\lambda$ (nm)
$N_B^{+1}$	PBE	-1885.828	-1884.159	1.669	743
	HSE06	-2200.669	-2199.028	1.640	757
$(V_B - V_N)^0$	PBE	-1859.307	-1859.197	0.110	11266
	HSE06	-2170.127	-2169.301	0.826	1503
$(V_B - C_B)^0$	PBE	-1870.328	-1869.913	0.415	2990
	HSE06	-2183.891	-2182.959	0.933	1331
$(V_B - Si_B)^0$	PBE	-1868.037	-1867.634	0.403	3077
	HSE06	-2181.164	-2179.909	1.256	988

Finally, for the  $(V_B - Si_B)^0$  defect, electron promotion occurs in the same way and within the same spin channel as in the previous case (see Fig. 6.13b). Therefore, the configurations for its ground and excited states are also represented by Eq. 6.11. Once again, Table 6.14 shows the results for this defect. The PBE method yields a ZPL value that is too small for QT applications, approximately 0.4 eV, with a respective wavelength of 3077 nm. For our purposes, this is not interesting since the wavelength falls within the mid-infrared range. However, the HSE06 functional increases the energy difference between the ground and excited states, yielding a ZPL value of approximately 1.26 eV. The defect is thus predicted by hybrid DFT to emit at a wavelengths of 988 nm, which also falls within the telecom range (near-infrared range). However, this wavelength is only suitable for short-distance transmission using fiber-optic technology in quantum communication.

Note that in cases such as  $(V_B - V_N)^0$ ,  $(V_B - CB)^0$ , and  $(VB - Si_B)^0$ , the difference between the ZPL values computed using the PBE and HSE06 functionals is higher. This energy difference could be a consequence of using a relatively small supercell of 216 atoms in c-BN ( $3 \times 3 \times 3$ ). Unlike very large supercells, small supercells are more prone to spurious interactions due to defect-defect interactions and artificial lattice distortions. These distortions could be influencing the total energies when the HSE06 method is used, as it is more sensitive to local effects.

## 6.4 Spin Coherence

The NV center in diamond, specifically in its charge state  $-1$ , is a well-studied material currently. Many researchers have dedicated and continue to dedicate their efforts to investigating and understanding the promising properties presented by this defect. Although the NV center in diamond faces challenges related to scalability for device manufacturing due to its hardness, it can serve as a good guide for searching of new host materials. Since properly knowing and applying the methods, either theoretical or experimental, is crucial for analyzing point defects in new host materials. That is why, throughout this thesis, the NV center in diamond has been used as a guide for our exploration of point defects in c-BN.

In this section, we will study the spin coherence in  $\text{NV}^{-1}$  defect in diamond through the CCE method. Unfortunately, we will not present results for our promising defects in c-BN. This is because we have not been able to perform the spin coherence calculations for c-BN. The methodology for implementing the spin coherence calculations in c-BN was the same as in our calculations for diamond. However, the calculations did not work, and the reasons are unknown.

As outlined in [Section 4.8](#), the lifetime of the defect spin (central spin) is primarily conditioned by its interactions with nuclear spins (the spin bath). However, considering the entire spin bath is computationally expensive. Therefore, in simulations using the CCE method, convergence tests on certain crucial parameters are required. This helps reduce computational cost without affecting the accuracy or reliability of the calculations. Hence, a restriction must be imposed on the size of the spin bath. That is, on the number of nuclear spins that should be included in the bath. In the PyCCE implementation, this is possible through a parameter known as the bath cutoff radius ( $r_{\text{bath}}$ ), which is measured from the position of the central spin. On the other hand, the clusters included in this method also require restrictions on the number of nuclear spins and the distances between them. The size of the cluster is conditioned by the order of the CCE method. That is, CCE1 consists of single nuclear spins, CCE2 includes both single and pairwise nuclear spins, and so on. This can be configured through `order` tag. In addition, the distance between the pairwise nuclear spins is defined via the connectivity distance ( $r_{\text{dipole}}$ ).

Furthermore, ab initio simulation results can also be included, such as the zero-field splitting (ZFS) and the quadrupole parameter. The  $\text{NV}^{-1}$  defect, with a spin state  $S = 1$ , has three electron spin triplet states:  $m_s = 0$  and  $m_s = \pm 1$ . Here,  $m_s = +1$  and  $m_s = -1$  are degenerate in the absence of a magnetic field, but they are separated from  $m_s = 0$ . This is a consequence of the spin-spin interaction. There are two ZFS parameters used to quantify that difference. The  $D$  parameter measures the separation between  $m_s = 0$  and  $m_s = \pm 1$ , while  $E$  parameter measures the separation between  $m_s = +1$  and  $m_s = -1$ . In cases where  $m_s = +1$  and  $m_s = -1$  are degenerate,  $E = 0$ . The ZFS can be computed using the VASP software through the `LDMATRIX` tag. Our calculations yield values of  $D = 2.952$  and  $E = 0$  GHz for  $\text{NV}^{-1}$ . These are in agreement with previous works, where  $D = 2.87$  and  $E = 0$  GHz are reported [71]. The quadrupole parameter can

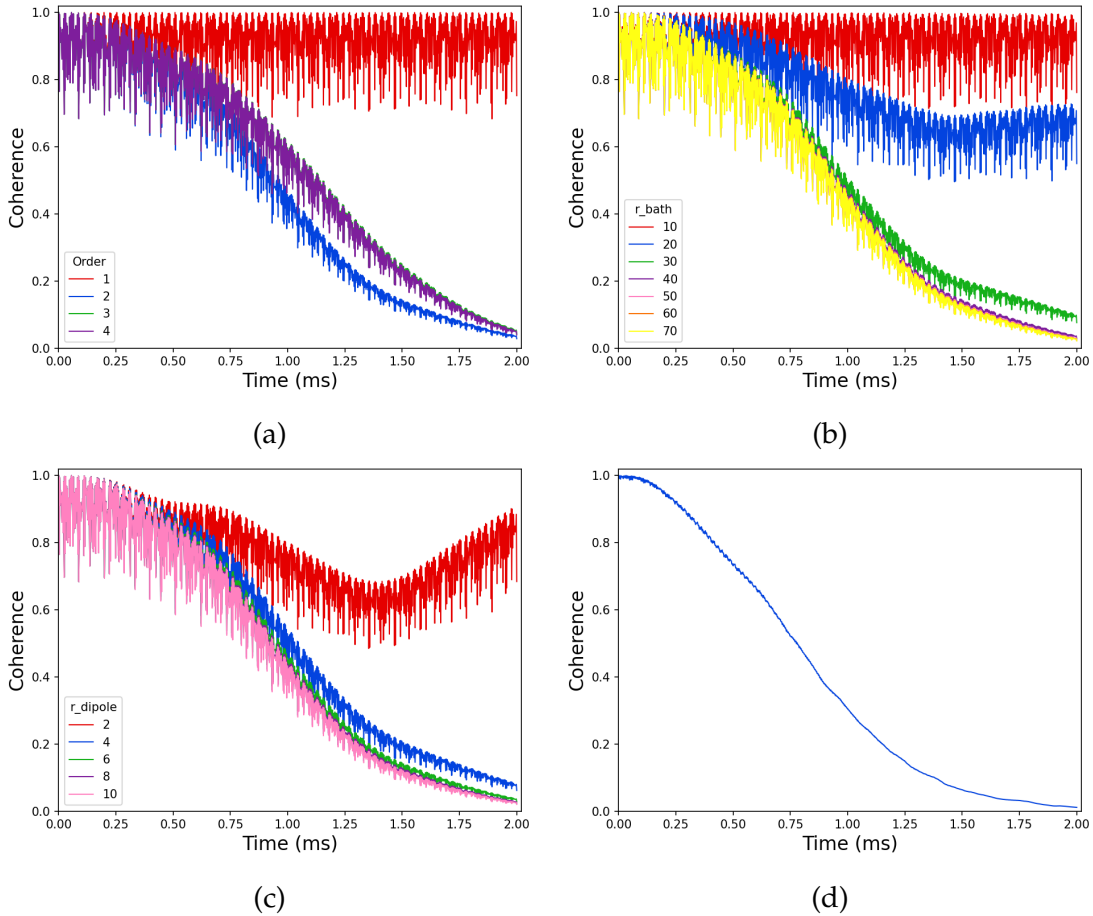


Figure 6.15: Convergence tests of the coherence curve with respect to the (a) approximation order (order), where CCE1, CCE2, CCE3 and CCE4 are included; (b) bath cutoff radius ( $r_{\text{bath}}$ ), the sizes are analyzed in a range from 10 to 70 Å; and (c) connectivity distance ( $r_{\text{dipole}}$ ), which is analyzed in a range from 2 to 10 Å. (d) Represents the decay of coherence for the central spin in the  $\text{NV}^{-1}$  defect in diamond at a magnetic field of 5000 G (5 T).

also be computed using the VASP software through the LEFG tag. However, the nuclear electric quadrupole moment ( $Q$ ) must be defined in advance. For the  $^{14}\text{N}$  isotope, which has a nuclear spin of  $I = 1$ ,  $Q = 20.44 \text{ mb}$  was used [72]. For the  $^{13}\text{C}$  isotope, a quadrupole moment of  $Q = 0$  was used due to its nuclear spin being  $I = 1/2$ . Thus, the quadrupole parameter calculated for the nitrogen atom is  $-7.196 \text{ MHz}$ . Here, our value computed with HSE06 functional is underestimated with respect to the other works ( $-5.01$  and  $-4.945 \text{ MHz}$ ) [73], [74]. However, our results will be used for next calculations.

**Fig. 6.15a** shows the convergence of the  $\text{NV}^{-}$  coherence time for different approximation orders for the CCE method. Orders such as CCE1, CCE2, CCE3 and CCE4 are included. This figure shows a convergence at second order (CCE2), which is in agreement with previous works [75], [76]. Note that the decay of coherence can be observed from the second order. **Fig. 6.15b** shows the convergence of the  $\text{NV}^{-}$  coherence time with respect to the bath cutoff radius,

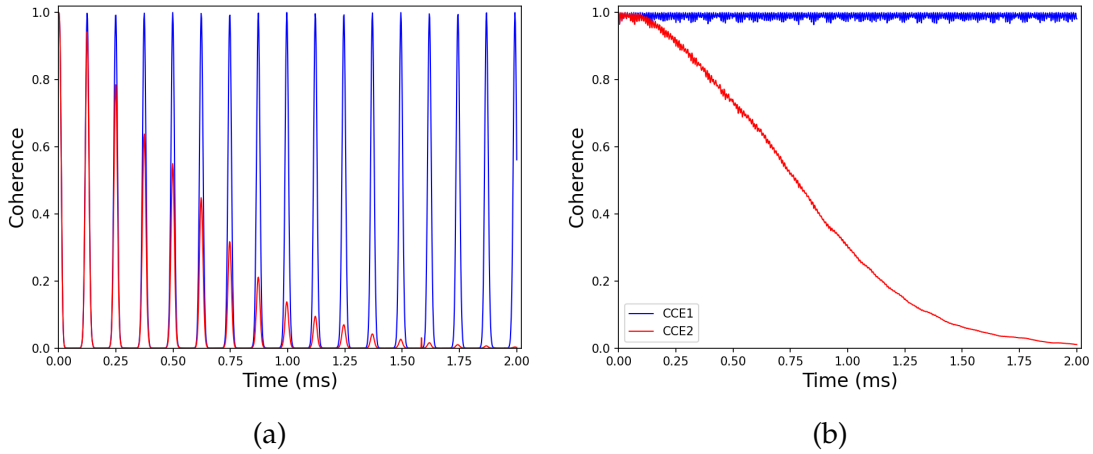


Figure 6.16: Analysis of the coherence function as magnetic field is varied: (a)  $B = 15$  G, and (b)  $B = 3000$  G. Both plots are generated using the CCE1 and CCE2 approximations.

where the sizes are analyzed in a range from 10 to 70 Å. The convergence results show that a bath cutoff radius of 40 Å is sufficient for our purposes. Finally, convergence with respect to the connectivity distance is shown in Fig. 6.15c. Here, a value of 6 Å has been selected.

Now that the initial parameters have been defined, we can continue with the main calculation. Fig. 6.15d shows the decay of coherence over time for the defect spin (central spin) in the  $NV^{-1}$  defect. The calculations were carried out using a Hahn-echo sequence and 100 different bath spin configurations to obtain an ensemble average. For the calculation of the coherence time  $T_2$ , the coherence function  $\mathcal{L}(t)$  was fit to a compressed exponential form:

$$\mathcal{L}(t) = \exp \left[ \left( -\frac{t}{T_2} \right)^n \right]. \quad (6.12)$$

The analysis yielded a coherence time of 0.916 ms at a magnetic field (B) of 5000 G (5 T). This value is in agreement with previous calculations, which report a  $T_2 = 0.97$  ms [76].

On the other hand, it is also interesting to examine the behavior of the coherence function as the magnetic field is varied from low to high strength. Here, two cases are shown in Fig. 6.16. At low strength, Fig. 6.16a is obtained for  $B = 15$  G using the CCE1 and CCE2 approximations. For CCE1 (blue), we can observe that the coherence function exhibits periodic behavior, which collapses and reemerges. However, CCE2 (red) also exhibits periodic behavior, but with a visible decay. In comparison, Fig. 6.16b shows curves at high strength ( $B = 3000$  G). The periodic behavior has been mitigated, and the decay of coherence in CCE2 is more evident. From both cases, we can conclude that single nuclear spins do not contribute significantly to the decoherence of the central spin. Thus, the pairwise interactions between nuclear spins are responsible of the decoherence. That is, CCE2 captures the decoherence information that arises from the interaction between the central spin and the spin bath.

# Chapter 7

## Concluding remarks

We have explored various promising point defects in c-BN as candidates for qubit platforms. Our guide for this exploration was the NV center in diamond. A study of its formation energy, spin state, energy levels and spin coherence has been presented. All our results have been satisfactorily corroborated with information from previous works, including the spin coherence study. Here, we report a coherence time of  $T_2 = 0.916$  ms.

In particular, four defects have been studied in depth in c-BN:  $N_B^{+1}$ ,  $(V_B - C_B)^0$ ,  $(V_B - V_N)^0$  and  $(V_B - Si_B)^0$ . All of them have shown thermodynamic stability near the mid-gap, thus exhibiting charge state transition levels far from both the valence and conduction bands. Although the formation energies are high for all defects under B-rich conditions, the situation is slightly more favorable under N-rich conditions. The  $(V_B - C_B)^0$  defect is the most favorable among all of them, as it has the lowest formation energy under N-rich conditions. In addition, the optical transitions for all the defects have been studied through their zero-phonon lines. Only the native defect  $N_B^{+1}$  showed characteristics to act as a color center, emitting a wavelength of 757 nm. This is important since the defect could potentially be enabled for applications such as quantum information, quantum sensing, and so on. On the other hand, the other three complex defects are also as interesting as the native defect. The three complex defects emit at telecom wavelengths. The  $(V_B - Si_B)^0$  defect has the shortest wavelength of 988 nm. Although this wavelength is only suitable for short-distance transmission using fiber-optic technology, it remains interesting for quantum technologies. The  $(V_B - V_N)^0$  defect has the largest wavelength of 1503 nm. This is the most interesting defect since the wavelength falls in the S-band, close to the C-band, which is widely used in communication applications. Finally, the  $(V_B - C_B)^0$  emits at a telecom wavelength of 1331 nm. This latter wavelength falls in the O-band, thus enabling quantum communication applications.

Unfortunately, the simulations to study the spin coherence in c-BN did not work as expected, and the reasons are unknown. Evidently, an aspect that must be worked on in the future is the spin coherence calculation for all our promising defects in c-BN. These calculations would be extremely important to determine the coherence times of each defect, which would help us demonstrate (in a complete manner) that they are promising defects for quantum technologies.

# Bibliography

- [1] G. Zhang, Y. Cheng, J.-P. Chou and A. Gali, ‘Material platforms for defect qubits and single-photon emitters,’ *Applied Physics Reviews*, vol. 7, no. 3, p. 031308, 2020.
- [2] ‘Qubits meet materials science,’ *Nature Reviews Materials*, vol. 6, no. 12, p. 869, 2021.
- [3] N. P. de Leon, K. M. Itoh, D. Kim *et al.*, ‘Materials challenges and opportunities for quantum computing hardware,’ *Science*, vol. 372, no. 6539, eabb2823, 2021.
- [4] L. Vines, E. Monakhov and A. Kuznetsov, ‘Defects in semiconductors,’ *Journal of Applied Physics*, vol. 132, no. 15, p. 150401, 2022.
- [5] A. Chatterjee, P. Stevenson, S. D. Franceschi, A. Morello, N. P. de Leon and F. Kuemmeth, ‘Semiconductor qubits in practice,’ *Nature Reviews Physics*, vol. 3, pp. 157–177, 2021.
- [6] G. Wolfowicz, F. J. Heremans, C. P. Anderson *et al.*, ‘Quantum guidelines for solid-state spin defects,’ *Nature Reviews Materials*, vol. 6, pp. 906–925, 2021.
- [7] C. E. Dreyer, A. Alkauskas, J. L. Lyons, A. Janotti and C. G. Van de Walle, ‘First-principles calculations of point defects for quantum technologies,’ *Annual Review of Materials Research*, vol. 48, no. Volume 48, pp. 1–26, 2018.
- [8] C. Freysoldt, B. Grabowski, T. Hickel *et al.*, ‘First-principles calculations for point defects in solids,’ *Rev. Mod. Phys.*, vol. 86, no. 1, pp. 253–305, 2014.
- [9] Á. Gali, ‘Recent advances in the ab initio theory of solid-state defect qubits,’ *Nanophotonics*, vol. 12, no. 3, pp. 359–397, 2023.
- [10] V. Ivády, I. A. Abrikosov and A. Gali, ‘First principles calculation of spin-related quantities for point defect qubit research,’ *npj Computational Materials*, vol. 4, no. 1, p. 76, 2018.
- [11] G. Kresse and J. Hafner, ‘Ab initio molecular dynamics for liquid metals,’ *Phys. Rev. B*, vol. 47, no. 1, pp. 558–561, 1993.
- [12] G. Kresse and J. Hafner, ‘Ab initio molecular-dynamics simulation of the liquid-metal–amorphous–semiconductor transition in germanium,’ *Phys. Rev. B*, vol. 49, no. 20, pp. 14251–14269, 1994.

- [13] G. Kresse and J. Furthmüller, ‘Efficiency of ab-initio total energy calculations for metals and semiconductors using a plane-wave basis set,’ *Computational Materials Science*, vol. 6, no. 1, pp. 15–50, 1996.
- [14] G. Kresse and J. Furthmüller, ‘Efficient iterative schemes for ab initio total-energy calculations using a plane-wave basis set,’ *Phys. Rev. B*, vol. 54, no. 16, pp. 11 169–11 186, 1996.
- [15] G. Kresse and J. Hafner, ‘Norm-conserving and ultrasoft pseudopotentials for first-row and transition elements,’ *Journal of Physics: Condensed Matter*, vol. 6, no. 40, p. 8245, 1994.
- [16] G. Kresse and D. Joubert, ‘From ultrasoft pseudopotentials to the projector augmented-wave method,’ *Phys. Rev. B*, vol. 59, no. 3, pp. 1758–1775, 1999.
- [17] J. P. Perdew, K. Burke and M. Ernzerhof, ‘Generalized gradient approximation made simple,’ *Physical Review Letters*, vol. 77, no. 18, pp. 3865–3868, 1996.
- [18] J. Heyd, G. E. Scuseria and M. Ernzerhof, ‘Hybrid functionals based on a screened coulomb potential,’ *The Journal of Chemical Physics*, vol. 118, no. 18, pp. 8207–8215, 2003.
- [19] M. Onizhuk and G. Galli, ‘Pycce: A python package for cluster correlation expansion simulations of spin qubit dynamics,’ *Advanced Theory and Simulations*, vol. 4, no. 11, p. 2 100 254, 2021.
- [20] N. W. Ashcroft and N. D. Mermin, *Solid State Physics*. Philadelphia: Saunders College, 1976, ch. 7.
- [21] S. H. Simon, *The Oxford Solid State Basics*. Oxford University Press, 2013, p. 122.
- [22] C. Kittel, *Introduction to Solid State Physics*, 8th ed. Wiley, 2005.
- [23] E. Wigner and F. Seitz, ‘On the constitution of metallic sodium,’ *Phys. Rev.*, vol. 43, no. 10, pp. 804–810, 1933.
- [24] L. Brillouin, ‘Les électrons libres dans les métaux et le rôle des réflexions de Bragg,’ *J. Phys. Radium*, vol. 1, no. 11, pp. 377–400, 1930.
- [25] P. Hofmann, *Solid State Physics: An Introduction*, 3rd ed. Wiley-VCH, 2022.
- [26] P. Y. Yu and M. Cardona, *Fundamentals of Semiconductors: Physics and Materials Properties*, 4th. Springer, 2010.
- [27] H. Ibach and H. Lüth, *Solid-State Physics: An Introduction to Principles of Materials Science*, 4th ed. Springer, 2009.
- [28] E. Kaxiras, *Atomic and Electronic Structure of Solids*. Cambridge University Press, 2003.
- [29] X. Gonze and C. Lee, ‘Dynamical matrices, born effective charges, dielectric permittivity tensors, and interatomic force constants from density-functional perturbation theory,’ *Phys. Rev. B*, vol. 55, no. 16, pp. 10 355–10 368, 1997.

- [30] R. M. Pick, M. H. Cohen and R. M. Martin, 'Microscopic theory of force constants in the adiabatic approximation,' *Phys. Rev. B*, vol. 1, no. 2, pp. 910–920, 1970.
- [31] S. M. Sze and K. K. Ng, *Physics of Semiconductor Devices*, 3rd ed. Wiley, 2007.
- [32] P. A. Burr, M. J. Rushton, A. Chroneos and R. W. Grimes, '1.02 - fundamental point defect properties in ceramics,' in *Comprehensive Nuclear Materials*, Second Edition, Elsevier, 2020, pp. 50–73.
- [33] J. R. Weber, W. F. Koehl, J. B. Varley *et al.*, 'Quantum computing with defects,' *Proceedings of the National Academy of Sciences*, vol. 107, no. 19, pp. 8513–8518, 2010.
- [34] L. Gordon, J. R. Weber, J. B. Varley, A. Janotti, D. D. Awschalom and C. G. Van de Walle, 'Quantum computing with defects,' *MRS Bulletin*, vol. 38, no. 10, pp. 802–807, 2013.
- [35] O. L. Hebnes, M. E. Bathen, Ø. S. Schøyen, S. G. W. Larsen, L. Vines and M. Hjorth-Jensen, 'Predicting solid state material platforms for quantum technologies,' *npj Computational Materials*, vol. 8, no. 207, 2022.
- [36] K. Momma and F. Izumi, 'Vesta 3 for three-dimensional visualization of crystal, volumetric and morphology data,' *Journal of Applied Crystallography*, vol. 44, no. 6, pp. 1272–1276, 2011.
- [37] A. F. Goncharov, J. C. Crowhurst, J. K. Dewhurst *et al.*, 'Thermal equation of state of cubic boron nitride: Implications for a high-temperature pressure scale,' *Phys. Rev. B*, vol. 75, no. 22, p. 224114, 2007.
- [38] D. Evans, A. McGlynn, B. Towlson *et al.*, 'Growth of diamond on high-power electronic material,' *Journal of Physics: Condensed Matter*, vol. 20, no. 7, 2008.
- [39] W. Setyawan and S. Curtarolo, 'Computational materials science: From ab initio to monte carlo,' *Computational Materials Science*, vol. 49, no. 2, pp. 299–312, 2010.
- [40] W. Nolting, *Theoretical Physics 9: Fundamentals of Many-body Physics*. Berlin, Germany: Springer Link, 2018.
- [41] M. Born and R. Oppenheimer, 'Zur quantentheorie der moleküle,' *Annalen der Physik*, 1927.
- [42] D. R. Hartree, *The Wave Mechanics of an Atom with a Non-Coulomb Central Field. Part I. Theory and Methods*. Cambridge University Press, 1928.
- [43] D. R. Hartree, *The Wave Mechanics of an Atom with a Non-Coulomb Central Field. Part II. Some Results and Discussion*. Cambridge University Press, 1928.
- [44] V. Fock, 'Näherungsmethode zur lösung des quantenmechanischen mehrkörperproblems,' *Z. Physik*, 1930.
- [45] J. C. Slater, 'The theory of complex spectra,' *Physical Review*, 1929.
- [46] W. Pauli, 'Über den zusammenhang des abschlusses der elektronengruppen im atom mit der komplexstruktur der spektren,' *Z. Physik*, 1925.

- [47] P. Hohenberg and W. Kohn, ‘Inhomogeneous electron gas,’ *Physical Review*, vol. 136, no. 3B, B864–B871, 1964.
- [48] W. Kohn and L. J. Sham, ‘Self-Consistent Equations Including Exchange and Correlation Effects,’ *Physical Review*, vol. 140, no. 4A, A1133–A1138, 1965.
- [49] D. S. Sholl and J. A. Steckel, *Density Functional Theory: A Practical Introduction*. John Wiley & Sons, Inc., 2009.
- [50] H. J. Monkhorst and J. D. Pack, ‘Special points for brillouin-zone integrations,’ *Phys. Rev. B*, vol. 13, no. 12, pp. 5188–5192, 1976.
- [51] C. Freysoldt, J. Neugebauer and C. G. Van de Walle, ‘Fully ab initio finite-size corrections for charged-defect supercell calculations,’ *Phys. Rev. Lett.*, vol. 102, no. 1, p. 016 402, 2009.
- [52] Y. Kumagai and F. Oba, ‘Electrostatics-based finite-size corrections for first-principles point defect calculations,’ *Physical Review B*, vol. 89, no. 19, p. 195 205, 2014.
- [53] A. Gali, E. Janzén, P. Deák, G. Kresse and E. Kaxiras, ‘Theory of spin-conserving excitation of the  $N - V^-$  center in diamond,’ *Phys. Rev. Lett.*, vol. 103, no. 18, p. 186 404, 2009.
- [54] W. Yang and R.-B. Liu, ‘Quantum many-body theory of qubit decoherence in a finite-size spin bath,’ *Phys. Rev. B*, vol. 78, no. 8, p. 085 315, 2008.
- [55] T. Hom, W. Kiszenick and B. Post, ‘Accurate lattice constants from multiple reflection measurements. ii. lattice constants of germanium, silicon, and diamond,’ *Journal of Applied Crystallography*, vol. 8, no. 4, pp. 457–458, 1975.
- [56] C. D. Clark, P. J. Dean and P. V. Harris, ‘Intrinsic edge absorption in diamond,’ *Proceedings of the Royal Society of London. Series A, Mathematical and Physical Sciences*, vol. 277, pp. 312–329, 1964.
- [57] M. S. Barson, E. Krausz, N. B. Manson and M. W. Doherty, ‘The fine structure of the neutral nitrogen-vacancy center in diamond,’ *Nanophotonics*, vol. 8, no. 11, pp. 1985–1991, 2019.
- [58] A. Alkauskas, B. B. Buckley, D. D. Awschalom and C. G. V. de Walle, ‘First-principles theory of the luminescence lineshape for the triplet transition in diamond nv centres,’ *New Journal of Physics*, vol. 16, no. 7, p. 073 026, 2014.
- [59] M. W. Doherty, N. B. Manson, P. Delaney, F. Jelezko, J. Wrachtrup and L. C. Hollenberg, ‘The nitrogen-vacancy colour centre in diamond,’ *Physics Reports*, vol. 528, no. 1, pp. 1–45, 2013.
- [60] A. Agui, S. Shin, M. Fujisawa *et al.*, ‘Resonant soft-x-ray emission study in relation to the band structure of cbn,’ *Phys. Rev. B*, vol. 55, no. 4, pp. 2073–2078, 1997.
- [61] J. E. Moussa, P. A. Schultz and J. R. Chelikowsky, ‘Analysis of the heyd-scuseria-ernzerhof density functional parameter space,’ *The Journal of Chemical Physics*, vol. 136, no. 20, p. 204 117, 2012.

- [62] A. Karolewski, L. Kronik and S. Kümmel, 'Using optimally tuned range separated hybrid functionals in ground-state calculations: Consequences and caveats,' *The Journal of Chemical Physics*, vol. 138, no. 20, p. 204115, 2013.
- [63] G. Will and B. Kiefer, 'Electron deformation density in rhombohedral  $\alpha$ -boron,' *Zeitschrift für anorganische und allgemeine Chemie*, vol. 627, no. 9, pp. 2100–2104, 2001.
- [64] F. H. Horn, 'Some electrical and optical properties of simple rhombohedral boron,' *Journal of Applied Physics*, vol. 30, no. 10, pp. 1611–1612, 1959.
- [65] W. Orellana and H. Chacham, 'Atomic geometry and energetics of vacancies and antisites in cubic boron nitride,' *Applied Physics Letters*, vol. 74, no. 20, pp. 2984–2986, 1999.
- [66] W. Orellana and H. Chacham, 'Energetics of carbon and oxygen impurities and their interaction with vacancies in cubic boron nitride,' *Phys. Rev. B*, vol. 62, no. 15, pp. 10135–10141, 2000.
- [67] Y. Gai and G. Tang, 'First-principles study of native and extrinsic point defects in cubic boron nitride,' *Physica Scripta*, vol. 83, no. 4, p. 045605, 2011.
- [68] M. E. Turiansky, D. Wickramaratne, J. L. Lyons and C. G. Van de Walle, 'Prospects for n-type conductivity in cubic boron nitride,' *Applied Physics Letters*, vol. 119, no. 16, p. 162105, 2021.
- [69] N. L. Nguyen, H. T. Dang, T. L. Pham and T. M. H. Nghiem, *Computationally predicted electronic properties and energetics of native defects in cubic boron nitride*, 2024. arXiv: 2402.08464 [cond-mat.mtrl-sci].
- [70] M. E. Turiansky and C. G. V. de Walle, 'Telecom-wavelength nv-center analogs in cubic boron nitride,' *Phys. Rev. B*, vol. 108, no. L041102, 2023.
- [71] Y. Yang, H. H. Vallabhapurapu, V. K. Sewani *et al.*, 'Observing hyperfine interactions of NV<sup>−</sup> centers in diamond in an advanced quantum teaching lab,' *American Journal of Physics*, vol. 90, no. 7, pp. 550–560, 2022.
- [72] N. Stone, 'Table of nuclear electric quadrupole moments,' *Atomic Data and Nuclear Data Tables*, vol. 111-112, pp. 1–28, 2016.
- [73] S. Felton, A. M. Edmonds, M. E. Newton *et al.*, 'Hyperfine interaction in the ground state of the negatively charged nitrogen vacancy center in diamond,' *Phys. Rev. B*, vol. 79, no. 7, p. 075203, 2009.
- [74] B. Smeltzer, J. McIntyre and L. Childress, 'Robust control of individual nuclear spins in diamond,' *Phys. Rev. A*, vol. 80, no. 5, p. 050302, 2009.
- [75] N. Zhao, S.-W. Ho and R.-B. Liu, 'Decoherence and dynamical decoupling control of nitrogen vacancy center electron spins in nuclear spin baths,' *Phys. Rev. B*, vol. 85, no. 11, p. 115303, 2012.
- [76] S. Kanai, F. J. Heremans, H. Seo *et al.*, 'Generalized scaling of spin qubit coherence in over 12,000 host materials,' *Proceedings of the National Academy of Sciences*, vol. 119, no. 15, e2121808119, 2022.

# Appendix A

## Convergence Tests

Table A.1: Detailed information on the total energies and relative energies for each energy cutoff. An energy cutoff of 500 eV was chosen for c-BN under a convergence criterion of 1 meV (gray shaded area).

ENCUT (eV)	$E_{prist}$ (eV)	$E_{dec}$ (eV)	$E_{inc}$ (eV)	$E_{dec}^{rel}$ (meV)	$E_{inc}^{rel}$ (meV)
200	-17.002	-16.938	-17.042	64.629	39.184
250	-17.525	-17.520	-17.538	4.624	13.704
300	-17.470	-17.462	-17.461	7.842	9.118
350	-17.426	-17.417	-17.416	8.942	10.197
400	-17.449	-17.447	-17.441	2.190	8.284
450	-17.454	-17.448	-17.445	5.954	9.034
500	-17.451	-17.446	-17.442	5.769	9.279
550	-17.452	-17.446	-17.442	5.677	9.308
600	-17.455	-17.449	-17.445	5.652	9.500
650	-17.457	-17.451	-17.447	5.559	9.565
700	-17.458	-17.453	-17.449	5.539	9.511
750	-17.459	-17.454	-17.450	5.586	9.455
800	-17.460	-17.454	-17.450	5.631	9.406
850	-17.460	-17.454	-17.451	5.657	9.401
900	-17.460	-17.454	-17.451	5.660	9.401
950	-17.460	-17.454	-17.451	5.661	9.397

Table A.2: Detailed information on  $\mathbf{k}$ -density convergence for c-BN. A  $\mathbf{k}$ -density of 4 was chosen under a convergence criterion of 1 meV (gray shaded area).

$\mathbf{k}$ -density ( $1/\text{\AA}^3$ )	$E_{prist}$ (eV)	$E_{dec}$ (eV)	$E_{inc}$ (eV)	$E_{dec}^{rel}$ (meV)	$E_{inc}^{rel}$ (meV)
2	-17.435	-17.429	-17.426	6.080	8.964
3	-17.451	-17.445	-17.442	5.818	9.243
4	-17.451	-17.446	-17.442	5.769	9.279
5	-17.451	-17.446	-17.442	5.784	9.264
6	-17.451	-17.446	-17.442	5.789	9.255
7	-17.451	-17.446	-17.442	5.792	9.262
8	-17.451	-17.446	-17.442	5.789	9.260
9	-17.451	-17.446	-17.442	5.788	9.264

Table A.3: Detailed information on the  $\mathbf{k}$ -density convergence for rhombohedral  $\alpha$ -boron. A  $\mathbf{k}$ -density of 4 was chosen under a convergence criterion of 1 meV (gray shaded area).

$\mathbf{k}$ -density ( $1/\text{\AA}^3$ )	$E_{prist}$ (eV)	$E_{dec}$ (eV)	$E_{inc}$ (eV)	$E_{dec}^{rel}$ (meV)	$E_{inc}^{rel}$ (meV)
2	-80.492	-80.476	-80.490	16.244	2.446
3	-80.428	-80.411	-80.426	16.331	2.071
4	-80.434	-80.420	-80.435	16.347	2.052
5	-80.438	-80.421	-80.436	16.347	2.072
6	-80.438	-80.421	-80.436	16.337	2.083
7	-80.438	-80.421	-80.436	16.352	2.077
8	-80.438	-80.421	-80.436	16.344	2.071
9	-80.438	-80.421	-80.436	16.338	2.067

Table A.4: Detailed information on the energy cutoff convergence for rhombohedral  $\alpha$ -boron. An energy cutoff of 450 eV was chosen under a convergence criterion of 1 meV (gray shaded area).

ENCUT (eV)	$E_{prist}$ (eV)	$E_{dec}$ (eV)	$E_{inc}$ (eV)	$E_{dec}^{rel}$ (meV)	$E_{inc}^{rel}$ (meV)
200	-78.670	-78.621	-78.696	48.894	26.711
250	-79.860	-79.854	-79.849	5.499	10.863
300	-80.254	-80.240	-80.254	14.492	0.002
350	-80.419	-80.402	-80.417	17.112	1.691
400	-80.437	-80.421	-80.435	16.360	1.977
450	-80.436	-80.420	-80.434	16.347	2.052
500	-80.440	-80.424	-80.438	16.069	2.342
550	-80.446	-80.430	-80.444	15.909	2.419
600	-80.453	-80.437	-80.451	15.910	2.398
650	-80.459	-80.443	-80.457	15.904	2.468
700	-80.463	-80.447	-80.461	15.875	2.499
750	-80.465	-80.449	-80.462	15.852	2.547
800	-80.465	-80.449	-80.463	15.809	2.571
850	-80.465	-80.449	-80.463	15.798	2.582
900	-80.465	-80.450	-80.463	15.786	2.594
950	-80.466	-80.450	-80.463	15.792	2.595

Table A.5: Detailed information on the energy cutoff convergence for nitrogen gas. An energy cutoff of 500 eV was chosen under a convergence criterion of 1 meV (gray shaded area).

ENCUT (eV)	$E_{prist}$ (eV)	$E_{dec}$ (eV)	$E_{inc}$ (eV)	$E_{dec}^{rel}$ (meV)	$E_{inc}^{rel}$ (meV)
200	-17.256	-17.232	-17.220	24.007	36.236
250	-16.647	-16.630	-16.649	17.302	1.475
300	-16.495	-16.487	-16.499	7.792	4.353
350	-16.519	-16.510	-16.523	8.859	3.565
400	-16.591	-16.584	-16.595	6.846	3.997
450	-16.615	-16.610	-16.619	4.469	4.218
500	-16.623	-16.619	-16.627	4.352	3.549
550	-16.629	-16.624	-16.632	4.182	3.316
600	-16.633	-16.629	-16.636	4.053	3.187
650	-16.637	-16.633	-16.640	3.991	3.191
700	-16.639	-16.635	-16.642	3.958	3.152
750	-16.640	-16.636	-16.643	3.907	3.165
800	-16.641	-16.637	-16.644	3.927	3.122
850	-16.641	-16.637	-16.644	3.920	3.124
900	-16.641	-16.637	-16.644	3.898	3.111
950	-16.642	-16.638	-16.645	3.885	3.102

Table A.6: Detailed information on the  $\mathbf{k}$ -density convergence for nitrogen gas. The data confirm that the  $\Gamma$  point is sufficient (gray shaded area).

$\mathbf{k}$ -density ( $1/\text{\AA}^3$ )	$E_{prist}$ (eV)	$E_{dec}$ (eV)	$E_{inc}$ (eV)	$E_{dec}^{rel}$ (meV)	$E_{inc}^{rel}$ (meV)
1	-16.623	-16.619	-16.627	4.018	3.398
2	-16.623	-16.619	-16.627	4.468	3.569
4	-16.623	-16.619	-16.627	4.352	3.549
5	-16.623	-16.619	-16.627	4.320	3.567
7	-16.623	-16.619	-16.627	4.326	3.516
8	-16.623	-16.619	-16.627	4.339	3.531

# Appendix B

## Local Density of States

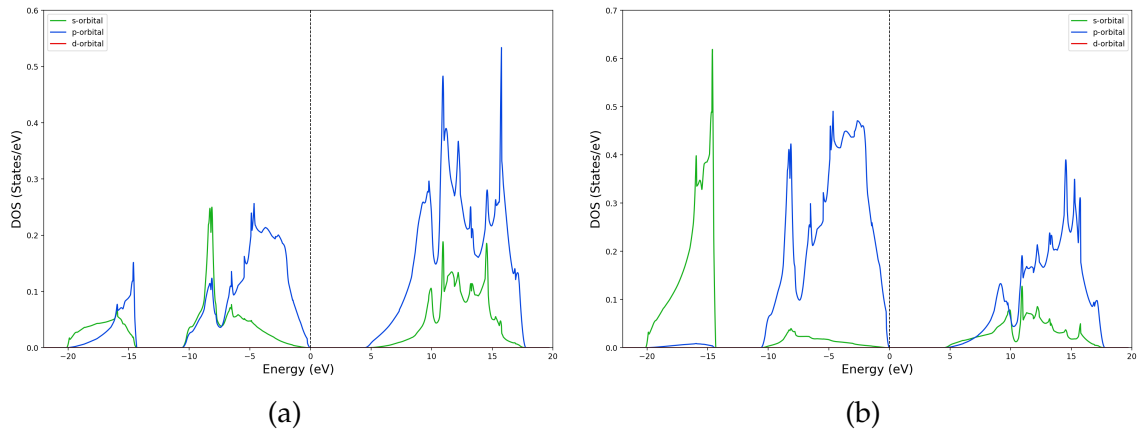


Figure B.1: Local DOS for (a) Boron and (b) Nitrogen in c-BN using the PBE method.

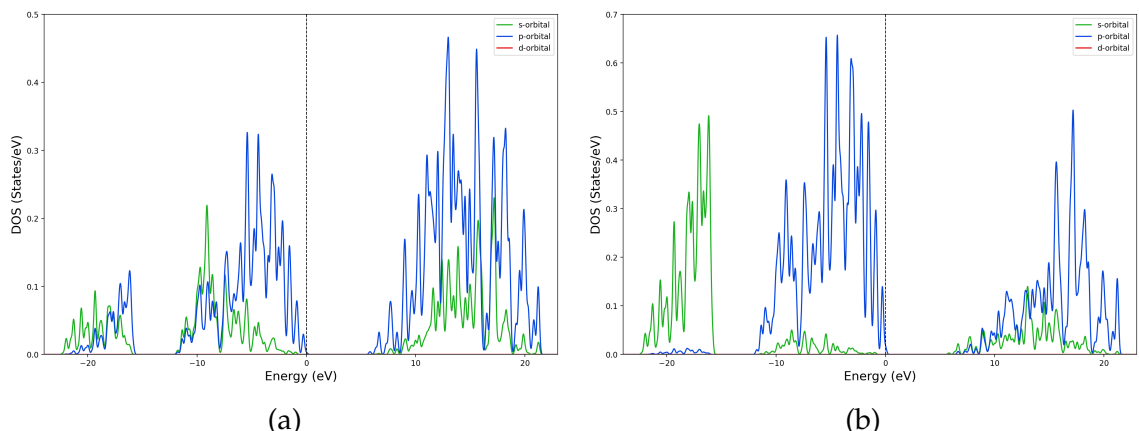


Figure B.2: Local DOS for (a) Boron and (b) Nitrogen in c-BN using the HSE06 method.

## Appendix C

# Analyzing the Fraction of Exact Hartree-Fock Exchange

Table C.1: Results for the lattice constant and band gap in c-BN, when the fraction of the exact Hartree-Fock exchange ( $\alpha$ ) is varied from 0 to 1. The screening parameter was kept at its default value of  $\omega = 0.2$ . The default parameter of HSE06 was used (gray shaded area). Band structure diagrams can be found in Fig. C.1.

$\alpha$	Lattice constant (Å)	Band gap (eV)
0.0	3.626	4.450
0.1	3.614	4.988
0.25	3.598	5.814
0.33	3.590	6.263
0.5	3.574	7.236
0.7	3.556	8.410
1.0	3.599	10.719

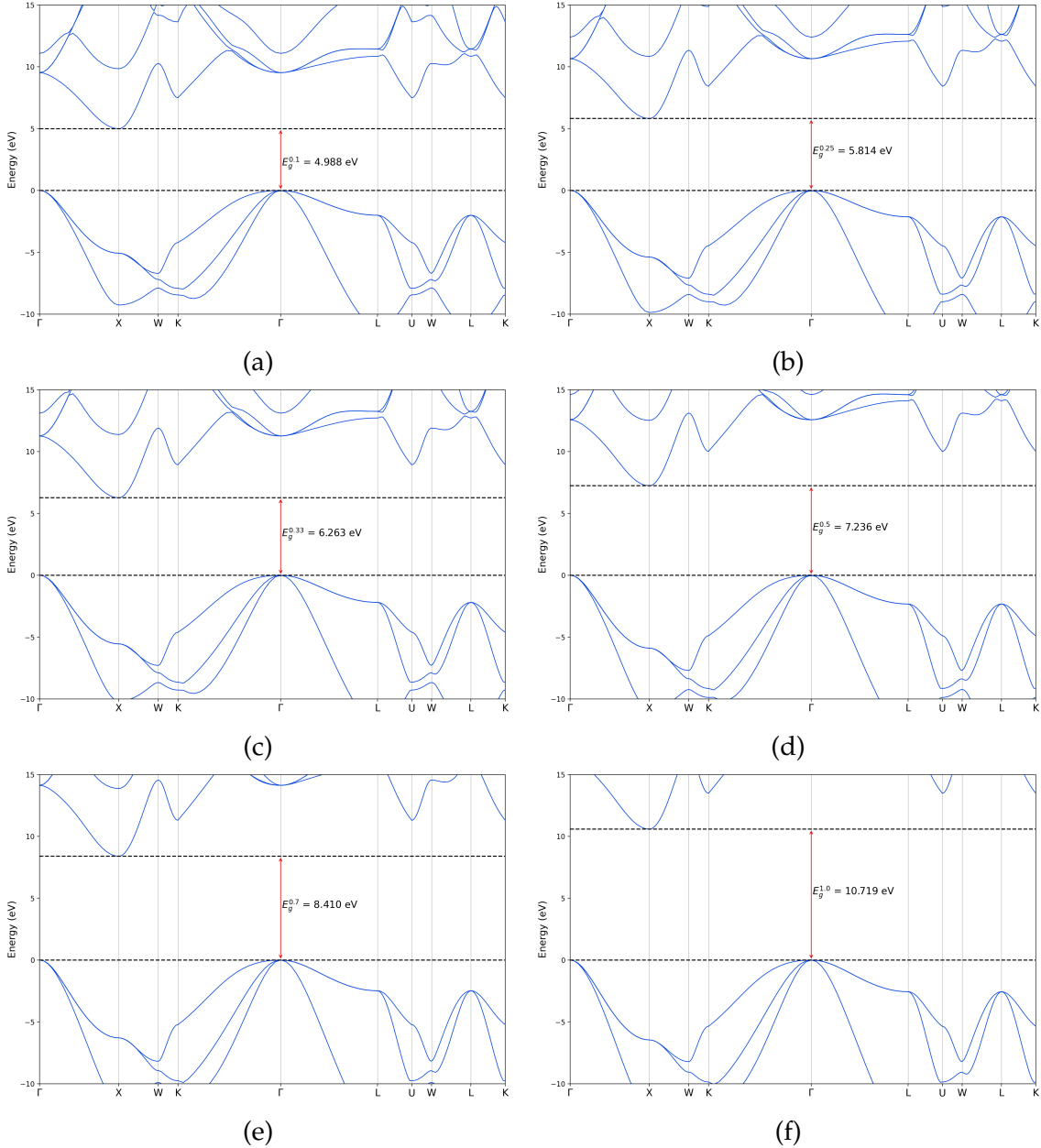


Figure C.1: Band structure for various  $\alpha$  in c-BN, where (a)  $\alpha = 0.1$ , (b)  $\alpha = 0.25$ , (c)  $\alpha = 0.33$ , (d)  $\alpha = 0.5$ , (e)  $\alpha = 0.7$  and (f)  $\alpha = 1.0$ .

# Appendix D

## NV center in Diamond

Table D.1: Values for the terms of the Eqs. 4.26 and 4.29, which allow plotting the formation energy diagram for the NV center in diamond using PBE method. Here,  $E_{perf} = -1961.920$  eV and  $E_{VBM} = 9.646$  eV.

$q$	$E_{def}^q$ (eV)	$E_{corr}$ (meV)	$\xi_{form}^q$ (eV)
-2	-1922.237	1323	10.526
-1	-1934.981	379	7.428
0	-1946.197	0	5.858
+1	-1957.045	152	4.656
+2	-1966.929	743	4.418

Table D.2: Energies for each level within the band gap for the  $NV^0$  defect using HSE06 method. The table includes information for both channels and their band indexes. An asterisk indicate the level is occupied.

States	Band index	Energy (eV)	
		Spin up	Spin down
$a_1$	430	0.185 (*)	0.305 (*)
$e_x$	431	0.776 (*)	2.934
$e_y$	432	3.199	4.046

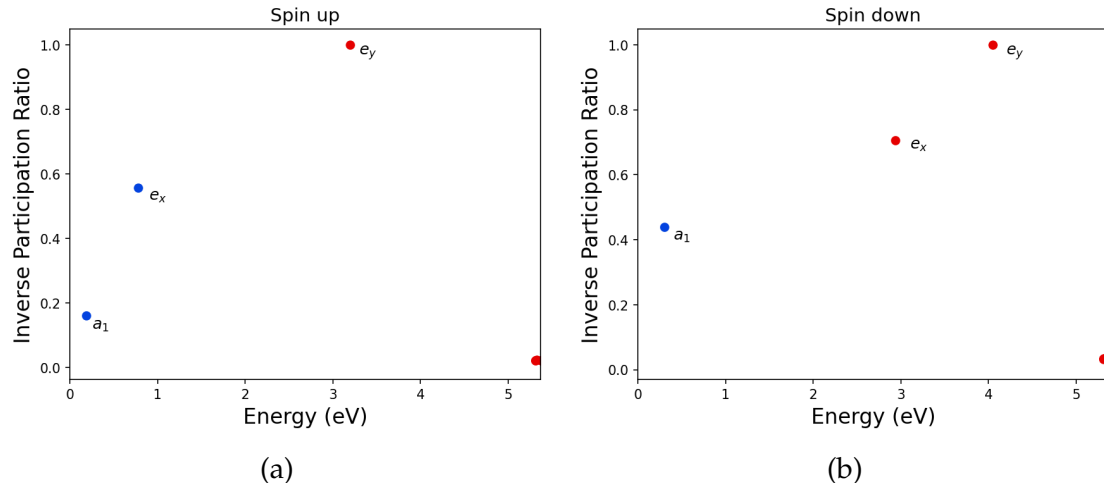


Figure D.1: IPR for the  $NV^0$  defect in diamond using the HSE06 method: (a) Spin up channel and (b) Spin down channel. The occupied electronic states are represent by blue balls, while the unoccupied states are represent by red balls. The energy range goes from 0 to  $E_g = 5.369$  eV.

# Appendix E

## Point defects in c-BN

Table E.1: Values for the terms of the **Eqs. 4.26** and **4.29**, which allow plotting the formation energy diagram for native defects. Here,  $E_{perf} = -1884.741$  eV and  $E_{VBM} = 7.295$  eV using PBE method.

Defect	$q$	$E_{def}^q$ (eV)	$E_{corr}$ (meV)	$\xi_{form}^q$ [B-rich] (eV)	$\xi_{form}^q$ [N-rich] (eV)
$V_B$	-4	-1832.258	3890	16.602	14.170
	-3	-1844.376	2458	11.778	9.346
	-2	-1853.359	1156	10.090	7.658
	-1	-1861.997	334	8.747	6.315
	0	-1870.307	0	7.731	5.299
$N_B$	+1	-1877.520	88	7.813	5.381
	-3	-1840.783	1936	26.120	21.256
	-2	-1852.828	912	21.370	16.506
	-1	-1864.837	247	16.655	11.791
	0	-1876.293	0	12.494	7.630
	+1	-1885.828	259	10.253	5.389
	+2	-1895.477	1033	7.898	3.034

Table E.2: Values for the terms of the Eqs. 4.26 and 4.29, which allow plotting the formation energy diagram for complex defects. Here,  $E_{perf} = -1884.741$  eV and  $E_{VBM} = 7.295$  eV using PBE method.

Defect	$q$	$E_{def}^q$ (eV)	$E_{corr}$ (meV)	$\xi_{form}^q$ [B-rich] (eV)	$\xi_{form}^q$ [N-rich] (eV)
$V_B - V_N$	-3	-1830.212	2458	15.193	15.193
	-2	-1842.174	1250	10.526	10.526
	-1	-1850.950	388	9.045	9.045
	0	-1859.307	0	7.982	7.982
	+1	-1867.802	76	6.782	6.782
	+2	-1876.107	627	5.772	5.772
	+3	-1883.296	1488	5.877	5.877
$V_B - C_B$	-3	-1840.809	2092	17.735	12.872
	-2	-1852.942	1062	12.896	8.033
	-1	-1861.844	302	11.289	6.426
	0	-1870.328	0	10.100	5.237
	+1	-1878.20	159	9.522	4.659
	+2	-1885.366	646	9.651	4.788
	-3	-1838.393	1858	16.478	11.615
$V_B - Si_B$	-2	-1850.569	900	11.597	6.734
	-1	-1859.500	225	9.960	5.097
	0	-1868.037	0	8.718	3.855
	+1	-1875.932	239	8.117	3.254
	+2	-1883.169	802	8.175	3.312

Table E.3: Values for the terms of the Eqs. 4.26 and 4.29, which allow plotting the formation energy diagram for native defects. Here,  $E_{perf} = -2199.238$  eV and  $E_{VBM} = 6.706$  eV using HSE06 method.

Defect	$q$	$E_{def}^q$ (eV)	$E_{corr}$ (meV)	$\xi_{form}^q$ [B-rich] (eV)	$\xi_{form}^q$ [N-rich] (eV)
$V_B$	-4	-2144.631	4006	20.359	17.660
	-3	-2156.908	2532	14.787	12.088
	-2	-2165.694	1187	12.707	10.008
	-1	-2174.505	338	10.601	7.902
	0	-2183.347	0	8.465	5.766
	+1	-2190.113	81	8.405	5.766
$N_B$	-3	-2154.780	2246	29.854	24.456
	-2	-2166.945	1022	24.395	18.997
	-1	-2178.889	256	19.157	13.759
	0	-2190.500	0	14.251	8.853
	+1	-2200.669	270	10.788	5.390
	+2	-2211.088	1067	7.075	1.677

Table E.4: Values for the terms of the Eqs. 4.26 and 4.29, which allow plotting the formation energy diagram for complex defects. Here,  $E_{perf} = -2199.238$  eV and  $E_{VBM} = 6.706$  eV using HSE06 method.

Defect	$q$	$E_{def}^q$ (eV)	$E_{corr}$ (meV)	$\xi_{form}^q$ [B-rich] (eV)	$\xi_{form}^q$ [N-rich] (eV)
	-3	-2140.542	2415	18.214	18.214
	-2	-2152.783	1278	12.679	12.679
	-1	-2161.405	393	10.763	10.763
$V_B - V_N$	0	-2170.127	0	8.747	8.747
	+1	-2178.561	98	7.018	7.018
	+2	-2187.258	672	5.027	5.027
	+3	-2194.133	1719	4.857	4.857
	-3	-2153.994	2135	20.821	15.423
	-2	-2166.263	1083	15.259	9.861
$V_B - C_B$	-1	-2175.172	320	13.055	7.657
	0	-2183.891	0	11.041	5.643
	+1	-2191.970	177	9.668	4.270
	+2	-2198.744	658	9.600	4.202
	-3	-2151.173	1902	19.386	13.988
	-2	-2163.477	919	13.788	8.390
$V_B - Si_B$	-1	-2172.494	236	11.476	6.077
	0	-2181.164	0	9.512	4.113
	+1	-2189.289	262	8.093	2.694
	+2	-2196.127	826	7.960	2.561

# List of Figures

2.1	Relation between the basis (green ball), the Bravais lattice (set of black points) and crystal (set of green balls). . . . .	5
2.2	(a) 2D representation of primitive and conventional cells in a hexagonal lattice. The cells with blue and red edges are primitive cells, with only the latter being a Wigner-Seitz cell. The cells with green and yellow edges are conventional cells. (b) Primitive and conventional cells of an FCC lattice. The primitive cell is represented with dashed lines and shaded in gray. The conventional cell has a cubic shape and is outlined with solid lines.	6
2.3	(a) Brillouin zones in a hexagonal lattice in 2D: the first zone is shaded in red, the second in yellow, the third in orange, the fourth in green, and finally, the fifth in blue. (b) 1BZ of an FCC lattice in 3D is a truncated octahedron, shaded in red. . . . .	8
2.4	Periodic potential in a one-dimensional lattice. The black balls depict the ions. . . . .	9
2.5	(a) Representation of optical and acoustic phonon branches for a 1D diatomic chain. (b) The primitive cell of diamond has 2 atoms, so its phonon dispersion relation is expected to show 6 branches. .	13
2.6	The phonon dispersion relation for cubic boron nitride is shown in both cases: without NAC and with NAC. At the $\Gamma$ -point, the LO-TO splitting can be observed due to the long-range Coulomb interactions in polar materials. . . . .	14
2.7	Energy level diagrams for different types of materials. . . . .	15
2.8	Parabolic Band Approximation for semiconductors (a) In a direct band gap semiconductor, the maximum of the valence band and the minimum of the conduction band occur at the same crystal momentum ( $\mathbf{k}$ ). (b) In an indirect band gap semiconductor, the transition occurs at different crystal momenta, with the maximum of the valence band and the minimum of the conduction band located at distinct ( $\mathbf{k}$ ) values . . . . .	16

2.9	Energy level diagrams for intrinsic and extrinsic semiconductors. The panel on the left side depicts the intrinsic semiconductor, that is, without doping. The figure in the middle shows the n-type semiconductor, which is characterized by having extra electrons close to the conduction band. Finally, the right panel shows the p-type semiconductor, where the holes are the majority carriers. The dashed lines represent the Fermi level, red balls are the electrons, and blue balls are the holes. . . . .	17
2.10	Representation of point defects in a material with two atomic species, where (a) and (b) are vacancies; (c) and (d) are interstitial; (e) is also an interstitial, but it is caused by a foreign atom; (f) and (g) are antisites; (h) is a substitutional defect, where a host atom has been replaced by a foreign atom; (i), (j) and (k) are complex defects composed of different single defects; (l) is the Frenkel pair defect and finally (m) is a Schottky defect. Host atoms are depicted by green and gray balls, while foreign atoms are depicted by red balls. . . . .	20
2.11	c-BN crystal structure, where the (a) primitive cell is a triclinic cell with 2 atoms and (b) conventional cell is a FCC cell with 8 atoms. The figures were designed with VESTA [36]. . . . .	24
2.12	Distribution of high symmetry points in the 1BZ. . . . .	25
2.13	High symmetry points and their respective coordinates. . . . .	25
2.14	Promising defects for quantum technologies in c-BN: (a) $N_B$ , (b) $V_B - V_N$ , (c) $V_B - C_B$ and (d) $V_B - Si_B$ . Here, the green balls are boron and the gray balls are nitrogen. The figures were designed with VESTA [36]. . . . .	26
4.1	Formation energy diagram, where the slopes are determined by $q$ and the intersections are known as transition levels $\varepsilon(q_1, q_2)$ . . . . .	43
4.2	Representation of a CC diagram for the ground and excited states of the defect. . . . .	44
4.3	Workflow for obtaining potential point defects in c-BN. . . . .	48
5.1	(a) Energy cutoff and (b) $k$ -density convergence for primitive cell using three configurations: pristine, increased-volume and decreased-volume cells. Relative energies are the difference of the total energies between the modified cells and pristine cell. . . . .	50
5.2	(a) Energy cutoff and (b) $k$ -density convergence for rhombohedral $\alpha$ -boron using three configurations: pristine, increased-volume and decreased-volume cells. Relative energies are the difference of the total energies between the modified cells and pristine cell. . . . .	51
5.3	(a) Energy cutoff and (b) $k$ -density convergence for nitrogen gas in a cell with a lattice constant $a = 10 \text{ \AA}$ , using three configurations: pristine, increased-volume and decreased-volume cells. Relative energies are the difference of the total energies between the modified cells and pristine cell. . . . .	53

5.4	Convergence test for supercell size. The number of atoms in the supercell is analyzed with respect to the formation energy. . . . .	55
6.1	Band structure diagram computed for bulk diamond using the PBE (red) and HSE06 (blue) functionals. Both methods reveal an indirect band gap in diamond. However, the PBE method yields a band gap of 4.157 eV, while HSE06 calculations yield a band gap value of 5.369 eV when the fraction of exact Hartree-Fock exchange is set to 0.25. Here, HSE06 functional reports a much better agreement with the experimental value of 5.470 eV at 295 K [56]. . . . .	57
6.2	Formation energy diagram for NV center in diamond. Calculations were performed using PBE and HSE06 methods. The band gap obtained with PBE method is 4.157 eV, while with HSE06 method is 5.369 eV. The solid line represents the HSE06 method, while the dashed line corresponds to the PBE method. The curve computed using the PBE method is centered into the plot for illustrative purposes. . . . .	59
6.3	Kohn-Sham level diagrams of the (a) $\text{NV}^0$ and (b) $\text{NV}^{-1}$ defects in diamond calculated using the HSE06 functional. The occupied levels are depicted with a blue ball and either an upward or downward arrow, while the unoccupied levels are depicted by red solid lines. The green dashed curved arrow represents the promotion of an electron from an occupied level to an unoccupied level. . . . .	61
6.4	IPR for the $\text{NV}^{-1}$ defect in diamond calculated using the HSE06 method for (a) the spin up channel and (b) the spin down channel. The occupied electronic states are represented by blue balls, while the unoccupied states are represented by red balls. The energy range goes from 0 to $E_g = 5.369$ eV. . . . .	62
6.5	Band structure diagram computed for bulk c-BN using the PBE (red) and HSE06 (blue) functionals. Both methods reveal an indirect gap in c-BN. However, the PBE method yields a band gap of 4.450 eV, while HSE06 method yields a band gap value of 5.814 eV when the fraction of exact Hartree-Fock exchange is set to 0.25. . . . .	66
6.6	Total DOS computed for bulk c-BN using the PBE (red) and HSE06 (blue) methods. . . . .	67
6.7	(a) Band gap and (b) Lattice constant versus the fraction of the exact Hartree-Fock exchange ( $\alpha$ ) for c-BN. . . . .	68
6.8	Formation energy diagram for point defects in c-BN under B-rich conditions. Calculations were performed using the PBE and HSE06 methods. The band gap obtained with the PBE method is 4.45 eV, while with the HSE06 method it is 5.814 eV. The solid lines represent the HSE06 method, while the dashed lines correspond to the PBE method. The curve computed using the PBE method is centered into the plot for illustrative purposes. . . . .	72

6.9	Formation energy diagrams for point defects in c-BN under N-rich conditions. Calculations were performed using the PBE and HSE06 methods. The band gap obtained with PBE method is 4.45 eV, while with HSE06 method is 5.814 eV. The solid line represents the HSE06 method, while the dashed line corresponds to the PBE method. . . . .	73
6.10	(a) Kohn-Sham level diagram and (b) IPR for the $V_B^{-1}$ defect in c-BN computed using the HSE06 method. The occupied levels are depicted by blue balls and either an upward or downward arrow for spin up or down, respectively, while the unoccupied levels are depicted by red balls and solid lines. The green dashed curved arrow represents the promotion of an electron from an occupied level to an unoccupied level. . . . .	76
6.11	Kohn-Sham level diagrams of the (a) $N_B^{+1}$ and (b) $(V_B - V_N)^0$ defects in c-BN computed using the HSE06 method. The occupied levels are depicted by blue balls and either an upward or downward arrow, while the unoccupied levels are depicted by red balls and solid lines. The green dashed curved arrow represents the promotion of an electron from an occupied level to an unoccupied level. . . . .	77
6.12	IPR for the (a) $N_B^{+1}$ defect in the spin up channel and (b) $(V_B - V_N)^0$ defect in the spin down channel computed using the HSE06 method. The occupied and unoccupied electronic states are represented by blue and red balls, respectively. The energy range goes from 0 to $E_g = 5.814$ eV. . . . .	78
6.13	Kohn-Sham level diagrams of the (a) $(V_B - C_B)^0$ and (b) $(V_B - Si_B)^0$ defects in c-BN using the HSE06 method. The occupied levels are depicted by blue balls and either an upward or downward arrow, while the unoccupied levels are depicted by red balls and solid lines. The green dashed curved arrow represents the promotion of an electron from an occupied level to an unoccupied level. . . . .	79
6.14	IPR for the (a) $(V_B - C_B)^0$ defect and (b) $(V_B - Si_B)^0$ defect, both in the spin down channel computed using the HSE06 method. The occupied electronic states are represented by blue balls, while the unoccupied states are represented by red balls. The energy range goes from 0 to $E_g = 5.814$ eV. . . . .	80
6.15	Convergence tests of the coherence curve with respect to the (a) approximation order (order), where CCE1, CCE2, CCE3 and CCE4 are included; (b) bath cutoff radius ( $r_{\text{bath}}$ ), the sizes are analyzed in a range from 10 to 70 Å; and (c) connectivity distance ( $r_{\text{dipole}}$ ), which is analyzed in a range from 2 to 10 Å. (d) Represents the decay of coherence for the central spin in the $NV^{-1}$ defect in diamond at a magnetic field of 5000 G (5 T). . . . .	85
6.16	Analysis of the coherence function as magnetic field is varied: (a) $B = 15$ G, and (b) $B = 3000$ G. Both plots are generated using the CCE1 and CCE2 approximations. . . . .	86

B.1	Local DOS for (a) Boron and (b) Nitrogen in c-BN using the PBE method. . . . .	98
B.2	Local DOS for (a) Boron and (b) Nitrogen in c-BN using the HSE06 method. . . . .	98
C.1	Band structure for various $\alpha$ in c-BN, where (a) $\alpha = 0.1$ , (b) $\alpha = 0.25$ , (c) $\alpha = 0.33$ , (d) $\alpha = 0.5$ , (e) $\alpha = 0.7$ and (f) $\alpha = 1.0$ . . . . .	100
D.1	IPR for the $NV^0$ defect in diamond using the HSE06 method: (a) Spin up channel and (b) Spin down channel. The occupied electronic states are represent by blue balls, while the unoccupied states are represent by red balls. The energy range goes from 0 to $E_g = 5.369$ eV. . . . .	102

# List of Tables

2.1	Classification of Bravais lattices in 3D. . . . .	5
2.2	A database of candidate defects gathered from the available literature. . . . .	25
3.1	Assumptions to prove <b>HK Theorem I</b> by contradiction. . . . .	31
5.1	Detailed information on the total energies and relative energies for each energy cutoff. An energy cutoff of 500 eV was chosen for c-BN under a convergence criterion of 1 meV (gray shaded area). A complete version of the table can be found in <b>Table A.1</b> . . . . .	50
5.2	Detailed information on the $\mathbf{k}$ -density convergence for c-BN. A $\mathbf{k}$ -density of 4 was chosen under a convergence criterion of 1 meV (gray shaded area). A complete version of the table can be found in <b>Table A.2</b> . . . . .	51
5.3	Detailed information on the energy cutoff convergence for rhombohedral $\alpha$ -boron. An energy cutoff of 450 eV was chosen under a convergence criterion of 1 meV (gray shaded area). A complete version of the table can be found in <b>Table A.4</b> . . . . .	52
5.4	Detailed information on the $\mathbf{k}$ -density convergence for rhombohedral $\alpha$ -boron. A $\mathbf{k}$ -density of 4 was chosen under a convergence criterion of 1 meV (gray shaded area). A complete version of the table can be found in <b>Table A.3</b> . . . . .	52
5.5	Detailed information on the energy cutoff convergence for nitrogen gas. An energy cutoff of 500 eV was chosen under a convergence criterion of 1 meV (gray shaded area). A complete version of the table can be found in <b>Table A.5</b> . . . . .	53
5.6	Detailed information on the $\mathbf{k}$ -density convergence for nitrogen gas. The data confirm that the $\Gamma$ point is sufficient (gray shaded area). An extended version of the table can be found in <b>Table A.6</b> . .	54
5.7	Convergence test of supercell size for c-BN. Supercells were generated by replicating the conventional cell in a range from $2 \times 2 \times 2$ to $6 \times 6 \times 6$ . . . . .	54
6.1	Report of lattice constant and band gap obtained from DFT calculations using the PBE and HSE06 functionals for diamond. Both experimental values are reported at room temperature, while simulations are at 0 K. . . . .	57

6.2	Details of the thermodynamic transition levels with respect to the Fermi level and the defect formation energy for NV center in diamond using both PBE and HSE06 methods. . . . .	59
6.3	Values for the terms of Eqs. 4.26 and 4.29 which enable plotting of the formation energy diagram for the NV center in diamond using the HSE06 method. Here, $E_{perf} = -2276.808$ eV and $E_{VBM} = 9.329$ eV. . . . .	60
6.4	Energies for each Kohn-Sham level within the band gap for the $NV^{-1}$ defect in diamond calculated using HSE06 method. The table includes information for both spin channels and their respective band indexes. An asterisk indicates whether the level is occupied. . . . .	61
6.5	The ZPL values calculated using PBE and HSE06 methods for $NV^0$ and $NV^{-1}$ defects are compared with experimental data [59]. . . . .	64
6.6	Report of lattice constant and band gap obtained from DFT calculations using the PBE and HSE06 functionals for c-BN. The experimental lattice constant is reported at room temperature, while simulations are at 0 K. No experimental data on the electronic band gap has been found. . . . .	65
6.7	Results for the lattice constant and band gap in c-BN, when the fraction of the exact Hartree-Fock exchange ( $\alpha$ ) is varied from 0 to 1. The screening parameter was kept at its default value of $\omega = 0.2$ . The default parameter of HSE06 was used (gray shaded area). A complete version of the table can be found in Table C.1. . . . .	67
6.8	Report of lattice constant and band gap obtained using PBE and HSE06 methods for pure boron in its $\alpha$ -rhombohedral phase. The bond angles found are the same using both methods, $\alpha = 58.03^\circ$ . . . . .	69
6.9	Elemental chemical potentials for boron and nitrogen using the PBE and HSE06 methods. Details of the enthalpy of formation are also added. The PBE method yields $\mu_{cBN} = -17.451$ eV, while the HSE06 method yields $\mu_{cBN} = -20.365$ eV. . . . .	69
6.10	The chemical potential limits ( $\mu_{\{B,N\}}$ ) and chemical potential limits with respect to the elemental chemical potentials ( $\mu_{\{B,N\}}^*$ ) under B-rich and N-rich conditions using the PBE and HSE06 methods. . . . .	70
6.11	Details of the thermodynamic transition levels with respect to the Fermi level ( $E_F$ ) and Formation energy for native and complex defects in c-BN under B-rich and N-rich conditions ( $E_{form}[\{B, N\}-rich]$ ). Both PBE and HSE06 methods are included. . . . .	74
6.12	Energies for each level within the band gap for the native defects using HSE06 method. The table only includes information for the most promising channels, along with their band indices. An asterisk indicate the level is occupied. . . . .	80
6.13	Energies for each level within the band gap for the complex defects using HSE06 method. The table only includes information for the most promising channels, along with their band indices. An asterisk indicate the level is occupied. . . . .	81

6.14	The ZPL values calculated using PBE and HSE06 methods for point defects defects in c-BN. . . . .	83
A.1	Detailed information on the total energies and relative energies for each energy cutoff. An energy cutoff of 500 eV was chosen for c-BN under a convergence criterion of 1 meV (gray shaded area). . . . .	93
A.2	Detailed information on $\mathbf{k}$ -density convergence for c-BN. A $\mathbf{k}$ -density of 4 was chosen under a convergence criterion of 1 meV (gray shaded area). . . . .	94
A.3	Detailed information on the $\mathbf{k}$ -density convergence for rhombohedral $\alpha$ -boron. A $\mathbf{k}$ -density of 4 was chosen under a convergence criterion of 1 meV (gray shaded area). . . . .	94
A.4	Detailed information on the energy cutoff convergence for rhombohedral $\alpha$ -boron. An energy cutoff of 450 eV was chosen under a convergence criterion of 1 meV (gray shaded area). . . . .	95
A.5	Detailed information on the energy cutoff convergence for nitrogen gas. An energy cutoff of 500 eV was chosen under a convergence criterion of 1 meV (gray shaded area). . . . .	96
A.6	Detailed information on the $\mathbf{k}$ -density convergence for nitrogen gas. The data confirm that the $\Gamma$ point is sufficient (gray shaded area). . . . .	97
C.1	Results for the lattice constant and band gap in c-BN, when the fraction of the exact Hartree-Fock exchange ( $\alpha$ ) is varied from 0 to 1. The screening parameter was kept at its default value of $\omega = 0.2$ . The default parameter of HSE06 was used (gray shaded area). Band structure diagrams can be found in Fig. C.1. . . . .	99
D.1	Values for the terms of the Eqs. 4.26 and 4.29, which allow plotting the formation energy diagram for the NV center in diamond using PBE method. Here, $E_{perf} = -1961.920$ eV and $E_{VBM} = 9.646$ eV. . . . .	101
D.2	Energies for each level within the band gap for the $NV^0$ defect using HSE06 method. The table includes information for both channels and their band indexes. An asterisk indicate the level is occupied. . . . .	102
E.1	Values for the terms of the Eqs. 4.26 and 4.29, which allow plotting the formation energy diagram for native defects. Here, $E_{perf} = -1884.741$ eV and $E_{VBM} = 7.295$ eV using PBE method. . . . .	103
E.2	Values for the terms of the Eqs. 4.26 and 4.29, which allow plotting the formation energy diagram for complex defects. Here, $E_{perf} = -1884.741$ eV and $E_{VBM} = 7.295$ eV using PBE method. . . . .	104
E.3	Values for the terms of the Eqs. 4.26 and 4.29, which allow plotting the formation energy diagram for native defects. Here, $E_{perf} = -2199.238$ eV and $E_{VBM} = 6.706$ eV using HSE06 method. . . . .	105

- E.4 Values for the terms of the Eqs. 4.26 and 4.29, which allow plotting the formation energy diagram for complex defects. Here,  $E_{perf} = -2199.238$  eV and  $E_{VBM} = 6.706$  eV using HSE06 method. . . . . 106